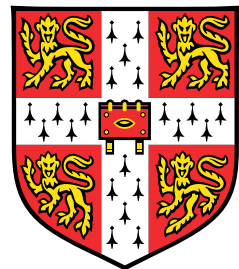


Writing your PhD thesis in **LATEX2e**

Using the CUED template



Krishna Kumar

Department of Engineering
University of Cambridge

This dissertation is submitted for the degree of
Doctor of Philosophy

King's College

February 2017

I would like to dedicate this thesis to my loving parents ...

Declaration

I hereby declare that except where specific reference is made to the work of others, the contents of this dissertation are original and have not been submitted in whole or in part for consideration for any other degree or qualification in this, or any other university. This dissertation is my own work and contains nothing which is the outcome of work done in collaboration with others, except as specified in the text and Acknowledgements. This dissertation contains fewer than 65,000 words including appendices, bibliography, footnotes, tables and equations and has fewer than 150 figures.

Krishna Kumar
February 2017

Acknowledgements

And I would like to acknowledge ...

Abstract

This is where you write your abstract ...

Table of contents

List of figures	9
List of tables	14
Nomenclature	15
1 Introduction	16
1.1 XXXXX	16
1.2 XXXXXX	16
2 Theory	17
2.1 Theory of neutrino physics	17
2.2 Nucleon decay in Grand Unifying Theories	17
2.3 Existing and future experiments	17
2.4 How Liquid Argone Time Projection Chambers work	17
3 The Deep Underground Neutrino Experiment	18
3.1 DUNE location and beam line	18
3.2 The DUNE detectors and schedule	18
3.3 Physics opportunities of DUNE	18
3.3.1 Neutrino physics	18
3.3.2 Nucleon decay and supernovae neutrinos	18
3.3.3 Background to nucleon decay	19
3.4 Path to building DUNE - The 35 ton prototype	19
3.5 The DUNE software	19
4 The 35 ton camera system	28
4.1 The need for cameras in a Liquid Argon Time Projection Chamber	28
4.2 Design of the camera system	28

Table of contents	7
4.3 Tabletop tests	28
4.4 Safety reviews and installation	28
4.5 Performance in the 35 ton	28
5 Simulations of the 35 ton prototype	29
5.1 Determination of interaction times	29
5.2 Calibrating calorimetric constants	33
5.3 Discerning reconstruction efficiencies	34
5.4 Performing particle identification	42
6 The 35 ton data sample	55
6.1 Organisation of the data structure	55
6.2 Reformatting the data to the offline structure	59
6.3 Observations on data quality and noise mitigation	60
6.4 Performance of reconstruction algorithms	65
6.5 Measuring interaction times using electron diffusion	73
6.5.1 Determining interaction times in 35 ton data	75
6.5.2 Determining interaction times in a low-noise detector using Monte Carlo, and differences with data	84
6.5.3 Discerning the impact of changing detector properties using Monte Carlo samples	91
6.5.4 The limitations of and future improvements to the method of interaction time determination using diffusion	95
7 Simulations of the DUNE Far Detector	102
7.1 Simulations of the LBNE surface detector	102
7.2 The use of MUSUN in LArSoft	102
7.3 Nucleon decay channels in DUNE	106
7.3.1 Cosmogenic background to the $n \rightarrow K^+ + e^-$ decay channel	107
7.3.2 Signal events in the $n \rightarrow K^+ + e^-$ decay channel	114
7.3.3 Energy constraints on the cosmogenic background to the $n \rightarrow K^+ + e^-$ decay channel	122
7.3.4 Future improvements to nucleon decay studies	128
References	129
Appendix A Supporting figures to Monte Carlo studies concerning determining interaction times using the effects of diffusion	133

Table of contents	8
Appendix B Something else mildly interesting	142

List of figures

3.1	How the interaction of a cosmic muon can mimic a nucleon decay signature	19
3.2	The wrapped wires of the 35 ton	19
3.3	A representation of the counter locations in the 35 ton	20
3.4	The LArSoft co-ordinate system as it is represented in the 35 ton.	22
3.5	Reconstructed hits from simulated energy depositions	23
3.6	Performing disambiguation with different wire pitches.	25
5.1	Matching tracks and flashes in the 35 ton using positions in the yz plane . .	31
5.2	The central x position of a reconstructed track versus the number of detected photoelectrons	31
5.3	The predicted x positions of flashes using the relationship between photo-electron and drift distance	32
5.4	The number of events as a function of the difference between Monte Carlo and photon detector times	33
5.5	The calibration of the calorimetric constants in the 35 ton	35
5.6	The reconstruction efficiencies for simulated events as a function of Monte Carlo truth track length.	37
5.7	The reconstruction efficiencies for simulated events as a function of Monte Carlo truth deposited energy.	38
5.8	The reconstruction efficiencies for simulated events as a function of Monte Carlo truth track angle in θ	38
5.9	The reconstruction efficiencies for simulated events as a function of Monte Carlo truth track angle in ϕ	39
5.10	The reconstruction efficiencies for simulated events as a function of Monte Carlo truth track angle in θ and ϕ	40
5.11	The mean energy loss per unit track length of different particle masses in different materials	43

5.12	Stopping power for different particle masses as a function of residual range in liquid Argon	45
5.13	The distribution of PIDA values, calculated using Monte Carlo truth, for different particle masses	45
5.14	The reconstruction efficiencies for protons in a sample generated using CRY.	46
5.15	The reconstruction efficiencies for single muons and protons in the 35 ton.	49
5.16	The calculated PIDA values for single muons and protons in the 35 ton.	50
5.17	The $\frac{dE}{dx}$ versus residual range plot for single muons and protons in the 35 ton.	51
5.18	The calculated PIDA values for muons and protons in a CRY sample through the 35 ton	54
6.1	The 35 ton data sample	56
6.2	The 35 ton data structure	58
6.3	Dropped TPC data in the 35 ton	61
6.4	Recovering stuck ADC codes in the 35 ton	62
6.5	Removing coherent noise in the 35 ton	62
6.6	Applying Wiener filters to the 35 ton data	63
6.7	The effect of noise removal algorithms in the 35 ton	64
6.8	dQ/dx in the 35 ton as a function of drift time	67
6.9	The numbering scheme for the East - West counters in the 35 ton	68
6.10	The dot product of the track and vector joining the centres of the coincidence counters in the yz plane	69
6.11	The alignment of reconstructed tracks with the vectors joining the centres of the coincidence counters	69
6.12	Reconstruction efficiencies of through going tracks in the 35 ton data	72
6.13	Schematic showing the process of diffusion	74
6.14	A simulated event display showing multiple tracks and flashes in the 35 ton	75
6.15	The effect of adding a noise baseline to a hit	76
6.16	The most probable values of the <i>RMS</i> and <i>RMS/Charge</i> distributions for tracks with a counter difference of 4 in the 35 ton data	77
6.17	The drift distance dependence of diffusion in the 35 ton dataset for coinci- dences with a counter difference of 4	78
6.18	The angular dependence of diffusion in the 35 ton dataset for hits within 10 cm of the APAs	79
6.19	The distribution of normalised hit charge in the 35 ton dataset	80
6.20	The difference between the predicted and reconstructed hit times in the 35 ton dataset	81

6.21	The accuracy of the hit <i>RMS</i> method in the 35 ton dataset	82
6.22	The accuracy of the hit <i>RMS/Charge</i> method in the 35 ton dataset	83
6.23	The most probable values of the <i>RMS</i> and <i>RMS/Charge</i> distributions for tracks with a counter difference of 4 in the 35 ton data and a low noise 35 ton detector	85
6.24	The drift distance dependence of diffusion in the 35 ton dataset and Monte Carlo for coincidences with a counter difference of 4	86
6.25	The angular dependence of diffusion in the 35 ton dataset and Monte Carlo for hits within 10 cm of the APAs	87
6.26	The distribution of normalised hit charge in the 35 ton dataset and a Monte Carlo sample	88
6.27	Comparing the accuracy of the hit <i>RMS</i> method in the 35 ton dataset and a Monte Carlo simulation	89
6.28	Comparing the accuracy of the hit <i>RMS</i> method in the 35 ton dataset and a Monte Carlo simulation	90
6.29	Comparing the accuracy of the hit <i>RMS</i> method, as the electronic noise changes	93
6.30	Comparing the accuracy of the hit <i>RMS</i> method, as the electronic noise level changes	94
6.31	Comparing the accuracy of the hit <i>RMS</i> method, as the electron lifetime changes	96
6.32	Comparing the accuracy of the hit <i>RMS</i> method, as the electron lifetime changes	97
6.33	Comparing the accuracy of the hit <i>RMS</i> method, as the electric field changes	98
6.34	Comparing the accuracy of the hit <i>RMS</i> method, as the electric field changes	99
6.35	Comparing the accuracy of the hit <i>RMS</i> method, as the constant of longitudinal diffusion changes	100
6.36	Comparing the accuracy of the hit <i>RMS</i> method, as the constant of longitudinal diffusion changes	101
7.1	The correlation between the surface profile and distribution of azimuthal angles at the DUNE far detector site	104
7.2	The distributions of some of the important quantities for a sample of 10^6 muons generated by MUSUN in LArSoft	105
7.3	The initial positions of muons generated by MUSUN around a DUNE 10 kt module	106
7.4	A simulated $n \rightarrow K^+ + e^-$ decay which occurred in a gap between TPCs . .	111

7.5	The energy distribution of background events surviving the application of sequential cuts in the $n \rightarrow K^+ + e^-$ channel	112
7.6	The normalised energy distribution of background events surviving the application of sequential cuts in the $n \rightarrow K^+ + e^-$ channel	113
7.7	A simulated $n \rightarrow K^+ + e^-$ decay which occurred near the edge of the detector volume	115
7.8	The energy distribution of signal events surviving the application of sequential cuts in the $n \rightarrow K^+ + e^-$ channel	116
7.9	The normalised energy distribution of signal events surviving the application of sequential cuts in the $n \rightarrow K^+ + e^-$ channel	116
7.10	A simulated $n \rightarrow K^+ + e^-$ decay where the kaon did not deposit any energy in the active volume	117
7.11	The number of events, as a function of the energy deposited within 2 cm, 5 cm, and 10 cm of the detector edges.	119
7.12	The separation of the kaon and the electron produced in the $n \rightarrow K^+ + e^-$ decay channel	120
7.13	The normalised energy distribution of signal events, and cosmic background events, surviving the application of sequential cuts, after the fiducial cut is modified	121
7.14	The energy directly deposited by kaons, as a function of the energy directly deposited by electrons, in the simulated nucleon decay, and cosmic background samples	124
7.15	The energy directly deposited by kaons, plus the energy directly deposited by electrons, as a function of the energy deposited near the kaon and electron vertex, in the simulated nucleon decay, and cosmic background samples . .	125
7.16	The energy directly deposited by kaons, plus the energy deposited by the kaon decay products, as a function of the energy depositions which do not fit any of the other criteria, in the simulated nucleon decay, and cosmic background samples	126
7.17	The energy directly deposited by kaons, plus the energy deposited by the kaon decay products, plus the energy directly deposited by electrons, plus the energy deposited near the kaon and electron vertex, as a function of the energy depositions which do not fit any of the other criteria, in the simulated nucleon decay, and cosmic background samples	127
A.1	The most probable values of the hit <i>RMS</i> and hit <i>RMS/Charge</i> distributions for tracks with a counter difference of 4, as the electronics noise changes . .	134

A.2	The drift distance dependence of diffusion in the 35 ton dataset and Monte Carlo for coincidences with a counter difference of 4, as the electronics noise changes	134
A.3	The angular dependence of diffusion in the 35 ton dataset and Monte Carlo for hits within 10 cm of the APAs, as the electronics noise changes	135
A.4	The normalised hit charge distribution as the electronics noise changes	135
A.5	The most probable values of the hit <i>RMS</i> and hit <i>RMS/Charge</i> distributions for tracks with a counter difference of 4, as the electron lifetime changes	136
A.6	The drift distance dependence of diffusion in the 35 ton dataset and Monte Carlo for coincidences with a counter difference of 4, as the electron lifetime changes	136
A.7	The angular dependence of diffusion in the 35 ton dataset and Monte Carlo for hits within 10 cm of the APAs, as the electron lifetime changes	137
A.8	The normalised hit charge distribution as the electron lifetime changes	137
A.9	The most probable values of the hit <i>RMS</i> and hit <i>RMS/Charge</i> distributions for tracks with a counter difference of 4, as the electric field changes	138
A.10	The drift distance dependence of diffusion in the 35 ton dataset and Monte Carlo for coincidences with a counter difference of 4, as the electric field changes	138
A.11	The angular dependence of diffusion in the 35 ton dataset and Monte Carlo for hits within 10 cm of the APAs, as the electric field changes	139
A.12	The normalised hit charge distribution as the electric field changes	139
A.13	The most probable values of the hit <i>RMS</i> and hit <i>RMS/Charge</i> distributions for tracks with a counter difference of 4, as the constant of longitudinal diffusion changes	140
A.14	The drift distance dependence of diffusion in the 35 ton dataset and Monte Carlo for coincidences with a counter difference of 4, as the constant of longitudinal diffusion changes	140
A.15	The angular dependence of diffusion in the 35 ton dataset and Monte Carlo for hits within 10 cm of the APAs, as the constant of longitudinal changes	141
A.16	The normalised hit charge distribution as the constant of longitudinal diffusion changes	141

List of tables

3.1	Nucleon decay limits in DUNE and Super-Kamiokande	18
5.1	Stopping power parameterisation for various particle types in liquid Argon .	44
5.2	The properties of initial particles simulated in the muon and proton samples. The angles θ_{xz} and θ_{yz} are defined as the angle that a vector makes in the xz and yz planes respectively.	48
5.3	A summary of the PIDA values calculated for the proton sample as sequential cuts are applied	52
5.4	A summary of the PIDA values calculated for the muon sample as sequential cuts are applied	52
5.5	A summary of the PIDA values calculated for the primary particles in the proton sample as sequential cuts are applied	53
6.1	The angles which tracks, with given counter differences have, relative to the APA frames	71
7.1	Muon flux parameters as calculated with MUSIC/MUSUN.	103
7.2	The number of events surviving isolated cuts which could mimic a $n \rightarrow$ $K^+ + e^-$ decay	114

Nomenclature

Roman Symbols

tick Unit of time equal to 500 ns

Acronyms / Abbreviations

CRC Cosmic Ray Counter

FD Far Detector

MIP Minimally Ionising Particle

MPV Most Probable Value

PID Particle IDentification

PoCA Point of Closest Approach

PoCA Point of Closest Approach

ROI Region Of Interest

ADC Analogue to Digital Converter

SiPM Silicon Photo Multiplier

TPC Time Projection Chamber

¹ **Chapter 1**

² **Introduction**

³ **1.1 XXXXX**

⁴ **1.2 XXXXXX**

Chapter 2

Theory

2.1 Theory of neutrino physics

3

2.2 Nucleon decay in Grand Unifying Theories

4

2.3 Existing and future experiments

5

2.4 How Liquid Argone Time Projection Chambers work

6

¹ Chapter 3

² **The Deep Underground Neutrino ³ Experiment**

⁴ **3.1 DUNE location and beam line**

⁵ **3.2 The DUNE detectors and schedule**

⁶ **3.3 Physics opportunities of DUNE**

⁷ **3.3.1 Neutrino physics**

⁸ **3.3.2 Nucleon decay and supernovae neutrinos**

Table 3.1 Nucleon decay limits in DUNE and Super-Kamiokande, in some favoured decay channels.

Total flux ($\text{cm}^{-2} \text{s}^{-1}$)	Mean E_μ (GeV)	Mean slant depth (m w.e)	Mean θ ($^\circ$)
5.66×10^{-9}	283	4532	26

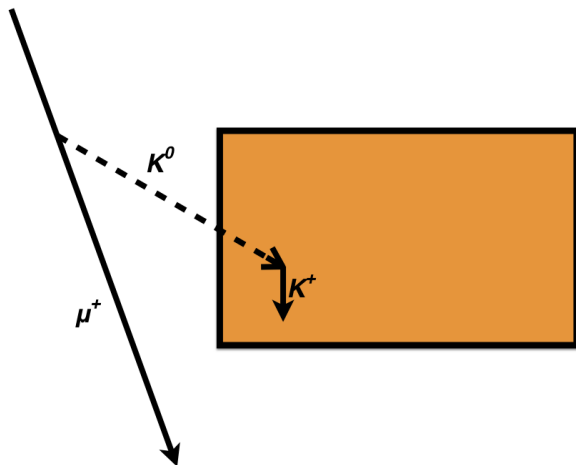


Fig. 3.1 How the interaction of a cosmic muon can mimic a nucleon decay signature, by producing a K_L^0 which interacts far from the detector wall, producing an isolated kaon.

Fig. 3.2 A schematic showing what the wrapped wire planes of the DUNE detector designs looked like in the 35 ton.

3.3.3 Background to nucleon decay

1

3.4 Path to building DUNE - The 35 ton prototype

2

3.5 The DUNE software

3

The software package used by DUNE is called LArSoft [1] [2] which is a simulation, reconstruction and analysis package for Liquid Argon Time Projection Chamber (LArTPC) that is being used by many experiments in the US neutrino program. LArSoft has been developed to be detector agnostic, meaning that much of the code is shared between experiments. To this end it is envisioned that it will be used as a platform for constant development in existing experiments and those still in the planning phases such as DUNE. LArSoft is built around the Fermilab-supported *analysis reconstruction framework (art)*. External packages such as ROOT [3] and GEANT4 [4] are incorporated into LArSoft meaning that the user does not have to coordinate specific versions of the packages as the newest versions are automatically incorporated.

4

5

6

7

8

9

10

11

12

13

14

There are numerous mechanisms by which particles can be generated within the software with external packages. One such package is GENIE [5] which is used to study neutrino interactions and nucleon decays. Another package, Nuance [6], is a neutrino interaction generator

15

16

17

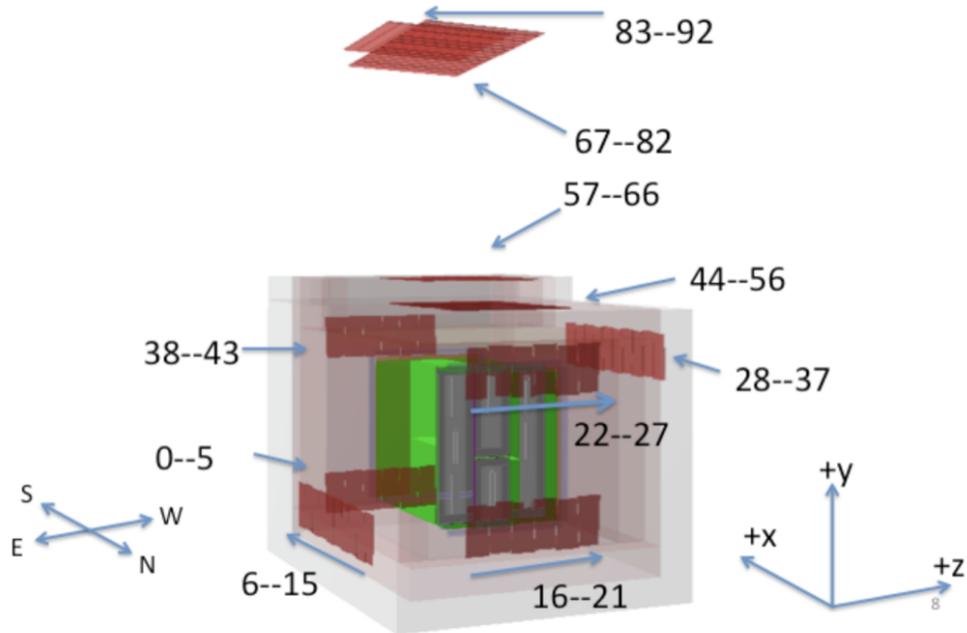


Fig. 3.3 A representation of the counter locations in the 35 ton, with the magnetic and LArSoft co-ordinate systems shown. The other detector components can be seen inside the cryostat, such that the counters on the North wall are behind the short drift volume. The East - West counters are numbered 6-15 and 28-37 respectively. The North Lower - South Upper counters are numbered 16-21 and 38 - 43 respectively. The North Upper - South Lower counters are numbered 22-27 and 0-5 respectively. The telescope triggers are numbered 44-92 and are split into four groups.

¹ specifically for Liquid Argon (LAr). Finally, CRY [7] and CORSIKA!!!^{citepCORSIKA}
² are cosmic ray events generators which are used to simulate the expected event rates for
³ surface detector locations in absence of a neutrino beam. Recently the MUon Simulations
⁴ UNderground (MUSUN) [8] [9] generator which takes the output of MUon SImulation Code
⁵ (MUSIC) [8] [10] [11] has also been incorporated, see Section 7.2 for further details. It is
⁶ also possible to use an inbuilt single particle generation mode which is fully tuneable as
⁷ particle type, momenta, positions and directions can all be varied.

⁸

⁹ The co-ordinates and angles in LArSoft are defined as follows, and schematic representa-
¹⁰ tions of how this appears in the 35 ton are shown in Figure 3.4:

¹¹ • x - The beam direction, with maximal x being where the beam enters the detector.

- In the 35 ton prototype where there is no beam positive x is in the opposite direction to that which electrons drift in the large TPC, where $x = 0$ is the position of the APA frames in the long drift volume. 1
2
3
- In the far detector geometry $x = 0$ is defined as the midpoint between the two rows of CPAs 4
5
- y - The vertical direction, with maximal y being the most highest point. 6
 - In the 35 ton $y = 0$ is halfway between the gap created by the two centre APAs which are mounted one above the other. 7
8
 - In the far detector $y = 0$ is defined as the midpoint between the two vertical layers of TPCs. 9
10
- z - Defined as such to have a right handed co-ordinate system. 11
 - In the 35 ton $z = 0$ is at the edge of the leftmost APA frame when looking down the long drift volume. 12
13
 - In the far detector $z = 0$ is defined at the edge of the leftmost APA frame when looking down the long drift volume. 14
15
- θ - The angle that a vector makes from the x axis in the xy plane. 16
- ϕ - The angle between the z axis and the vector. 17

The simulation of particles is usually split into five separate distinct processes to reflect the different stages in which development often progresses. The advantage of segmenting the computational process in this way is that improvements can easily applied to a file without rerunning the entire chain. This is especially important when large Monte Carlo or data samples are produced for general use within collaborations so that users are able to concentrate on improving a specific part of the computational process. When these all-purpose samples are produced the analysis performed provides users with any Monte Carlo truth information along with the reconstructed quantities for use in analyses performed outside LArSoft. The computational process is often broken down in the following way: 18
19
20
21
22
23
24
25
26

- Particle generator. 27
- Particle transport using GEANT4. 28
- Full detector simulation, including detector responses. 29
- Full event reconstruction. 30

3.5 The DUNE software

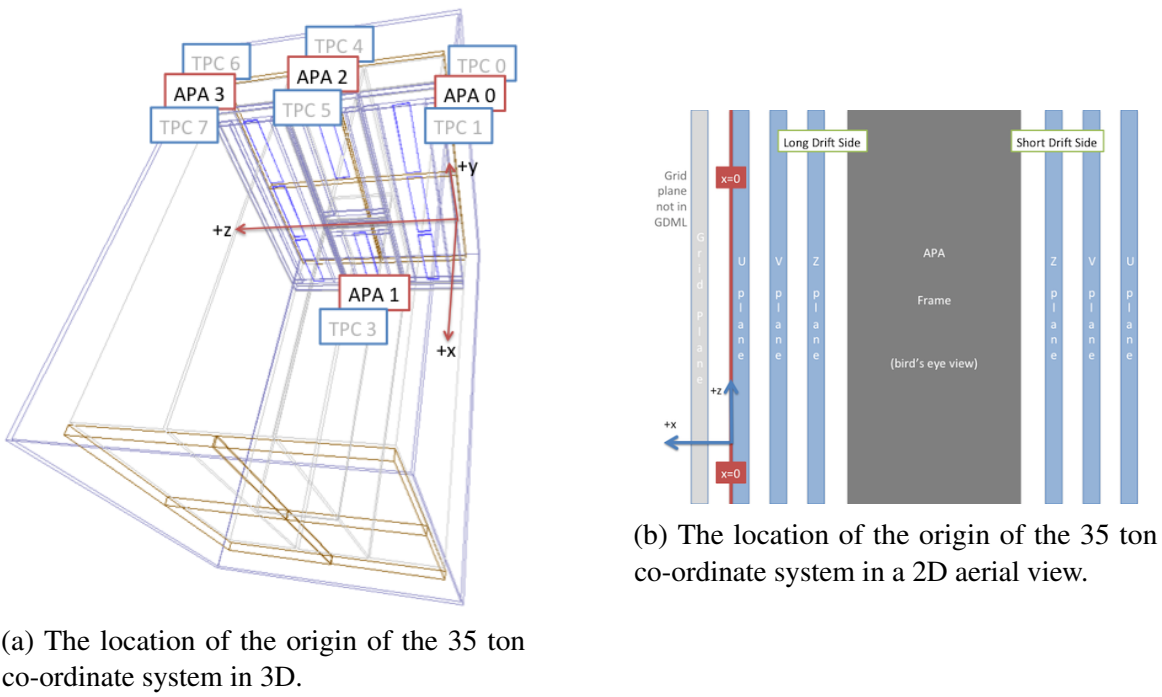


Fig. 3.4 The LArSoft co-ordinate system as it is represented in the 35 ton. Left shows the location of the origin relative to the TPC detector components. The four APAs, and eight TPCs are shown, where the even numbered TPCs are on the short drift side, ~ 20 cm drift, and the odd numbered TPCs are on the long drift side, ~ 250 cm drift. The CPAs are also shown as the objects with a brown outline. Right shows the location of the origin with respect to the APAs. The wire planes are shown, the U and V planes are induction wires, whilst the Z planes are collection wires.

¹ • Analysis.

² Later significant focus will be given to the reconstruction of TPC data, and so it is
³ necessary to briefly illustrate the mechanisms by which TPC data is reconstructed in LArSoft.
⁴ Much of the information presented below is summarised in [12] [2]. After the full detector
⁵ simulation or data taking, detector effects such as the electronics response function and a
⁶ pedestal offset have to removed. Once these effects are removed the signal is estimated using
⁷ the optimal value of *signal/noise* which would produce the measured signal. This process,
⁸ called deconvolution, does not conserve pulse height and is not guaranteed to preserve the
⁹ normalisation. The deconvoluted signals are all unipolar distributions which means that
¹⁰ Gaussian distributions can then be fitted to them when trying to reconstruct hits. This is
¹¹ shown in Figure 3.5, and explained further below.

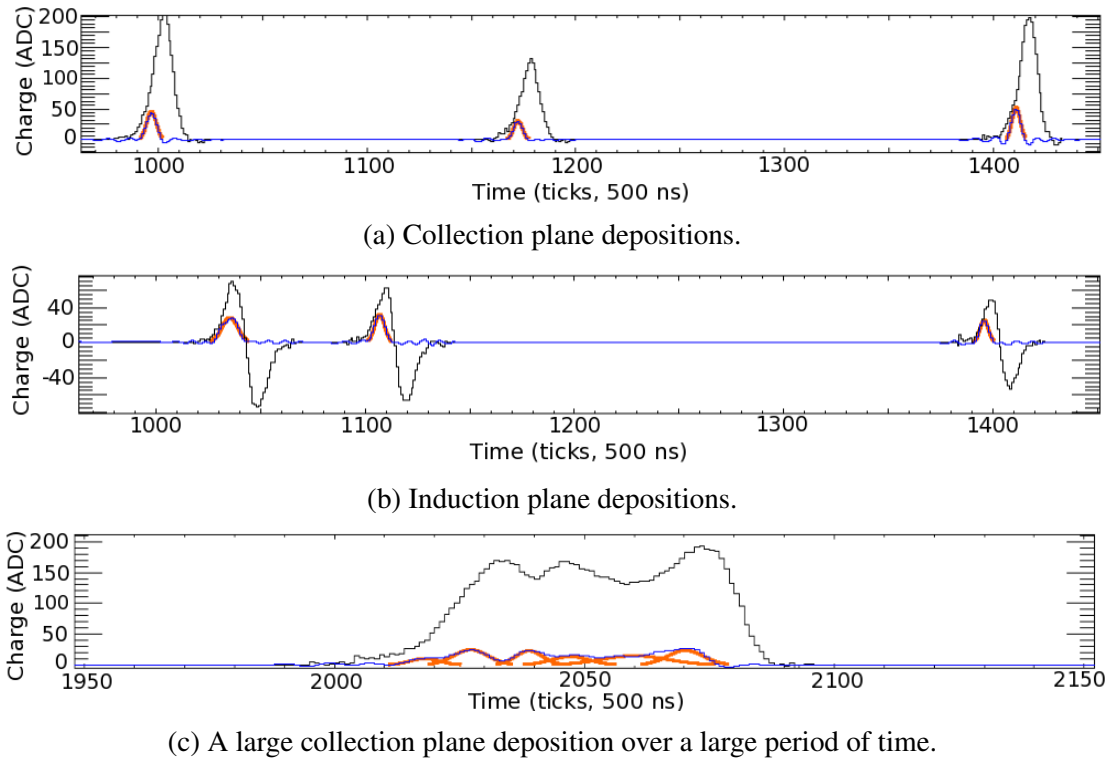


Fig. 3.5 The raw and deconvoluted signals with reconstructed hits on single wires for simulated energy depositions. The depositions, from particles generated by CRY, are not from a single event and have been selected for demonstration purposes only. The plots are shown with increasing charge (ADC) on the y axis, and increasing time (ticks, 500 ns) on the x axis. The black lines represent the raw signals, the blue lines represent the deconvoluted signals and the orange lines represent the reconstructed hits. Top shows depositions on a collection plane wire, it can be seen that the raw signal is unipolar. Middle shows depositions on an induction plane wire, it can be seen that the raw signal is bi-polar whilst the deconvoluted signal and reconstructed hits are unipolar. Bottom shows a complex deposition on a collection plane wire, where multiple reconstructed hits are required to reproduce the deconvoluted signal.

The deconvoluted signals are reconstructed into hits by identifying regions that are above a threshold value and then attempting to replicate the signal in these regions by introducing Gaussian distributions. For isolated hits this is typically achieved using only one Gaussian distribution, however for large energy depositions over a large period time where many particles are involved, multiple Gaussian distributions are often required. Large energy depositions are also possible when the direction of the particle aligns with a wire, this means that all of the deposited energy is collected on this single wire. Examples of reconstructed hits are shown in Figure 3.5. These figures are taken from separate CRY simulated events, and so do not correspond to a continuous simulated event. They have been selected only as

1
2
3
4
5
6
7
8
9

3.5 The DUNE software

24

¹ a demonstration of the process of hit reconstruction. Figures 3.5a and 3.5b show multiple
² time-separated energy depositions on a collection and induction wire respectively. A more
³ complex energy deposition on a collection plane wire is shown in Figure 3.5c where energy
⁴ depositions from many particles at similar times have created a complicated energy deposi-
⁵ tion that requires many reconstructed hits to explain.

⁶

⁷ As noted in Section 3.2 and Section 3.4 the DUNE FD and the 35 ton both have wrapped
⁸ wires on the induction planes. A result of this is that the location of the reconstructed hit on an
⁹ induction wire is ambiguous as a single wire has many wire segments, as shown in Figure 3.2.
¹⁰ An important feature of this ambiguity is that the TPC in which the hit occurred cannot be
¹¹ identified unless it is combined with another hit. These ambiguities do not extend to the
¹² collection plane wires as they are not wrapped and so consist of only a single wire segment
¹³ in a single TPC. Hits are combined across the three planes by identifying wire segments on
¹⁴ each plane which intersect and have hits at common times. In the traditional reconstruction
¹⁵ process only hits that make these so-called ‘triple points’ are considered disambiguated, with
¹⁶ other hits being identified as noise hits causing them to be discarded.

¹⁷

¹⁸ The inclination of the wire planes has to be carefully chosen so as to minimise both
¹⁹ the number of wires required and the number of times that wire triplets intersect. This is
²⁰ shown in Figure 3.6, where the wire inclinations used in the 35 ton detector, are compared
²¹ to those in the DUNE FD reference design. The inclination of wires in the 35 ton was 45°
²² $\pm 0.7^\circ$ meaning that many wire triplets cross twice and some wire pairs cross three times.
²³ When wire triplets cross multiple times the triplet which has the smallest distance between
²⁴ the common intersection point and the two, two-wire intersection points, is chosen as the
²⁵ best intersection candidate. This is shown as the ‘Good intersection’ on the right panel in
²⁶ Figure 3.6. The different wire pitches are necessary so that one of the triple points can
²⁷ be evaluated to be a better candidate, as with a wire pitch of 45° it can be impossible to
²⁸ distinguish between different triple points. The inclination of wires in the FD was chosen
²⁹ to be 36° to remove the possibility of multiple intersection points, as given the geometry of
³⁰ the APAs multiple intersection points are impossible and so disambiguation is much simpler.
³¹ The lower inclination results in more induction wires being required though, making it more
³² expensive to instrument the detector. It is also important that all wires on a given APA are
³³ either read at the top or base of the APA, depending on whether the APA is at either the top
³⁴ or the base of the detector respectively. This is because there must be minimal space between
³⁵ TPCs in the DUNE FD to reduce the internal dead space, and so TPCs cannot be read out
³⁶ along the sides as this would require a non-negligible amount of space to accommodate the

3.5 The DUNE software

cabling.

1

2

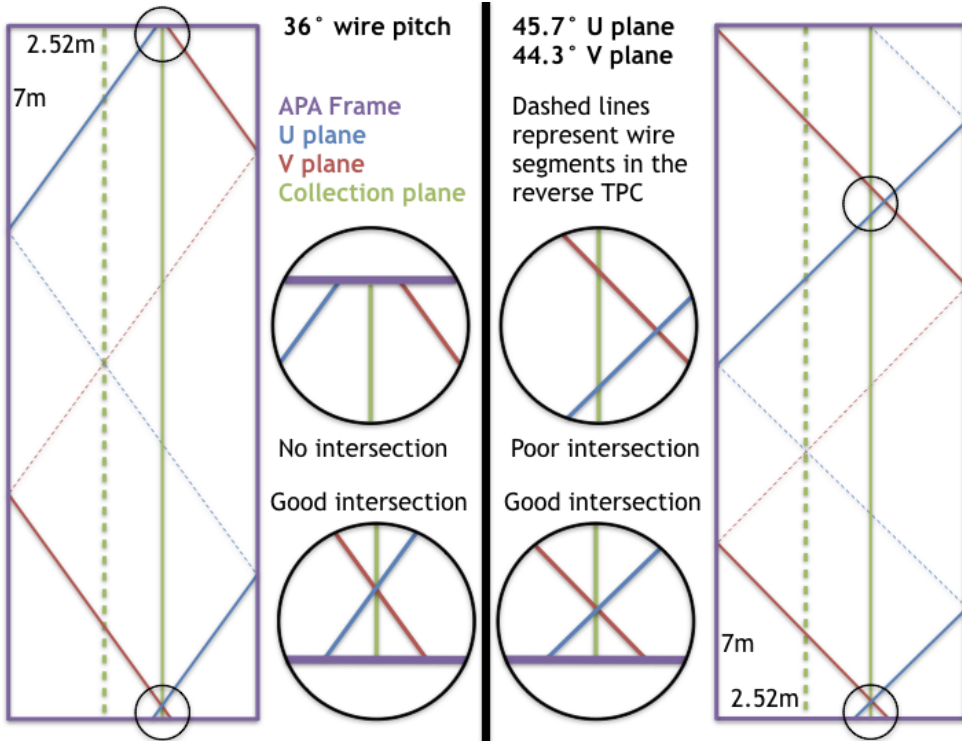


Fig. 3.6 The effect that different wire pitches have on the ability to perform disambiguation in APAs with the far detector geometry. The left panel shows a wire pitch of 36° , which is the reference design for the far detector, whilst the right panel shows wire pitches of $45^\circ \pm 0.7^\circ$, as was used in the 35 ton. The left panel shows that only one 'triple point' can be made with the three wires shown, and so disambiguation is relatively trivial. The right panel shows that two 'triple points' can be made with the three wires shown, the 'triple point' where the three wires have a common intersection point is labelled as a 'good intersection' and it is this intersection point which would be chosen for the disambiguated hit.

Once the hits have been disambiguated they are combined to make clusters in each of the three planes, before the clusters are merged to make reconstructed tracks or showers. The clustering process is usually performed in wire-tick space on each plane separately, where all the hits from a single track or shower should make a single cluster on each plane. It is possible to seed the start of clusters by using imaging techniques such as a Harris transform [13], or to identify straight lines by using Hough transforms [14]. As hits from a physical entity are unlikely to remain on a single channel or all come at identical times, clusters are often spread out over many channels for a range of times especially when performing clustering for showers.

3

4

5

6

7

8

9

10

11

12

Once clusters have been identified in each plane they can then be merged into 3-dimensional tracks and showers. The two most common tracking algorithms are PM-Track [15] and Pandora [16], and the most common showering algorithm is EMShower [17]. Once 3D objects have been reconstructed, the calorimetric quantities need to be determined, this is often done separately for each plane. Two models exist for calculating $\frac{dE}{dx}$ in LArSoft, Birks model [18] and a modified Box model [19] which uses a correction to the Box model [20] at low values of $\frac{dE}{dx}$. Normally the modified Box model is used as it holds for both large and small ionisation's, whereas Birks model experiences difficulties at large ionisation's and the traditional Box model struggles at low $\frac{dE}{dx}$. Both models incorporated in LArSoft, calculate the $\frac{dE}{dx}$ of a hit using the deposited charge (dQ) and the track pitch (dx) of the hit as well as the conversion of ADC value to number of electrons ($C_{GeV \rightarrow e^-}$), a correction due to electron lifetime ($C_{lifetime}$), the LAr density (ρ), the electric field (E_{field}) and the tuneable electron recombination factors ($Recomb_X$). The series of equations used in Birks model are shown in Equation 3.1, whilst those used in the modified Box model are shown in Equation 3.2.

16

$$\frac{dE}{dx} = \frac{dQdx}{\alpha - (\beta \times dQdx)} \quad (3.1a)$$

$$dQdx = \frac{dQ \times C_{lifetime}}{dx \times C_{ADC \rightarrow e^-}} \quad (3.1b)$$

$$\alpha = Recomb_A \times C_{GeV \rightarrow e^-} \times 10^{-3} \quad (3.1c)$$

$$\beta = \frac{Recomb_B}{\rho \times E_{field}} \quad (3.1d)$$

$$\frac{dE}{dx} = \frac{e^\alpha - Recomb_A}{\beta} \quad (3.2a)$$

$$\alpha = \frac{10^3 \times \beta}{C_{GeV \rightarrow e^-}} \times \frac{dQ}{dx} \quad (3.2b)$$

$$dQdx = \frac{dQ \times C_{lifetime}}{dx \times C_{ADC \rightarrow e^-}} \quad (3.2c)$$

$$\beta = \frac{Recomb_B}{\rho \times E_{field}} \quad (3.2d)$$

When performing calorimetry it is also important that the interaction time is known so that the x positions of hits can be corrected, as they will be reconstructed assuming an

interaction time of 0 s. This assumption is made because when using beam events the beam trigger is placed at a time of $T = 0$. An unknown interaction time causes the hit and track positions to be calculated incorrectly, and will also skew the calorimetric corrections, as recombination is a drift dependant effect.

1

2

3

4

¹ Chapter 4

² The 35 ton camera system

³ 4.1 The need for cameras in a Liquid Argon Time Project- ⁴ tion Chamber

⁵ 4.2 Design of the camera system

⁶ 4.3 Tabletop tests

⁷ 4.4 Safety reviews and installation

⁸ 4.5 Performance in the 35 ton

Chapter 5

Simulations of the 35 ton prototype

5.1 Determination of interaction times

As outlined at the end of Section 3.5 it is important to know the interaction time of a track when performing calorimetric reconstruction. When performing simulations the simplest interaction time to assign to a reconstructed object is the Monte Carlo truth time of when the particle was created. The generation time can be used, as the time taken to travel the distances considered in simulations, less than 100 ns, is small when compared to the resolution of the detector (500 ns). When matching a reconstructed object with a GEANT4 particle the particle which contributed the most overall deposited charge to the whole track is chosen. This means that the energy deposited for each hit on the track is broken down into how much each particle contributed to the charge of the individual hit, with the energies summed over all hits. The ability to assign the true interaction times to 3D objects is vital when wanting to benchmark how well other algorithms to estimate interaction times perform or to determine the efficiency of the tracking algorithms as described in Section 5.3.

In the 35 ton detector, it was envisioned that there would be at least two ways in which interaction times could be assigned to tracks, one using the external cosmic ray counters and another using reconstructed scintillation light collected by the photon detectors. The cosmic ray counters were used extensively in the 35 ton data, as described in Section 6.4. However, in simulations the scintillation light was used as this would have been more powerful during continuous running. This is because, not all particles would pass through the counters but, one would expect almost all of them to produce reconstructable scintillation light. The flashes of light are reconstructed using a pre-built library which models the expected number of photoelectrons to be measured on each photon detector given the 3D position of the source of the flash. Using the library it is then possible to reconstruct the location of a flash in

5.1 Determination of interaction times

30

1 three dimensions, given the relative amounts of light that each photon detector collects. For
2 example, less scintillation light will be collected for a flash that originated further away from
3 the photon detectors. This library also takes into account the expected quantum efficiencies
4 of each photon detector.

5

6 When trying to produce an association metric a sample of 10,000 isolated positive muons
7 generated with CRY at $T = 0$ was used. Isolated particles were used as then there should
8 only be one long track with which to match one reconstructed flash. The positive muons
9 were generated outside of the detector with a constant y position, above the uppermost
10 scintillation counters, and flat distributions in x and z . When this sample was simulated it
11 was clear that the photon detector reconstruction using the pre-built libraries worked well
12 as the reconstructed flash source normally lay very close to the track which caused it. It
13 was found that a Point of Closest Approach (PoCA) calculation of the reconstructed track to
14 the reconstructed flash centre, gave an effective metric by which the flash and track could
15 be associated. Other metrics such as the distance between the flash and track centres, and
16 the perpendicular distance between the flash centre and the line joining the start and end of
17 track were investigated but found to provide less reliable metrics. The latter of these metrics
18 is less effective because the reconstructed tracks are rarely straight lines, due to particles
19 scattering as they travel through the LAr, and so the perpendicular distance at each hit must
20 be calculated. A comparison of these metrics is shown in Figure 5.1.

21

22 Another metric by which flashes could be assigned to reconstructed tracks is by utilising
23 the relationship between the number of measured photoelectrons in the simulation, and the
24 distance from the APAs at which they were produced. When considering two flashes of
25 scintillation light that are produced at different distances from the APAs, it would be expected
26 that more photoelectrons would be collected when the photons were produced closer to
27 the APAs. This relationship is shown in Figure 5.2 where it can be seen that there is an
28 exponential decay in the number of photoelectrons which are measured with increasing drift
29 distances. Utilising this relationship, means that the distance from the APAs can be predicted
30 from the number of photoelectrons which are measured. This predicted distance from the
31 APA planes can then be compared to the expected x position of a reconstructed track given
32 the difference in flash time and hit times, this is shown in Figure 5.3. The difference in these
33 two quantities can then be used as the second metric as it gives an indication of how well
34 the properties of a flash match the reconstructed x position of the track. If the predicted
35 and reconstructed x positions are identical then the track and flash are well matched, this

5.1 Determination of interaction times

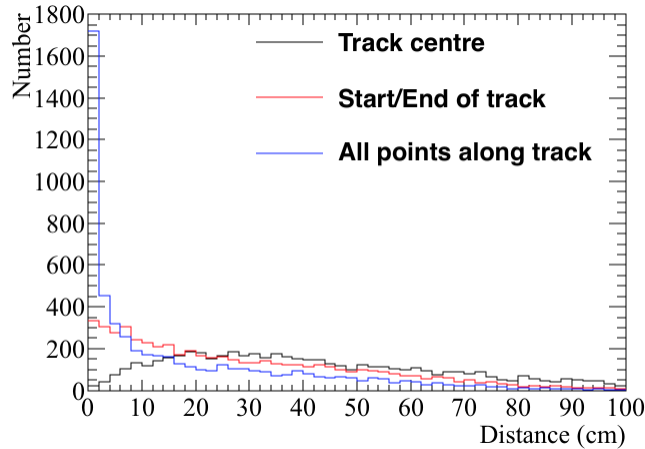


Fig. 5.1 The number of events as a function of the calculated distance between a reconstructed track and a reconstructed flash for various metrics. The distance between track centre and the flash centre is shown in black. The perpendicular distance between the flash centre and the line joining the start and end of the track is shown in red. The point of closest approach between the flash centre and all hits along the track is shown in red.

corresponds to the collection of points around the $y = x$ line in Figure 5.3.

1

2

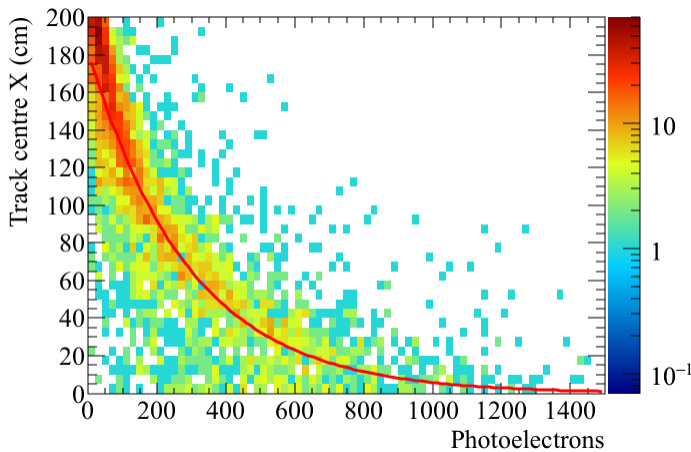


Fig. 5.2 The central x position of a reconstructed track versus the number of detected photoelectrons. The red line corresponds to a parameterisation of the distribution, so that the measured number of photoelectrons can be used to predict the central x position of the track, that the flash should be associated with.

Using these metrics it is possible to attempt to assign reconstructed flashes to reconstructed tracks. Only flashes which are within one drift window of a given track are considered, as flashes outside of this time window cannot have been caused by the reconstructed

3

4

5

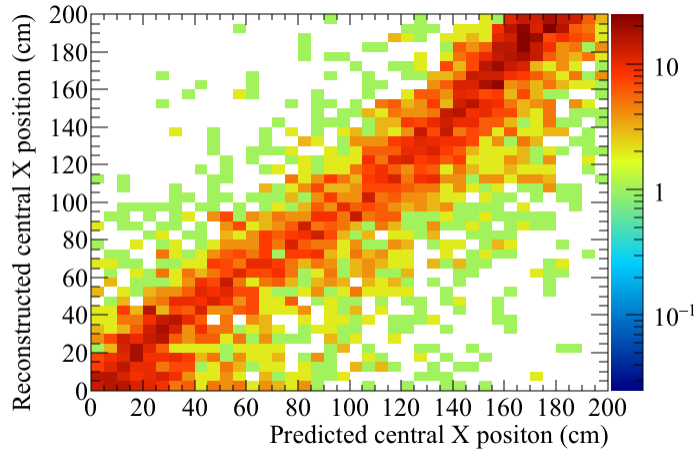


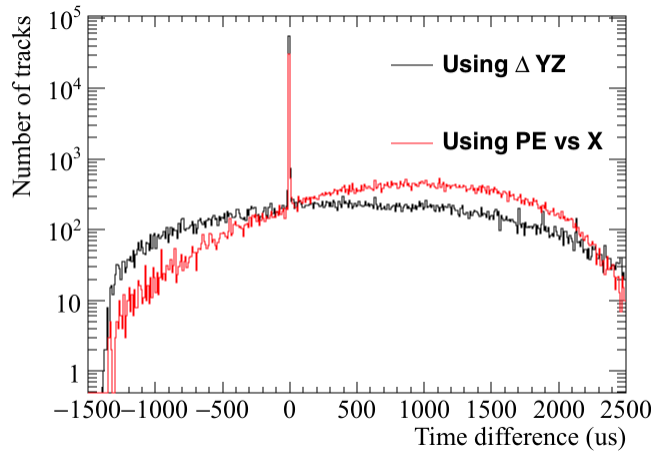
Fig. 5.3 A comparison of the x position predicted using the relationship in Fig 5.2 and the x position predicted by using the difference in flash and hit times.

1 track. Once flashes are assigned to tracks it is possible to determine how well the matching
2 has performed by comparing the Monte Carlo truth interaction time with the photon detector
3 interaction time. When doing this it is more useful to use a CRY sample which spans multiple
4 drift windows, as then incoming particles will create scintillation flashes at random timings
5 as opposed to all at $T = 0$ in the positive muon sample initially considered. The CRY sample
6 over multiple windows contains many particles generated by CRY, and is not limited to only
7 producing positive muons, meaning that it better represents the cosmic flux observed by the
8 35 ton detector. This comparison is shown in Figure 5.4, where there is a clear peak at a time
9 difference of 0 ms in the Monte Carlo truth and photon detector times. When zooming in on
10 this peak it can be seen that there is a systematic offset of $0.6 \mu\text{s}$, this is due to an electronics
11 offset applied in the simulation to the photon detector system.

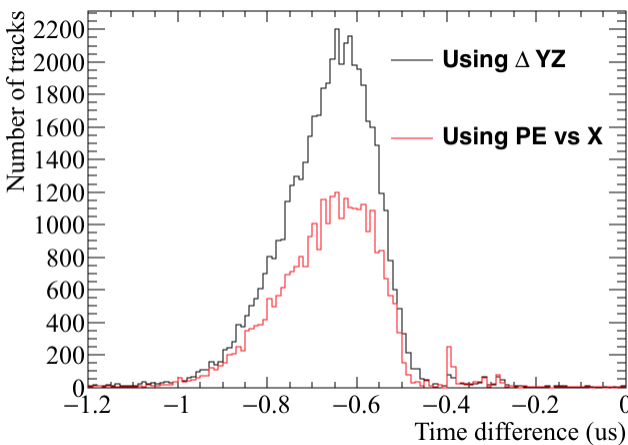
12
13 From Figure 5.4 it can clearly be seen that the metric using the proximity of the flash
14 centre to the track trajectory yields the best matches. This is likely caused by the large spread
15 in the number of photoelectrons collected at fixed drift distances, as shown by Figure 5.2.
16 The two metrics can be combined to give a prediction for the interaction time, though given
17 the increased sensitivity from the proximity metric this should be given greater weighting. In
18 physics data the metric using the number of collected photoelectrons is particularly sensitive
19 to the absolute light level in the detector as a high residual light level would reduce the
20 proportional change in the number of photoelectrons collected for increasing drift distances.
21 This metric also relies a sample of tracks with known x positions upon which it can be
22 calibrated which may be difficult to obtain.

23

5.2 Calibrating calorimetric constants



(a) The difference in interaction times.



(b) Zoomed in at low time differences.

Fig. 5.4 The number of events as a function of the difference between Monte Carlo and photon detector times. The difference in interaction times over a large range of times is shown top. The peak at a time difference of 0 is expanded to show a systematic offset of 0.6 μ s, due to an electronics offset is shown bottom.

5.2 Calibrating calorimetric constants

Having the correct calorimetric responses is vital when trying to calculate $\frac{dE}{dx}$ as the measured change in charge has to be correctly converted to the change in energy. The parameter which has to be tuned in order to ensure that this is done correctly is the number of electrons that each ADC corresponds to. This was presented in Equations 3.1 and 3.2 as $C_{ADC \rightarrow e^-}$. Each plane will have a different response function, and so each plane has to be treated separately. These parameters have to be tuned in such a way as to make a known particle energy deposition have the correct $\frac{dE}{dx}$, the easiest deposition to tune against is the minimally

¹ ionising particle (MIP) peak, which in LAr should have a value of 1.8 MeV cm^{-1} . To do
² this the sample of 10,000 positive muons made to calibrate the photon detector track/flash
³ assignment will be used as many of these particles will be MIPs.

⁴

⁵ To select the MIPs in the sample only tracks caused by through-going muons are used.
⁶ The $\frac{dE}{dx}$ value for all hits in all tracks is then calculated, and the different planes are considered
⁷ separately. A Gaussian distribution is then fitted around the peaks for each of the planes to
⁸ discern the most probable value (MPV) of $\frac{dE}{dx}$ for that plane. If the MPVs are not equal to
⁹ 1.8 MeV cm^{-1} then the ADC to electron parameters are scaled by the factor between the
¹⁰ measured MPV and the MIP peak. As the relationship between $\frac{dE}{dx}$ and $C_{ADC \rightarrow e^-}$ is not linear
¹¹ an element of trial and error is required until the correct MPVs are measured. An example of
¹² the calibration being applied is shown in Figure 5.5. Calibration of the response functions is
¹³ required whenever the electronics gains or signal shaping functions are changed.

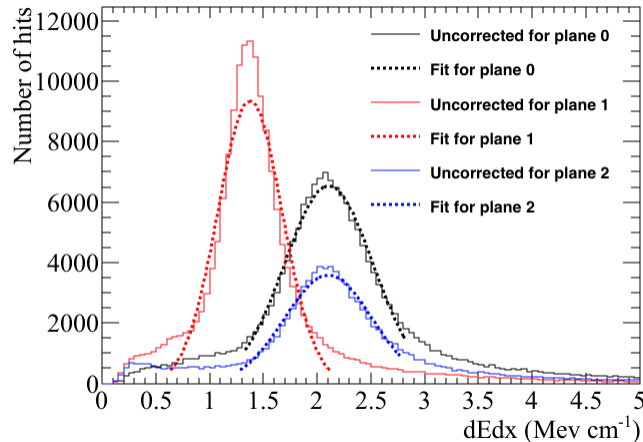
¹⁴ 5.3 Discerning reconstruction efficiencies

¹⁵ Knowledge of the strengths and weaknesses of different tracking algorithms is vital when
¹⁶ using them for physics analyses. To this end it is useful to develop a metric by which they
¹⁷ can be compared. In order to do this a series of conditions have to be applied to the recon-
¹⁸ structed tracks from a large set of simulated particles which are reconstructed using different
¹⁹ tracking algorithms. It is interesting to observe what the effect of event complexity has on the
²⁰ reconstruction algorithms and so efficiencies will be calculated for both of the CRY samples
²¹ used in Section 5.1. The sample referred to as the positive muon sample contains single
²² positive muons generated at $T = 0$, with a constant y position above the scintillation panels,
²³ and flat distributions in x and z . The sample referred to as the CRY sample, contains multiple
²⁴ particles of multiple particle types, generated at times spanning multiple drift windows, and
²⁵ at an altitude above sea level of 0 m.

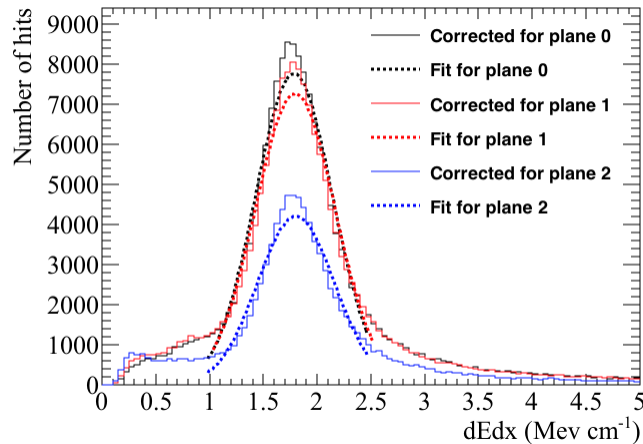
²⁶

²⁷ The criteria upon which to determine whether a particle is well reconstructed has to be
²⁸ carefully chosen as every definition will have limitations. For example, consider a particle
²⁹ that travels 100 cm in the active volume of the detector but is reconstructed as 2 separate
³⁰ tracks (tracks 1 and 2), with lengths 77 cm and 23 cm respectively. Firstly, should these
³¹ tracks be merged, or left separate? If the reconstruction algorithms have found them to be
³² separate tracks then it is likely that it would be difficult to ascertain that they are from the
³³ same particle in real data, and so in considerations here they are not merged. One metric of
³⁴ efficiency would be to consider a track well reconstructed if it has a length between 75% and

5.3 Discerning reconstruction efficiencies



(a) Before calibration is performed.



(b) After calibration is performed.

Fig. 5.5 The number of hits as a function the hit $\frac{dE}{dx}$, before and after calibration of the response functions, for the conversion of ADC to number of electrons, for each plane is performed. The distribution of hit $\frac{dE}{dx}$ and the MPV of $\frac{dE}{dx}$ before calibration is shown top. The distribution of hit $\frac{dE}{dx}$ and the MPV of $\frac{dE}{dx}$ after calibration is shown bottom.

125% of the Monte Carlo truth length that the particle traversed in the detector, in which case track 1 would be considered well reconstructed. Another metric however would be to consider a track well reconstructed if the Monte Carlo truth distance the particle traversed in the detector is between 75% and 125% of the reconstructed length, in which case neither track would be considered well matched. Both metrics have used exactly the same tracks and a seemingly identical method of evaluating whether a track is well reconstructed or not, but have got the opposite results. As such it is wrong to say which consideration gives the correct result, but instead the result of each should be considered equally. It should also be

1
2
3
4
5
6
7
8

5.3 Discerning reconstruction efficiencies

36

1 noted that these are just two of a wide range of definitions one could use to quantify a well
2 reconstructed track. In discussions here the former definition of efficiency will be used, such
3 that a track is considered well reconstructed if:

- 4 • Reconstructed track length is more than or equal to 75% of the Monte Carlo track
5 length.
- 6 • Reconstructed track length is less than or equal to 125% of the Monte Carlo track
7 length.
- 8 • Only one reconstructed track can be matched per Monte Carlo particle.

9 When calculating efficiencies it is important to consider much more than just the ratio of
10 reconstructed to true track length. To this end efficiencies with regards to many aspects of
11 the tracks are calculated:

- 12 • Track length,
- 13 • Energy deposited in the active volume of the detector,
- 14 • The angle θ of the track, defined as the angle that a vector makes from the x axis in the
15 xy plane,
- 16 • The angle ϕ of the track, defined as the angle between the z axis and the vector.

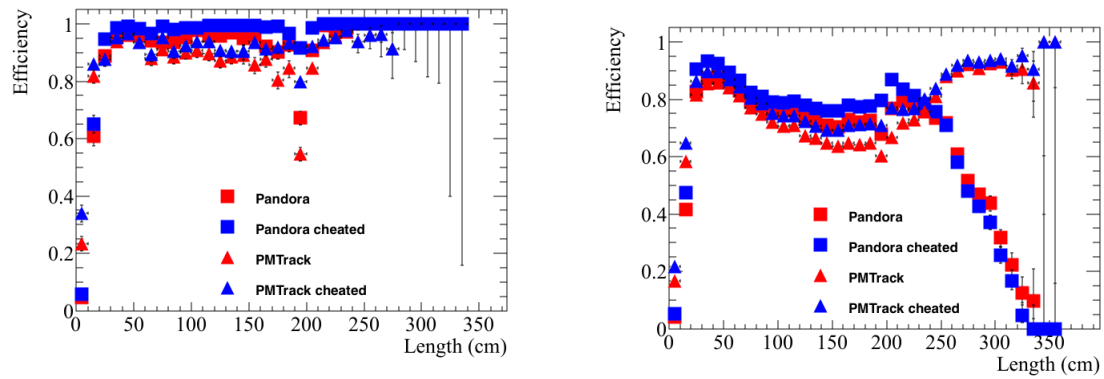
17 In all efficiency plots the Monte Carlo truth quantity, not the reconstructed quantity is shown
18 so as to reflect how the variations of these quantities affect the reconstruction efficiencies. It
19 is also useful to observe the effect on reconstruction of failed disambiguation and incorrect
20 interaction time determination. To show this, two forms of reconstruction are ran on the par-
21 ticles. One reconstruction path uses no Monte Carlo information and so the interaction time
22 is determined using the simulated photon detectors as described in Section 5.1. The second
23 reconstruction path uses cheated disambiguation and interaction time determination. Cheated
24 disambiguation means using the Monte Carlo truth information of the energy deposition to
25 correctly assign which wire segment the energy was deposited on.

26

27 The calculation of reconstruction efficiencies also serves as an effective method upon
28 which reconstruction algorithms can be further developed as it identifies aspects which do
29 not work as expected. For example when the efficiencies for the CRY sample were initially
30 calculated they were significantly lower than for the positive muon sample, but only when
31 disambiguation was not cheated. It transpired that this was because the disambiguation was
32 only selecting the largest collection of hits on each plane for each TPC. This is not a problem

when only 1 particle is simulated and will reduce the number of noise hits but in a CRY sample of 16 ms there will almost certainly be multiple particles in each TPC. Removing the hits from all but one of these multiple particles will cause them to have no reconstructed track, and thus cause the efficiency to drop significantly. Upon making the disambiguation algorithm no longer have this restriction the reconstruction efficiencies of the positive muon and CRY samples were observed to become much more similar.

The reconstruction efficiencies given the current state of the most commonly used reconstruction algorithms are shown in Figures 5.6, 5.7, 5.8, 5.9 and 5.10. Efficiencies are shown for both the positive muon and CRY samples, where it can be seen that the efficiency tends to be lower for the CRY sample. It is thought that this is due to the more complex event structure in the CRY sample, as multiple primary particles will be present in the detector at any given time. The relatively slow drift velocity of LAr may mean that these tracks cross in wire-tick space. Tracks crossing in wire-tick space could cause reconstruction errors as the overlaps may be mistaken for interactions, which would cause the tracks to be split, resulting in the interaction time calculated from the photon detectors to be incorrect. This error, in the calculation of interaction time using the photon detectors, was seen in Figure 5.4. The reconstruction efficiencies for the CRY sample are more realistic as events will rarely be isolated in the detector due to the large flux of cosmic particles on the Earth's surface.



(a) Reconstruction efficiencies for a positive muon sample.

(b) Reconstruction efficiencies for a CRY sample.

Fig. 5.6 The reconstruction efficiencies for simulated events as a function of Monte Carlo truth track length. The efficiencies are shown for 'non-cheated' reconstruction (in red), and 'cheated' reconstruction (in blue), for both Pandora (triangles) and PMTrack (squares).

A striking feature of Figure 5.6 is the rapid decrease in reconstructed efficiency for the CRY sample for track lengths above 250 cm when using Pandora. The cause of this is that

5.3 Discerning reconstruction efficiencies

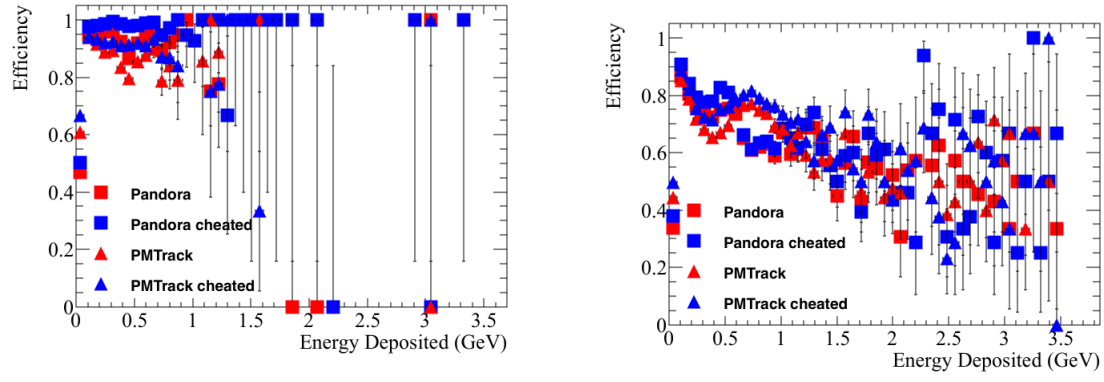


Fig. 5.7 The reconstruction efficiencies for simulated events as a function of Monte Carlo truth deposited energy. The efficiencies are shown for 'non-cheated' reconstruction (in red), and 'cheated' reconstruction (in blue), for both Pandora (triangles) and PMTrack (squares).

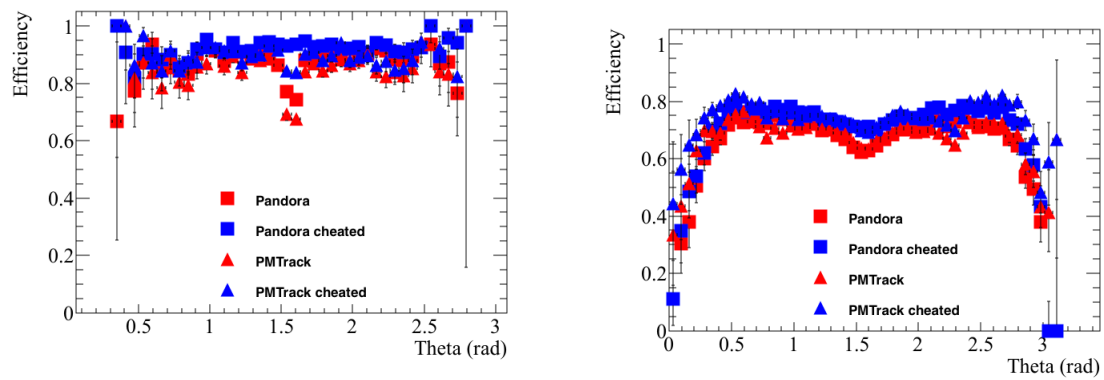
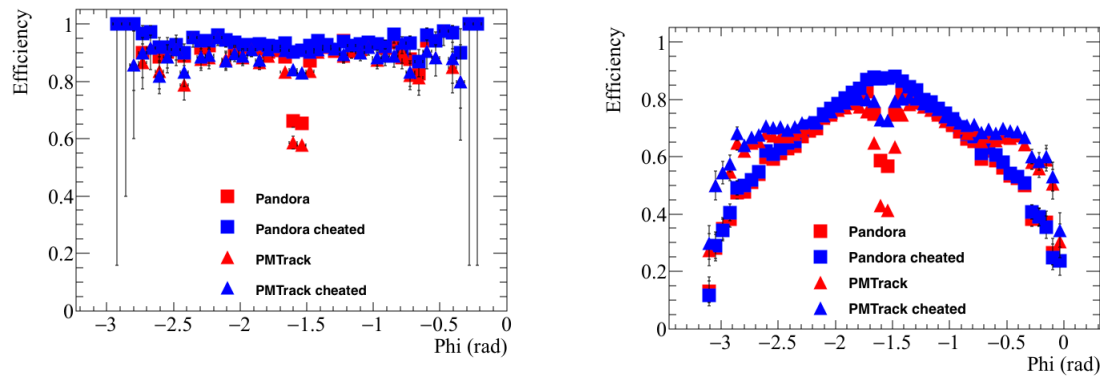


Fig. 5.8 The reconstruction efficiencies for simulated events as a function of Monte Carlo truth track angle in θ . The efficiencies are shown for 'non-cheated' reconstruction (in red), and 'cheated' reconstruction (in blue), for both Pandora (triangles) and PMTrack (squares).

- ¹ tracks are reconstructed separately in the long and short drift volumes before being merged
² when they are found to be co-linear in the yz plane. This is not a problem in the positive muon
³ sample as the x position of the hits calculated using Equation 5.1 will be correct. Where, x_{Hit}
⁴ is the calculated x position of the hit, T_{Hit} is the measured time of the hit, and v_{Drift} is the
⁵ electron drift velocity. An electron, in an electric field of 500 V cm^{-1} , in LAr, drifts at a
⁶ speed of $0.160563 \text{ cm } \mu\text{s}^{-1}$.

⁷
$$x_{Hit} = T_{Hit} \times v_{Drift} \quad (5.1)$$



(a) Reconstruction efficiencies for a positive muon sample.

(b) Reconstruction efficiencies for a CRY sample.

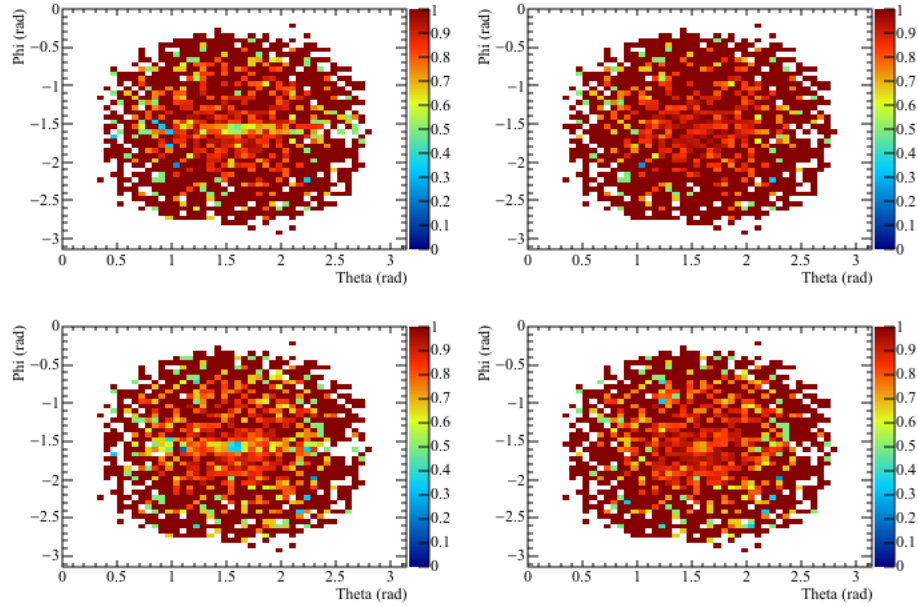
Fig. 5.9 The reconstruction efficiencies for simulated events as a function of Monte Carlo truth track angle in ϕ . The efficiencies are shown for 'non-cheated' reconstruction (in red), and 'cheated' reconstruction (in blue), for both Pandora (triangles) and PMTrack (squares).

However, when the same is done for hits in the CRY sample using particles with large interaction times, the x positions will have offsets proportional to the interaction time of the particle, unless the hit time is corrected by Equation 5.2. Where T_{Hit} is the corrected hit time, $T_{Measured}$ is the measured time of the hit, and $T_{Interaction}$ is the calculated interaction of the particle which caused the hit.

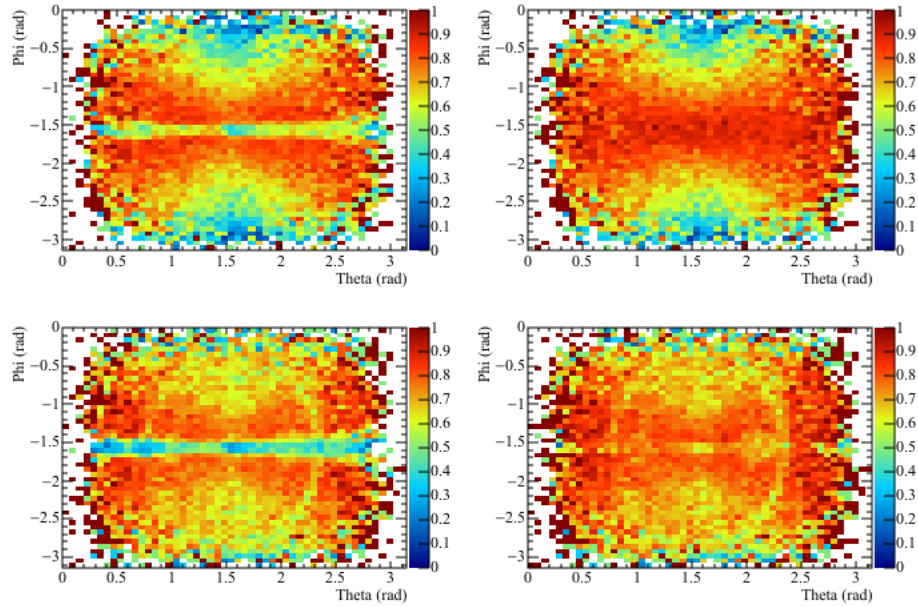
$$T_{Hit} = T_{Measured} - T_{Interaction} \quad (5.2)$$

This is due to particles being generated at large interaction times, as opposed to all at $T = 0$, as in the positive muons sample. For example, if a particle is generated at a time of $T = 12.5$ ms, then the offset in x position would be more than 20 m, using Equation 5.1. Obviously the hits could not have occurred at those positions, as the drift distances are roughly 30 cm in the 'short' drift volume, and 250 cm in the 'long' drift volume. However, if tracks which are reconstructed separately in the 'short' and 'long' drift volumes, are merged before this x offset is corrected for, then the combined track length will have a discontinuity in x of more than 40 m! As the interaction time of the track is calculated using the output of the tracking algorithms it is not possible to prevent this by using the interaction time at present. It is however, possible to subtract this jump in x position from the track length quantity which is calculated when the stitched track is stored in the event. This will give the correct track length, though the user will still have to correct individual hit positions in later analyses, using the calculated interaction time. This is what is done by PMTrack, hence it is not exhibiting this rapid decrease in reconstruction efficiency for long tracks. The interaction

5.3 Discerning reconstruction efficiencies



(a) Reconstruction efficiencies for a positive muon sample.



(b) Reconstruction efficiencies for a CRY sample.

Fig. 5.10 The reconstruction efficiencies for simulated events as a function of Monte Carlo truth track angle in θ and ϕ . The track angle in θ is shown on the x axis, and the track angle in ϕ is shown on the y axis. The colour z axis shows the reconstruction efficiency. The efficiencies are shown for non-cheated reconstruction (plots on the left) and cheated reconstruction (plots on the right) for both Pandora (plots on the top) and PMTrack (plots on the bottom).

time can be found from, among other things, the Monte Carlo truth generation time, or the photon detectors.

It is clear from Figure 5.6 that particles with track lengths less than 30 cm are poorly reconstructed. The very low efficiency for particles with track lengths less than 10 cm can be partially attributed to, Monte Carlo truth particles with track lengths of less than 1 cm, in the active volume of the detector. These particles, which represent 30% of the particles with active volume track lengths of less than 10 cm, are too short to be reconstructed using the current reconstruction process. These particles will need to be reconstructed when looking for supernovae bursts, though special algorithms will be written to do this, as the traditional hit finding and clustering algorithms may discard them due to the isolated nature of the hits. Another issue is that the low energies of these particles may mean that the signals that they produce are below threshold and so will not even be reconstructed, or if hits are reconstructed, they may be too close to a more energetic track, and get absorbed into them. The reconstruction of tracks is affected by the number of wires which they cross, though this should not matter for particles with lengths of more than 5 cm in the active volume, as they will have crossed roughly 10 wires in each plane, which should produce enough unique hits for a cluster to be reliably constructed. This can be seen to be the case for PMTrack when considering the positive muon sample, as the efficiency for particle track lengths between 10 and 20 cm is roughly the same as that for track lengths between 20 and 30 cm, however when considering the CRY sample there is still a significant decrease in efficiency. This is attributed to secondary particles which are produced in hadronic interactions with the concrete surrounding the detector. Many of these particles will travel only very short distances in the active volume, though those that travel slightly larger distances are likely to cause energy depositions that will be confined to the detector edges. The tracking algorithms may struggle to accurately reconstruct these tracks, as significant portions of the track will be close to the detector edge, where the field is poorly modelled and hits may be more difficult to disambiguate.

The trend of increasing efficiency for longer track lengths from Figure 5.6 can also be seen in Figure 5.7 as the amount of deposited energy increases. This is because particles which deposit more energy will tend to have travelled further in the detector. The amount of energy that particles deposit is limited by the size of the detector, as particles with an energy of more than 1 GeV are energetic enough to be MIPs. This results in few particles depositing more than 1 GeV in the detector. The result of this is that the uncertainty in the reconstruction efficiency increases above 1 GeV. The larger range in the amount of energy deposited seen in Figure 5.7b, is due to the larger number of muons in the CRY that create

5.4 Performing particle identification

42

¹ large electromagnetic showers upon entering the LAr.

²

³ It is also interesting to note the pronounced decreases in reconstruction efficiencies for
⁴ particular angles, shown in Figure 5.8 and Figure 5.9. The decrease in efficiency at $\phi = \frac{\pi}{2}$
⁵ can be attributed to the drop in efficiency for particles with track lengths between 190 cm
⁶ and 200 cm. This is because the vertical height of the detector is approximately 195 cm,
⁷ and near vertical tracks will hit few collection wires, meaning that determining the triple
⁸ points needed by the disambiguation is very difficult. This is verified by the large increase
⁹ in efficiency achieved by cheating the disambiguation, as seen in Figure 5.8a, where the
¹⁰ reduction in reconstruction efficiency is seen to become much less pronounced. Similarly the
¹¹ decrease in efficiency at $\theta = \frac{\pi}{2}$ can be attributed to particles which are perpendicular to the
¹² collection wires resulting in few collection wires being hit.

¹³

¹⁴ The information from Figures 5.8 and 5.9 is combined in Figure 5.10, where the sharp
¹⁵ drop in efficiency at $\phi = \frac{\pi}{2}$ for the 'non-cheated' CRY sample, is particularly visible. The
¹⁶ effect of cheated disambiguation is clear in Figure 5.10b where the dip in efficiency as a
¹⁷ function of θ at fixed $\phi = \frac{\pi}{2}$ is completely removed. The same is not true however, for the
¹⁸ dip in efficiency as a function ϕ at fixed $\theta = \frac{\pi}{2}$, though the reduction in efficiency was not
¹⁹ as severe as that seen for fixed values of $\phi = \frac{\pi}{2}$. The effect of 'cheated disambiguation'
²⁰ can still be seen though, as the reconstruction efficiency in Figure 5.10b can be seen to
²¹ improve for values of ϕ . There are still however, noticeable decreases in the reconstruction
²² efficiency for values of ϕ close to 0 or π , when using Pandora. The improvement in the
²³ performance of the reconstruction algorithms that comes from 'cheating' the reconstruction
²⁴ is part of the motivation for the wire pitches in the DUNE FD being 36° as opposed to the
²⁵ $45 \pm 0.7^\circ$ used in the 35 ton. This is because, as discussed in Section 3.5, the shallower wire
²⁶ pitch makes disambiguation easier. Though disambiguation will be easier in the different
²⁷ geometry, further efforts to improve disambiguation are still required, as are continued efforts
²⁸ to reconstruct the shortest tracks.

²⁹

³⁰ 5.4 Performing particle identification

³¹ Being able to perform reliable particle identification (PID) is a key requirement for the
³² DUNE experiment, and so efforts have been made to establish a procedure by which this can
³³ be achieved. The predominant method of performing PID in LAr is to use the relationship
³⁴ between $\frac{dE}{dx}$ and the residual range of the track, defined as being the distance between a point

5.4 Performing particle identification

43

on the track and the stopping point of the track. This relationship is observed to be dependent on particle mass and is quantified by the Bethe-Bloch equation [21] [22] which is shown in Figure 5.11 and presented in Equation 5.3.

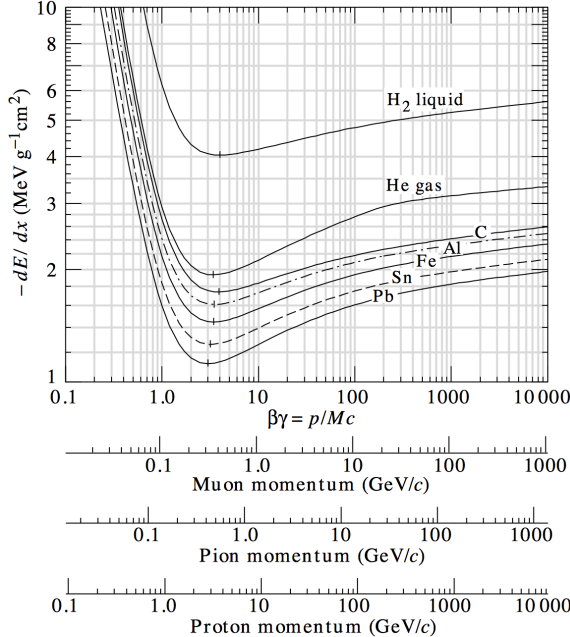


Fig. 5.11 The mean energy loss per unit track length of different particle masses in different materials [23]. The $\frac{Z}{A}$ of Liquid Argon is slightly less than that of Carbon.

$$-\frac{dE}{dx} = Kz^2 \frac{Z}{A} \rho \frac{1}{\beta^2} \left[\frac{1}{2} \ln \frac{2m_e c^2 \beta^2 \gamma^2 T_{max}}{I^2} - \beta^2 - \frac{\delta(\beta \gamma)}{2} \right] \quad (5.3)$$

The sharp increase in energy loss per unit length can be seen to occur at different momenta for different particle masses meaning that the peak value of $\frac{dE}{dx}$ can change significantly. When comparing muons and protons, it can be seen that the momenta at which the $\frac{dE}{dx}$ increases is very different. When muons and pions are compared, it can be seen that the momenta at which an increase occurs is very similar.

The particle mass dependence can be seen by plotting the $\frac{dE}{dx}$ against the residual range of the particle on a log-log plot, as shown in Figure 5.12. A power law dependence is found to describe the relationship [19], as shown in Equation 5.4.

$$\frac{dE}{dx} = AR^b \quad (5.4)$$

5.4 Performing particle identification

Table 5.1 Stopping power parameterisation for various particle types in liquid Argon. The table is taken from [19].

Particle	A (MeV cm ^{b-1})	b
Pion	8	-0.37
Kaon	14	-0.41
Proton	17	-0.42
Deuteron	25	-0.43

- ¹ The dependence on b is found to be weak, and so can be set to -0.42 for all particle masses.
² This means that the main discriminant used is the A parameter, which has a strong dependence
³ on particle mass. The values for A and b calculated from Figure 5.12 are shown in Table 5.1.
⁴ It is found that the error introduced by fixing the b parameter is small compared to the error
⁵ from ionisation fluctuations.

⁶

- ⁷ Once the b parameter is set to be constant for all particle types it is possible to calculate
⁸ a value for the A parameter for each hit on the track using Equation 5.5, where R_i is the
⁹ residual range of the track at that point.

$$\text{10} \quad A_i = \left(\frac{dE}{dx} \right)_i \times (R_i)^{0.42} \quad (5.5)$$

- ¹¹ The particle type discriminant, called PIDA, can then be calculated for a track by finding the
¹² average value of A_i for the track. As the particle mass dependant increase in $\frac{dE}{dx}$ only occurs
¹³ near the end of the track, the PIDA variable can only be calculated for particles which stop
¹⁴ in the detector as all other particles will have MIP-like $\frac{dE}{dx}$ distributions and so cannot be
¹⁵ identified in this way. As shown by the plotted range of Figure 5.12 the average value of A is
¹⁶ normally calculated for the last 30 cm of the track.

¹⁷

- ¹⁸ The PIDA method was tested in [19], where the PIDA values were calculated for sim-
¹⁹ ulated particles which stopped in the detector, using truth information over the last 30 cm
²⁰ of the particle tracks. This is shown in Figure 5.13, where a clear separation can be seen
²¹ between the peaks for muons, pions, kaons and protons. Though the muon and pion peaks
²² are relatively close together they can still be resolved in the plot due to little overlap. It is
²³ interesting to note how tight the PIDA distributions found in the paper are, which allows the
²⁴ different particles types to cleanly separated in the truth study. The author notes that an incor-
²⁵ rect tuning of the electron recombination effects will cause the distributions in Figure 5.13
²⁶ to become broader. The dependence of $\frac{dE}{dx}$ on the recombination effects ($Recomb_X$) were

5.4 Performing particle identification

45

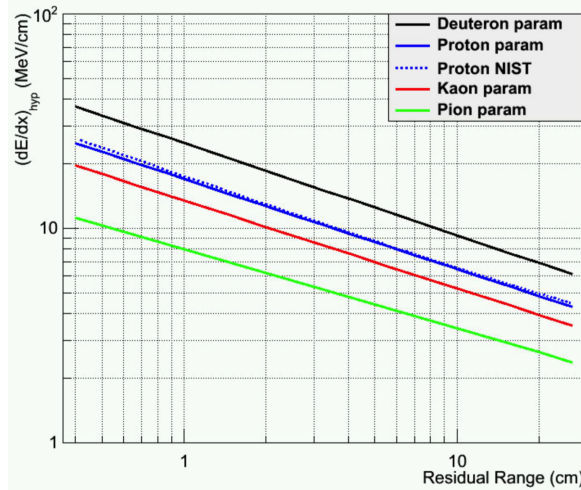


Fig. 5.12 Stopping power for different particle masses as a function of residual range in liquid Argon. The figure is taken from [19].

presented in Equations 3.1 and 3.2. The author also notes that an incorrect calibration of the detector will introduce a systematic shift in the expected values of PIDA, this is why the work presented in Section 5.2 is important.

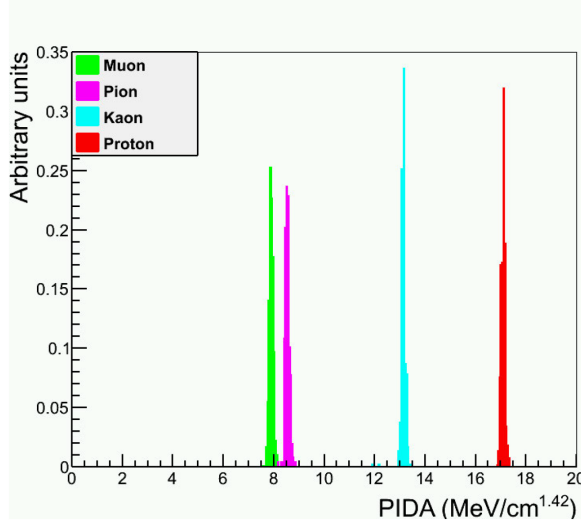


Fig. 5.13 The distribution of PIDA values, calculated using Monte Carlo truth, for different particle masses. The figure is taken from [19].

From Figure 5.13 it can be seen that the most distinct PIDA distributions are that of muons and protons, these are also two of the most common particle types in cosmic rays. For these reasons particle identification using the PIDA variable will be attempted on simulations of the 35 ton. As outlined in Sections 5.1 and 5.2 in order to do this the interaction times of

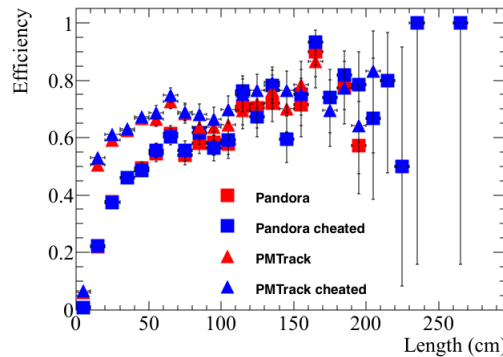
1
2
3
4

5
6
7
8

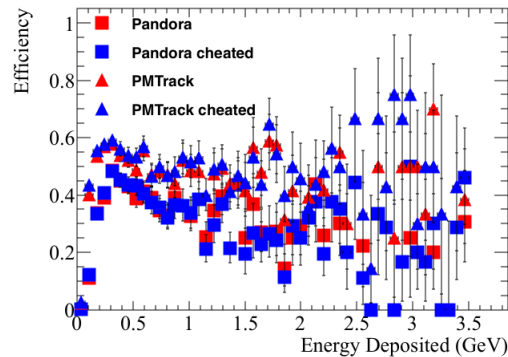
5.4 Performing particle identification

1 particles have to be well known and the calibration constants must be tuned so as to ensure
 2 that the effects of recombination are properly accounted for. It is also useful to use the
 3 information found in Section 5.3 about the efficiency with which tracks are reconstructed. In
 4 this regard it is useful to produce additional figures showing the reconstruction efficiencies
 5 of protons in the CRY sample, these are shown in Figure 5.14.

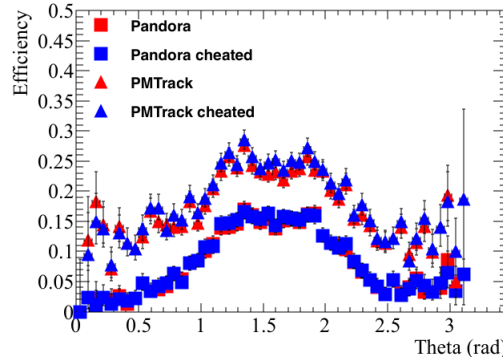
6



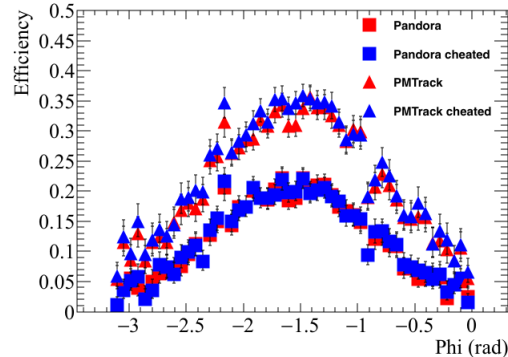
(a) The reconstruction efficiency as a function of Monte Carlo truth track length.



(b) The reconstruction efficiency as a function of Monte Carlo truth deposited energy.



(c) The reconstruction efficiency as a function of Monte Carlo truth track angle in θ .



(d) The reconstruction efficiency as a function of Monte Carlo truth track angle in ϕ .

Fig. 5.14 The reconstruction efficiencies for protons in a sample generated using CRY. Top left, shows the efficiencies as a function of Monte Carlo truth track length. Top right, shows the efficiencies as a function of Monte Carlo truth deposited energy. Bottom left, shows the efficiencies as a function of Monte Carlo truth track angle in θ . Bottom right, shows the efficiencies as a function of Monte Carlo truth track angle as a function of ϕ . The efficiencies are shown for 'non-cheated' reconstruction (in red), and 'cheated' reconstruction (in blue), for both Pandora (triangles) and PMTrack (squares).

7 Figure 5.14 shows that the average reconstruction efficiency for PMTrack is higher than
 8 that for Pandora when considering protons. This can be easily seen in Figure 5.14c where

the efficiency for PMTrack is roughly 10% higher than that for Pandora, for all values of θ . The reconstruction efficiency is still much lower than the overall efficiency shown in Figure 5.8, for both the positive muon and CRY samples though. This shows that the overall reconstruction efficiency for protons is quite low. Comparing Figures 5.6b and 5.14a, it is evident that the reconstruction efficiency for protons with track lengths of more than 10 cm is reasonably similar, to that of the overall reconstruction efficiency for the CRY sample, when using PMTrack. However, the reconstruction efficiency is significantly lower for protons with tracks of less than 10 cm. When using Pandora to reconstruct protons, the reconstruction efficiency is lower for all track lengths. It is found that 60% of simulated protons have track lengths of less than 1 cm, and that none of these particles are reconstructed. It is this large number of very short particles which causes the overall reconstruction efficiency to be relatively low. When particles with track lengths of less than 1 cm (10 cm) are removed, the average reconstruction efficiency for PMTrack rises to 37% (58%). This shows that, when the shortest tracks are not counted the reconstruction performs reasonably well.

It is also useful to produce samples where the primary particle is a single muon or proton located in the active volume of the detector. This allows for a sample of isolated tracks to be made upon which the capabilities of the PIDA metric can be tested. It also allows the reconstruction efficiency to be found for particles in isolation. The properties of the generated particles are illustrated below in Table 5.2. The values of the simulated quantities were found by changing the given parameters by an amount taken from a random sampling of a Gaussian distribution of width equal to the error listed. These simulation parameters were chosen to produce samples which would contain both exiting and stopping particles whilst generating the particles in the LAr would ensure that there should always be a reconstructable track in the detector. The reconstruction efficiencies when using the PMTrack reconstruction method are shown for the simulated particles in Figure 5.15.

Particles with track lengths of less than 1 cm have been excluded from these plots which is why the angular reconstruction efficiencies for protons in Figures 5.15c and 5.15d, are higher than those seen in Figures 5.14c and 5.14d. This was done as none of these particles were reconstructed due to the very short distances which they travel. After discounting these very short particles, the efficiencies generally follow similar patterns observed in the earlier efficiency plots, though there is a decrease in efficiencies for the longest track lengths which is not observed in other samples. This is attributed to the initial positions of the particles being within the detector volume, as this means that any particle travelling over 100 cm would have a very peculiar trajectory as the edge of the detector should never be more than 100 cm

5.4 Performing particle identification

Table 5.2 The properties of initial particles simulated in the muon and proton samples. The angles θ_{xz} and θ_{yz} are defined as the angle that a vector makes in the xz and yz planes respectively.

	Muon properties	Proton properties
Initial position (cm)	($100 \pm 50, 0 \pm 30, 80 \pm 20$)	($100 \pm 50, 0 \pm 30, 80 \pm 20$)
Initial momentum (GeV)	0.3 ± 0.1	0.8 ± 0.5
Initial θ_{xz} ($^{\circ}$)	0 ± 180	0 ± 180
Initial θ_{yz} ($^{\circ}$)	-45 ± 45	-45 ± 45

¹ away from the starting position. The only exception to this is if a particle travelled along
² the x axis to the other end of the detector, which, as discussed earlier, is a very problematic
³ orientation to reconstruct as all of the charge would be deposited over a large range of time
⁴ on very few collection plane wires.

⁵
⁶ As the increase in $\frac{dE}{dx}$ is only visible when the particle stops in the detector it is necessary
⁷ to remove exiting particles from the sample by applying a fiducial cut on the end point of the
⁸ reconstructed track. It is important to only place this on the end point of the track, as one does
⁹ not want to remove particles which enter the detector and then stop. When calorimetry is
¹⁰ performed, the end point of the track is determined using, among other metrics, the increase
¹¹ in $\frac{dE}{dx}$ and so the residual range of the track (a stored data member of the track object), should
¹² always refer to the distance to the end of the particles trajectory. For this study a fiducial cut of
¹³ 5 cm is used, meaning that any track with hits within 5 cm of the edge of the detector volume
¹⁴ is discarded, and counted as an exiting particle. This should mean that very few tracks due to
¹⁵ exiting particles are identified as stopping in the detector, as it would require the reconstruc-
¹⁶ tion algorithms to miss large section of the track. This will mean that some stopping particles
¹⁷ are incorrectly assigned as exiting particles, causing the identification efficiency to drop, but
¹⁸ it is necessary to ensure that exiting particles are not included in the final distributions. A
¹⁹ further cut that is applied, is the requirement that there are a minimum of 5 collection plane
²⁰ hits, this is to ensure that an adequate number of points are taken upon which to find an
²¹ average value of PIDA for the track. Similar cuts are described in [19], and the resulting
²² distributions of PIDA values for the single proton and muon samples are shown in Figure 5.16.

²³
²⁴ As can be seen from Figure 5.16 using truth information can make the distributions much
²⁵ cleaner, particularly when discounting particles for which the reconstruction algorithms
²⁶ do not track to their end point. A track is identified as having a correct end point if the
²⁷ reconstructed end point is within 2.5 cm of the true end point of the particle. It is reassuring to

5.4 Performing particle identification

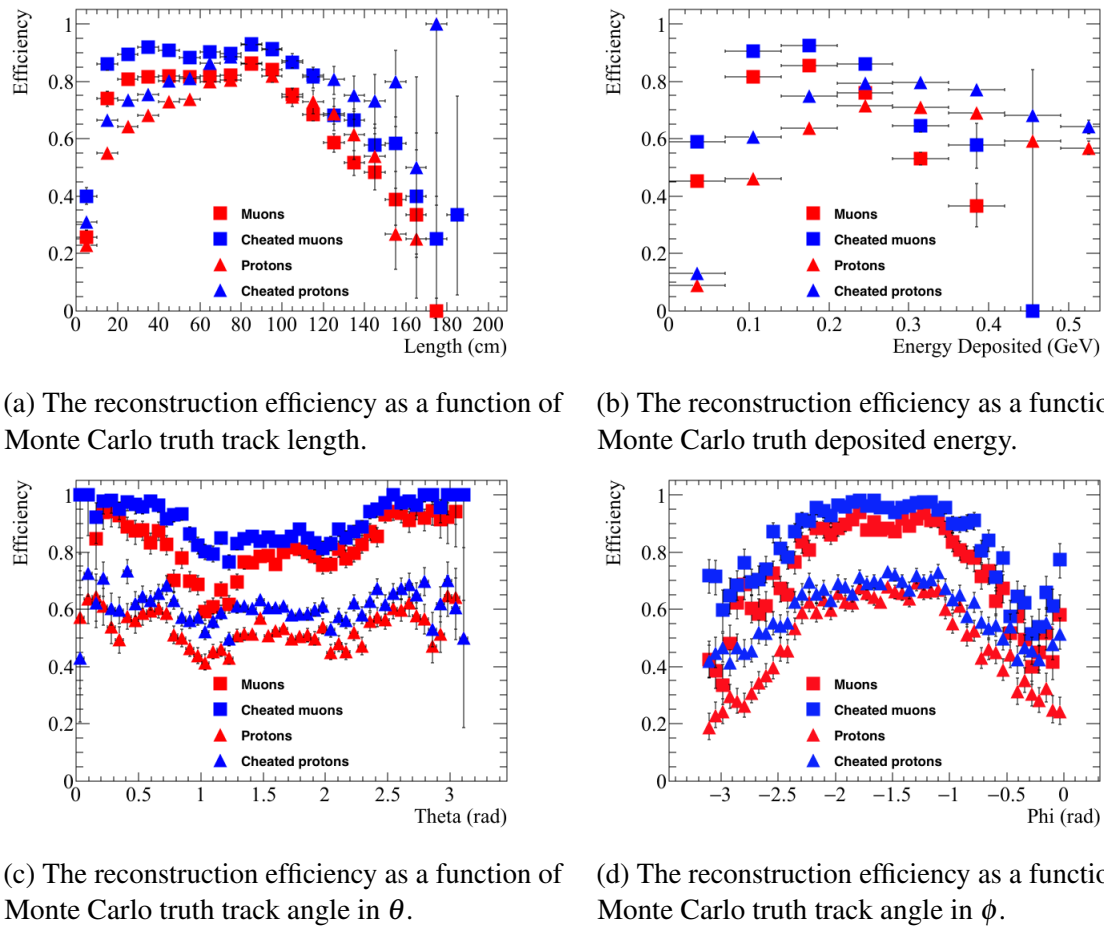
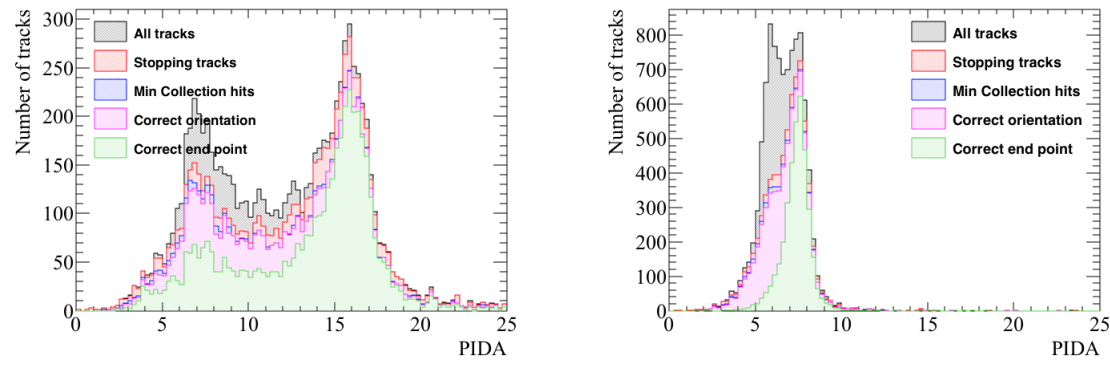


Fig. 5.15 The reconstruction efficiencies for single muons and protons in the 35 ton. Top left, shows the efficiencies as a function of Monte Carlo truth track length. Top right, shows the efficiencies as a function of Monte Carlo truth deposited energy. Bottom left, shows the efficiencies as a function of Monte Carlo truth track angle in θ . Bottom right, shows the efficiencies as a function of Monte Carlo truth track angle as a function of ϕ . The efficiencies are shown for non-cheated reconstruction (red blocks) and cheated reconstruction (blue blocks) for both muons (square blocks) and protons (triangle blocks).

see that few tracks are reconstructed backwards, as if this were not the case then performing particle identification would be very difficult, as it would indicate that the calorimetry and tracking algorithms are not performing well. Improvements can still be made though, as both plots in Figure 5.16 contain tracks which do not have the final energy depositions. This can be seen as when the requirement that the reconstructed track end point is consistent with the true end point, the low tails of the PIDA distributions are significantly reduced. This is most noticeably the case in Figure 5.16a, where the peak at low values of PIDA is significantly reduced. It is observed that the PIDA distributions are cleaner when information from all

1
2
3
4
5
6
7
8

5.4 Performing particle identification



(a) The PIDA values calculated for the single proton sample. (b) The PIDA values calculated for the single muon sample.

Fig. 5.16 The calculated PIDA values for single muons and protons in the 35 ton. A series of criteria designed to select only tracks due to stopping particles which have a required number of collection plane hits is applied. The tracks are then further refined using truth information such as the true end point of the particle.

1 three wire planes are used, as opposed to only using the collection plane, and so this is
 2 presented here. This shows how important it is to calibrate the electronics responses of all
 3 three wire planes, and how additional wire planes can improve calorimetry, as well as the
 4 accuracy of reconstruction algorithms.

5
 6 The relationship between the $\frac{dE}{dx}$ and residual range of a track is shown in Figure 5.17
 7 for both protons and muons. The much steeper increase in $\frac{dE}{dx}$ at low residual range for
 8 protons compared to muons is clearly visible when comparing Figures 5.17a and 5.17b. The
 9 contamination in the proton sample at low PIDA can be seen in Figure 5.17a where there is
 10 a clear sample of tracks for which the $\frac{dE}{dx}$ does not increase for low residual ranges. These
 11 plots are filled after tracks whose end points do not correlate with the true end points, are
 12 removed, and so the tail of low $\frac{dE}{dx}$ values is due to particles for which the simulated detector
 13 did not find increased energy depositions as the particle stopped. It is therefore possible that
 14 at least some of these protons do not in fact stop, but interact inelastically when they still
 15 have a significant amount of kinetic energy meaning that GEANT4 will create a new particle
 16 and that the tracking algorithms are creating a new track after this interaction.

17
 18 It is useful to summarise the information shown in Figure 5.16 in a table so that an
 19 efficiency of identifying stopping particles can be found. This is shown in Table 5.3 for
 20 protons, and in Table 5.4 for muons. The efficiency shown in these tables is defined as the
 21 number of tracks in the PIDA range, divided by the total number of stopping particles. This

5.4 Performing particle identification

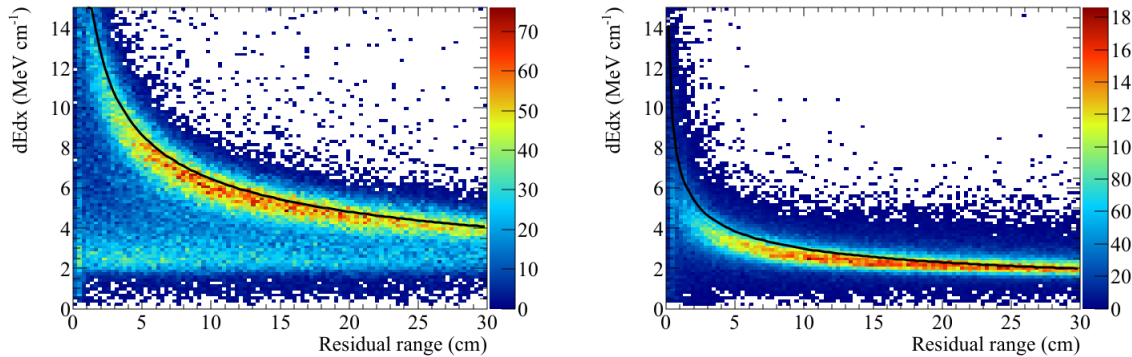
(a) The $\frac{dE}{dx}$ versus residual range plot for the single proton sample.(b) The $\frac{dE}{dx}$ versus residual range plot for the single muon sample.

Fig. 5.17 The measured relationship between $\frac{dE}{dx}$ and residual range for single muons and protons in the 35 ton. These plots are made after applying all of the cuts outlined in Figure 5.16, meaning that only hits from tracks whose end points are consistent with the true end points are plotted.

means that, should more reconstructed tracks have PIDA values within the PIDA range than there are stopping particles, then the efficiency can be more than 100%. This is the case in Table 5.4. The purity shown in these tables is defined as the percentage of tracks in the PIDA range, which are associated with particles that stop in the detector. As many of the tracks shown in the 'reconstructed tracks' row in Table 5.4, are not due to stopping particles the purity is low, but this increases markedly after the fiducial cut is applied. The PIDA ranges referred to are 14-18 and 5-9 for protons and muons respectively, as these ranges cover the peaks of the distributions shown in Figure 5.17, and are centred on the peaks in Figure 5.13.

As can be seen in Table 5.3, the efficiency upon which protons can be identified does not change significantly as the sequential criteria are applied, but, as shown in Figure 5.16a, the peak at low values of PIDA decreases significantly. The same cannot be said for the muon sample however, as when the criteria that the tracking end point matches the true end point is applied, a significant section of the tail within the PIDA range is removed which significantly reduces the PIDA efficiency. However, the resulting distribution is more similar to that shown in Figure 5.13, showing that the particles which survive the cut are those that are very well reconstructed. The cut to remove tracks that do not have the correct end points reduces both sets of efficiencies, but, if all particles were reconstructed with the correct end points, then one can imagine that the number of tracks within the PIDA ranges would increase, and the distributions would become more symmetrical, as shown in Figure 5.16b. Both tables also exhibit high purities, which shows that the fiducial cut designed to removing exit-

5.4 Performing particle identification

52

Table 5.3 A summary of the PIDA values calculated for the proton sample as sequential cuts are applied.

Applied cut	Proton sample			
	Tracks	In PIDA range	Efficiency	Purity
Total stopping particles	13295			
Reconstructed tracks	8761	3009	22.6%	98.7%
Survives 5 cm fiducial cut	7552	2894	21.8%	99.9%
Minimum of 10 collection plane hits	6186	2507	18.9%	99.9%
Correct track orientation	6022	2491	18.7%	99.9%
Correct tracking end point	4432	2288	17.2%	100%

Table 5.4 A summary of the PIDA values calculated for the muon sample as sequential cuts are applied.

Applied cut	Muon sample			
	Tracks	In PIDA range	Efficiency	Purity
Total stopping particles	6880			
Reconstructed tracks	9883	8907	129%	67.4%
Survives 5 cm fiducial cut	7126	6259	90.9%	90.2%
Minimum of 10 collection plane hits	6580	5876	85.4%	89.9%
Correct track orientation	6436	5767	83.8%	90.1%
Correct tracking end point	3676	3555	51.7%	100%

¹ ing particles is effective, with only 2 exiting protons being mis-identified in the proton sample.

²

³ From Table 5.3 it can be seen that there are more stopping protons than primary protons,
⁴ as only 10,000 primary protons were generated. The effectiveness of the PIDA algorithm
⁵ at identifying only primary protons is shown in Table 5.5. Comparing both tables, it can be
⁶ seen that the efficiency with which the primary protons can be identified, is larger than the
⁷ secondary protons, as the efficiencies shown in Table 5.3 are lower than those in Table 5.5. It
⁸ is thought that this is due to the low reconstruction efficiency for particles with the shortest
⁹ track lengths, as many of the secondary protons will have, as discussed in Section 5.3. A
¹⁰ similar table is not produced for primary muons as there were no secondary muons produced
¹¹ in the muon sample, and so Table 5.4 is itself the efficiency with which the primary muons
¹² can be identified.

¹³

5.4 Performing particle identification

Table 5.5 A summary of the PIDA values calculated for the primary particles in the proton sample as sequential cuts are applied.

Applied cut	Proton sample			
	Tracks	In PIDA range	Efficiency	Purity
Total stopping particles	7798			
Reconstructed tracks	5920	1937	24.8%	98.9%
Survives 5 cm fiducial cut	5044	1878	24.1%	99.9%
Minimum of 10 collection plane hits	4485	1711	21.9%	99.9%
Correct track orientation	4363	1707	21.9%	99.9%
Correct tracking end point	3122	1565	20.1%	100%

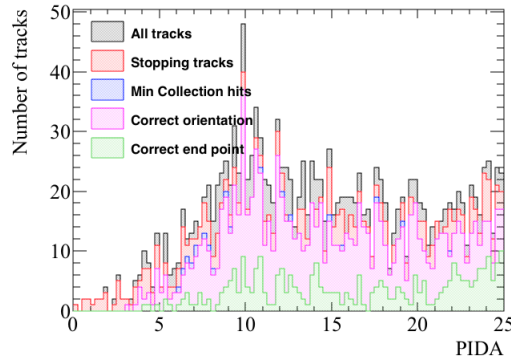
Upon verifying that the PIDA metric can reliably determine particle type when they are simulated in isolation, the next step is to observe the accuracy upon which particles can be identified in a CRY sample. The sample used here differs from the CRY sample used earlier in that only events which contain a proton in the detector are reconstructed. This is done to reduce simulation time and storage space, as this cut will still provide a substantial number of muons, whilst ensuring that a large proton sample can be reconstructed. The process of calculating PIDA values for tracks is identical in all samples, though as discussed in Section 5.3 the much more complicated event structure in the CRY sample affects the reconstruction efficiency, and so will likely also affect the accuracy of the calorimetry. The calorimetry will be affected in two ways, firstly, the reduced performance of the reconstruction algorithms will mean that some particles are not reconstructed at all, whilst those that are reconstructed may be more likely to have missing hits, and so the end points may be reconstructed less accurately. This will cause the tail of low $\frac{dE}{dx}$ values, seen in Figure 5.17a, to be more pronounced. Secondly, though the photon detector time determination is very accurate for a large number of tracks it is also incorrect for a number of tracks, as shown in Figure 5.4. This will cause the recombination correction to be miscalculated, which will in turn increase the calculated $\frac{dE}{dx}$, and hence PIDA values.

The PIDA values calculated for protons and muons in the CRY sample are shown in Figure 5.18. As can be seen from Figure 5.18b, there is a tail of very high PIDA value muon tracks which contaminate the proton PIDA region of interest (ROI). This causes a serious problem when trying to identify protons from a cosmic sample, as the muon flux is significantly higher than the number of protons. The result of this will be a sample of tracks which will not be very pure, and so further cuts will have to be developed to enhance the purity of this sample whilst not reducing the efficiency upon which proton tracks are

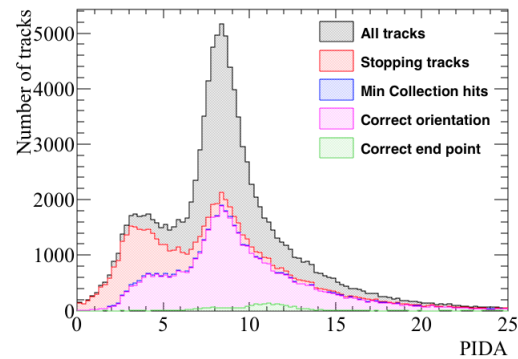
5.4 Performing particle identification

1 identified.

2



(a) The PIDA values calculated for protons.



(b) The PIDA values calculated for muons.

Fig. 5.18 The calculated PIDA values for muons and protons in a CRY sample through the 35 ton. A series of criteria designed to select only tracks due to stopping particles which have a required number of collection plane hits is applied. The tracks are then further refined using truth information such as the true end point of the particle.

Chapter 6

The 35 ton data sample

The data taking period for the 35 ton prototype was from November 2015 until March 2016. This included an extensive commissioning period before the detector was filled with LAr, and the electric field was turned on. During this time many of the features of the data discussed below were first noticed, and attempts to rectify these were pursued. A long commissioning period was also required because many of the DAQ sub-systems were still under active development in November.

A total of 22 days worth of data was collected with the electric field set at 250 V cm^{-1} , the breakdown of when these periods occurred is shown in Figure 6.1. It is clear that the analysable data is interspersed with data where the electric field was not turned on, this is both due to extenuating circumstances such as a site wide power outage in early March, and a dedicated two week noise hunting exercise in February. The physics data taking period ended at 3am on 19th March 2016, when a filtration pump broke causing an unrecoverable loss of purity as air was pumped into the detector. Following this studies to understand the electronics noise and to test the high voltage systems continued, but it was deemed too costly to acquire any more physics data. During this time the electric field was raised to the nominal value of 500 V cm^{-1} , and some of the causes of the higher than expected noise levels were discerned.

6.1 Organisation of the data structure

As previously noted the 35 ton consisted of three detector sub-systems: RCEs collecting TPC data, SSPs collecting photon detector data, and CRCs tagging cosmic rays. The DAQ combined these three data streams into synchronous events in time and saved them as LArSoft

6.1 Organisation of the data structure

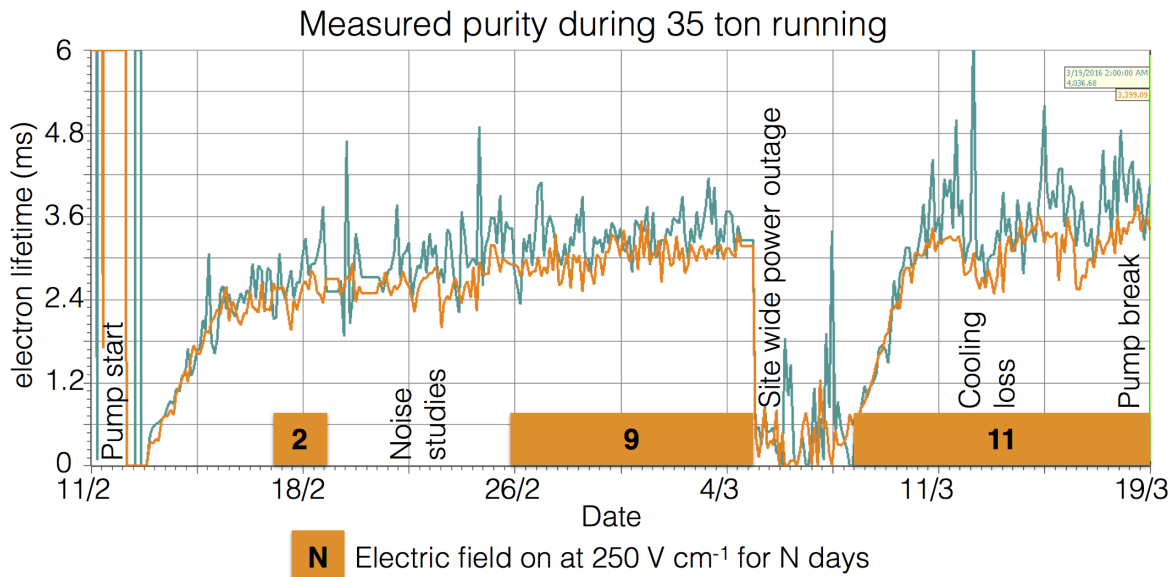


Fig. 6.1 Timeline showing the data collected during the 35 ton Phase II run once the purification pumps were turned on.

¹ data objects. These data objects would later have to be converted to the offline data products,
² which the reconstruction tools developed on simulation used, this is discussed in Section 6.2.
³ This section describes the structure of the data objects in the raw form.

⁴
⁵ During operations the DAQ was configured to maximise data throughput and physics
⁶ potential. This meant recording different lengths of times for each of the three sub-systems,
⁷ as the data volumes and length of physics information were significantly different. For
⁸ example, due to the emission of prompt light, the physics information from the SSPs is of a
⁹ much shorter length of time than the physics information from the RCEs, where data has to be
¹⁰ recorded whilst the electrons drift through the LAr. During the running period the recorded
¹¹ data was triggered by through-going muons which produced coincidences on the CRCs on
¹² opposite side of the cryostat. A coincidence is defined as two CRC modules recording a hit
¹³ within 30??? ns. The system used to collect the CRC data was also responsible for generating
¹⁴ the triggers, and so this meant that the trigger rate could be suppressed to approximately 1 Hz,
¹⁵ by only producing triggers every N times a coincidence occurred, where N was a tuneable
¹⁶ variable. A trigger rate of 1 Hz was used as the maximum speed at which data could be
¹⁷ written to disk was approximately 60 MB s⁻¹, which is roughly equal to the size of each
¹⁸ triggered event when the entire detector is read-out in the configuration discussed below. The
¹⁹ rate at which events were recorded could have been increased if zero-suppression of the TPC

6.1 Organisation of the data structure

57

data had been used, however the noise level meant that this was not feasible. 1

With an electric field of 250 V cm^{-1} , and a drift of 2.25 m, the drift time for electrons at the long drift CPA was roughly 2.6 ms or 5200 ticks (where 1 tick is 500 ns). It was decided that in order for a track causing a counter coincidence to be separated from other tracks, it was necessary to have roughly one drift window both before, and after, the drift window around the coincidence. This means that data was recorded for 7.5 ms, or 15,000 ticks, around each coincidence. The SSPs only collected the prompt light from through-going particles, and so only $200 \mu\text{s}$ of SSP data was recorded for each event. The CRCs produced the least volume of data, and so were able to be read out constantly. 10

As the run mode required accessing buffered data, it had to be discretised inside the components before being sent to the event builders in the DAQ. In the discussion of how this worked, focus will be given on the RCE data where some new terms need to be introduced. The smallest unit of data, called a nanoslice, is the data from one RCE for one tick, where each RCE controls 128 channels meaning that there were a total of 16 RCEs in the 35 ton. A microslice is then made by combining $1000 \times N$ nanoslices such that it contains 0.5 ms (1,000 ticks) of data across all channels, where N is the number of RCEs that are recorded in the run. Microslices are then combined to make millislices, the length of which was configurable. Once produced, these millislices were sent by the DAQ to the event builders, to be stored as time synchronous LArSoft data objects. 21

The time synchronous events produced by the DAQ, did not, however, correspond to the physics events. This is because the DAQ was originally designed to produce a continuous data stream. This meant that the DAQ was configured to pad events with headers when a sub-system provided no physics information, such as nanoslices in the case of the RCEs. Removing these padded header objects was a remit of the online to offline converter discussed in Section 6.2. As the length of the millislices was configurable, it was chosen to be 10 ms (20,000 ticks), in order to best attempt to fully contain physics events, and reduce the need for the online to offline converter to stitch DAQ events together. The padding of millislices with headers between physics events introduced some peculiarities in the recorded data, such as millislices containing two parts of non-continuous data. This is shown in Figure 6.2, where the second millislice has no information for the time between the end of physics event 2, and the start of physics event 3. 35

6.1 Organisation of the data structure

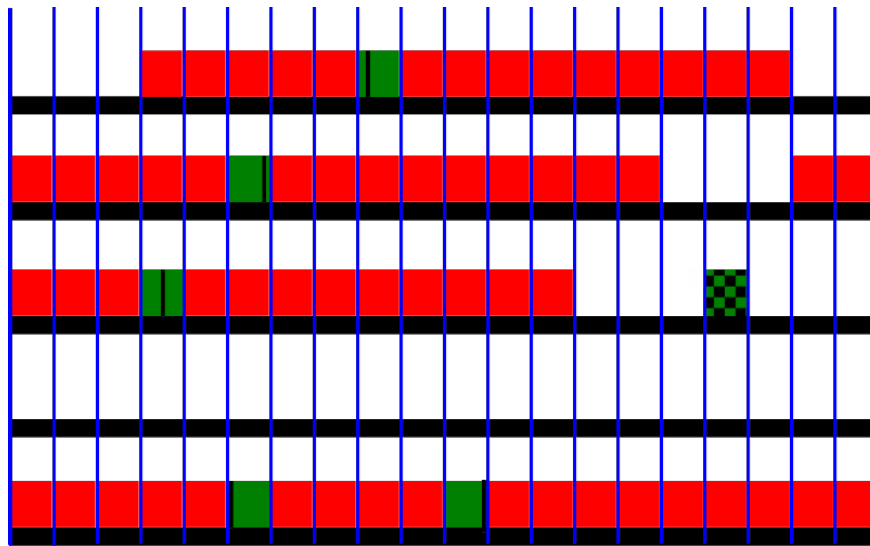


Fig. 6.2 A diagram of possible millislice structures for the TPC data recorded by the 35 ton. Each row represents a millislice, whilst each box represents a microslice. The vertical blue lines delineate each microslice, giving 20 microslices per millislice. Solid red and green boxes represent microslices with TPC data in them. A group of 15 continuous red and green boxes are the recorded “physics events”. Green boxes represent triggers which were used, with the black lines showing the time in the millislice at which the trigger occurred. Green and black patterned boxes represent coincidences of CRCs which were not issued as triggers. A possible reason for these triggers not being issued, is their proximity to a previous coincidence trigger which was issued.

1 During normal data taking, the last N microslices are buffered in the RCEs so that if a
 2 trigger is issued, the previous millislices can be accessed before they are deleted. As the
 3 data is buffered in the form of microslices, previous microslices may only be accessed in
 4 whole. This means that a whole number of microslices must be loaded before the trigger, so
 5 when a trigger is issued part way through a microslice, the previous X microslices are sent
 6 to the event builders. As a result, there are always a minimum number of ticks both before
 7 (5,000 ticks), and after (9,000 ticks), the trigger, but the exact numbers can change by up to
 8 1,000 ticks for a given event, depending on where in the microslice the trigger came. The
 9 result of this is that it is impossible to know the number of ticks before/after a given counter
 10 coincidence. This is shown in Figure 6.2 where the black lines representing triggers, are seen
 11 to occur at different points within the microslices. For example, physics event 1 will have
 12 more data after the trigger than physics event 2 as the trigger occurs earlier in the triggered
 13 microslice.

6.2 Reformatting the data to the offline structure

Conversion of the data objects stored in the raw data to the data objects used in simulation required a suite of unpacking services to be written, the specifics of which are not discussed here. These all required a common interface through which to access the data and check that the timing of each component was consistent, so that a final LArSoft file for downstream use could be produced. This interface had the added role of producing complete physics events, meaning that it had to be able to combine multiple millislices and extract only the data containing the continuous physics events.

Following the unpacking of each of the sub-systems, the data reformatter would loop through the TPC ticks to see if a user defined set of conditions could be satisfied at that time. These conditions were usually whether an East-West or North-South counter coincidence occurred at that time, or if this millislice contained TPC data whilst the previous one did not. The latter was the default configuration as this gave the option of preserving all of the data gathered, for reasons discussed at the end of Section 6.1. Other conditions were available, though rarely used, such as if the SSPs observed a large flash of flight, or if there was a large change in the average TPC ADC value. Once a set of conditions are satisfied a user defined number of pre-condition ticks are gathered. No pre-condition ticks are gathered when the previous millislice contains no TPC data, as there is no previous data to load which would not have a gap in time, see Figure 6.2. In the case of using a counter coincidence to make an event, a value of 300 pre-condition ticks is normally used, with a maximum of 5000 ticks being able to reliably collected. Once the pre-conditions ticks are gathered, a further N post-condition ticks are gathered, where N is defined by the user. Usually 15,000 ticks are gathered when the previous millislice is empty, and 5,200 ticks are gathered when there is a coincidence, though a maximum of 9,000 ticks could be reliably gathered. Data from the other components is added to the event if its timestamp is within the timestamps of the first and last ticks in the event, when no more TPC data is required, or at the end of a millislice if stitching is required. All timestamps are corrected such that the event began at $t=0$ as the reconstruction assumes this, and the timestamp of the start of the event is stored in the event record, so that it can be accessed later if required.

At all points in this process it is important to integrate flexibility so that the user can choose the length of events, which sub-systems are in the events, and what the conditions are for making events. It is also important for users to be able to run the service on already formatted events, as the unpacking services are the major overhead in running the interface. It is also conceivable that users would want to reformat Monte Carlo events so as to centre

6.3 Observations on data quality and noise mitigation

60

1 them around their chosen conditions, and so the use of the unpacking was determined by the
2 interface depending on the format of the input file.

3 **6.3 Observations on data quality and noise mitigation**

4 Reformatting the online data to the offline format was an important step in maintaining
5 data quality, as subsequently there was no access to the raw data due to the framework of
6 the 35 ton software. Some of the important checks which are performed are outlined in
7 Figure 6.3. If any of these issues are present in a given physics event then it is discarded,
8 as the integrity of the data cannot be guaranteed. It was decided that these events would be
9 discarded as non-synchronous events would lead to hits in the detector being at incorrect
10 times, and padding empty events with pedestals could mean that tracks seem to disappear
11 and later reappear as they travel through the detector.

12

13 Another example of inconsistent events is when the sub-systems are not synchronised
14 with each other. This is normally caused by one of the sub-systems missing a clock increment
15 from the master timing unit, due to the data trigger being issued close to an increment from
16 the master unit. This misalignment causes an incorrect time sample being read out, and so
17 the data from each sub-system within a millislice is not consistent. The result of this is that
18 the event will fail the timestamp check, and so won't be added to the event record. To avoid
19 incomplete events these physics events are also discarded when observed.

20

21 The electronic noise in the 35 ton was higher than anticipated, with the RMS of the RCE
22 ADC being approximately 30 counts compared to an expected thermal noise of around 2.5
23 ADC counts. Many sources contributed to this elevated noise, some of which are explained
24 below.

25

26 Though not directly affecting the noise issues “stuck ADC codes” were a feature of the
27 data which had to removed. “Stuck ADC codes” were caused by bit level corruption where
28 lowest 6 bits in the ADC became frozen to either 0x0 or 0x3f. This was observed during the
29 first stages of commissioning and an algorithm to remove them was developed and tested
30 on Monte Carlo [24]. In simulations it was observed that the signal could be recovered with
31 minimal losses, as shown in Figure 6.4, where the blue lines (after removal) are seen to
32 closely match the black lines (before adding stuck codes).

33

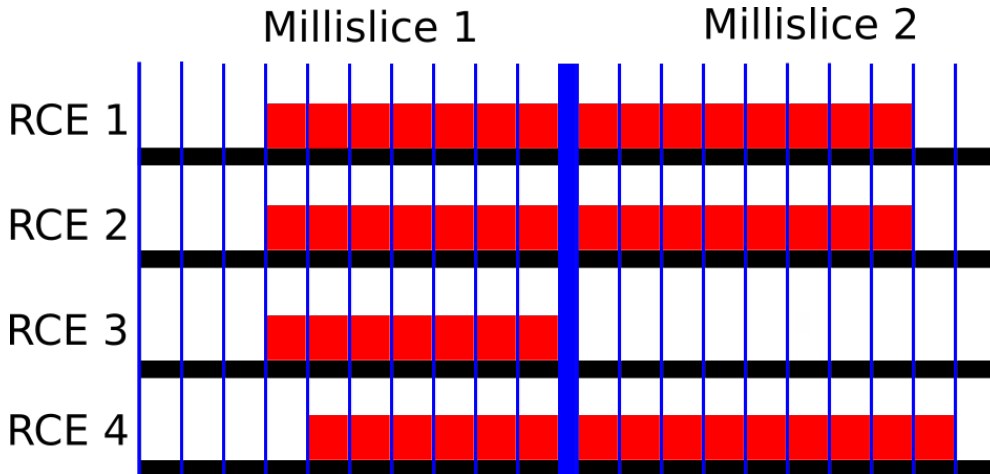


Fig. 6.3 A diagram of TPC microslices within millislices in the 35 ton data stream. Two millislices are shown, each containing 10 microslices. One physics event straddling the millislice boundaries is shown, and 4 RCEs representing each row are read out. The vertical blue lines delineate each microslice (0.5 ms, 1,000 ticks), with the thick blue line showing the millislice boundary. Solid red boxes represent micro slices with TPC data in them. It can be seen that RCEs 1 and 2 contain data for the same interval, whilst the data from RCE 3 in millislice 2 has been “Dropped,” and the data from RCE 4 is shifted by 1 microslice from RCEs 1 and 2 and is thus “Inconsistent.” As a result of these issues this physics event would be discarded as data integrity cannot be guaranteed.

A significant portion of the noise was correlated between groups of 32 channels, where the ADCs would coherently oscillate. To remove these coherent shifts, ADC baselines were calculated for these groups of 32 channels at each tick, and then subtracted from the measured ADC values. This was found to be an effective method of removing coherent noise in MicroBooNE [25]. The effect of removing coherent noise is shown in Figure 6.5, where the signal peak becomes much easier to discern after noise removal, and a coherent noise peak around tick 6030 is removed. An issue with removing coherent noise in this way is that events which are parallel to the APAs will produce signals at common times across adjacent wires, and these signals may be removed along with the coherent noise. This will cause a reduction in the hit reconstruction efficiency. The only way to prevent this is to “protect” potential signal regions from the coherent noise removal, as is done in MicroBooNE [25].

When a Fast Fourier Transform (FFT) [26] is performed on the coherent noise subtracted waveforms, it can be seen that signals occur with specific frequencies. Some of these frequencies are caused by real energy depositions, whilst others are due to the electronics noise. It is possible to remove the noise frequencies by applying Wiener filters [27]. Frequency spectra are taken for each of the three planes, and a clear signal is both preserved and

6.3 Observations on data quality and noise mitigation

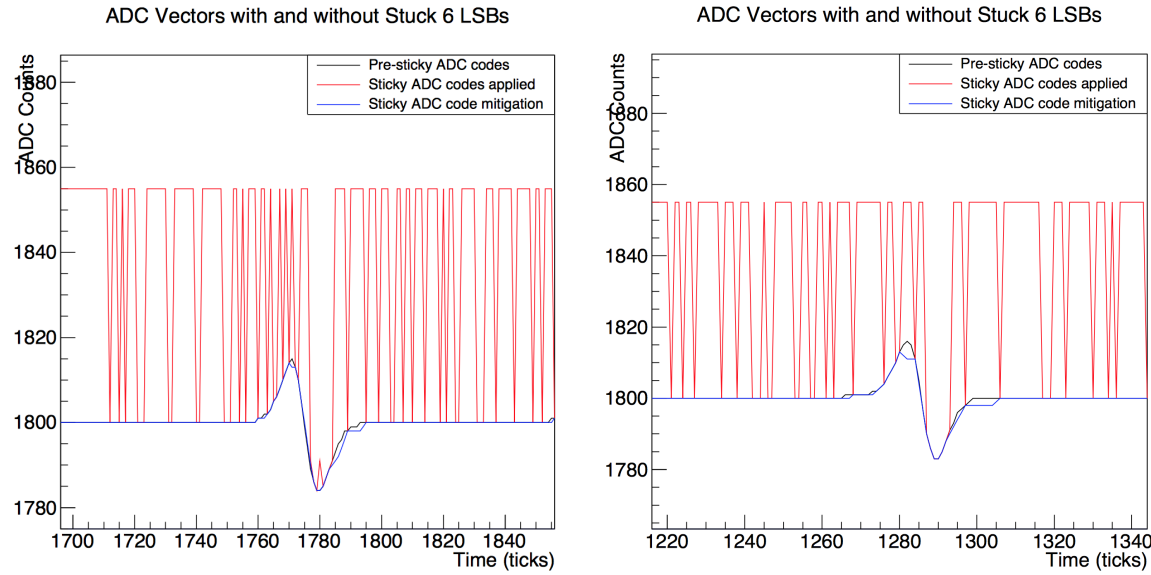


Fig. 6.4 Two Monte Carlo spectra showing the effect of the introduction and removal of stuck bits on a simulated signal. The black line shows the simulated signal on a wire, which is then modified by adding the effects of “stuck ADC codes,” shown by the red line. The “stuck ADC codes” are then removed, and the resulting signal is given by the blue line. It can be seen that the signal loss is minimal after the “stuck ADC codes” are removed. The figures were taken from [24].

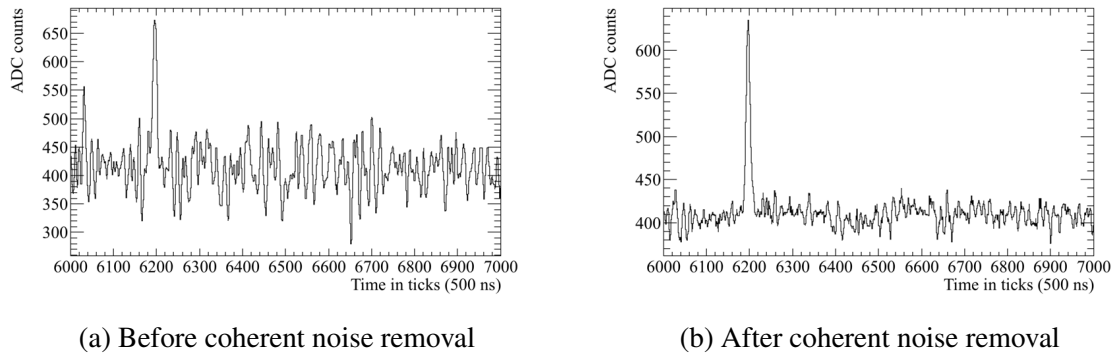


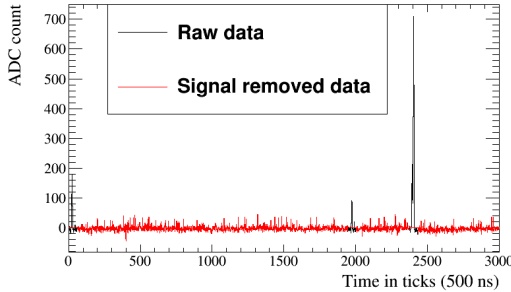
Fig. 6.5 The effect of coherent noise removal on a 35 ton signal event. Left shows the signal before coherent noise is removed, and right shows the signal after the coherent is removed. The signal peak around tick 6200 is much clearer after coherent noise removal, meaning that hit reconstruction becomes much simpler.

¹ suppressed. The raw signal spectra, are then divided by the signal suppressed spectra, to produce *signal/noise* frequency spaces. The regions of frequency space to be conserved, given by regions of high *signal/noise*, can then be found by fitting a combination of sigmoid functions to the frequency spaces. A demonstration of how this was applied is shown in Figure 6.6. It is also possible to remove specific frequencies which are not removed by

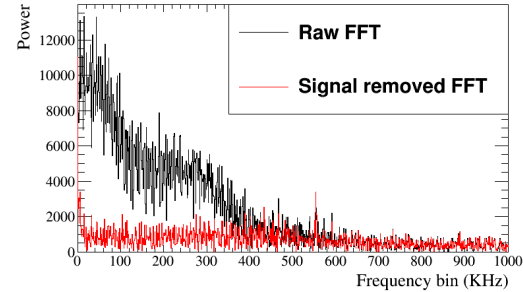
6.3 Observations on data quality and noise mitigation

63

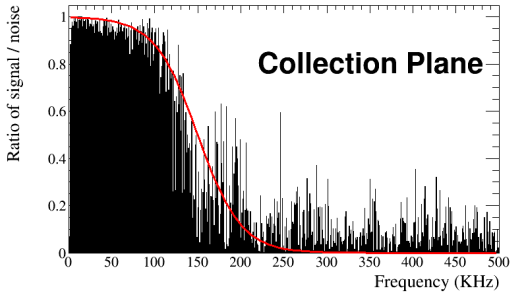
the filters, this was necessary for a 54 KHz noise component, which was introduced by the fluorescent lights in the detector hall. After the run ended it was found that some of the high frequency noise components were introduced by a short on a warm power cable. The techniques used to find this cable will be used when commissioning future detectors [28].



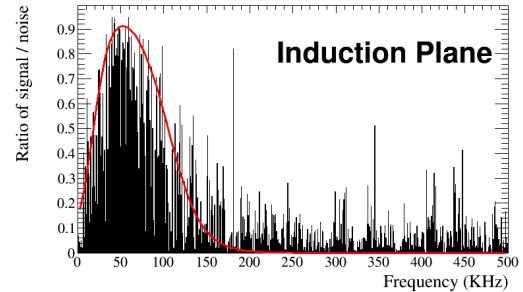
(a) A raw and signal subtracted waveform for a collection plane wire.



(b) The FFT of the raw and signal subtracted waveform for a collection plane wire.



(c) The *signal/noise* ratio for a collection plane wire, the red line shows the fraction of frequency power which passes the filter.



(d) The *signal/noise* ratio for an induction plane wire, the red line shows the fraction of frequency power which passes the filter.

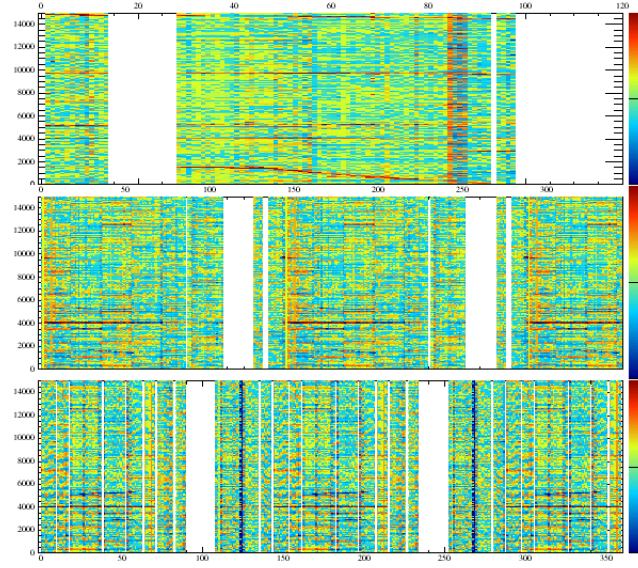
Fig. 6.6 The application of Wiener filters to the 35 ton data. Top left shows a waveform from a collection plane wire which is then signal suppressed. The FFT of both the raw and signal suppressed waveforms are shown top right. The *signal/noise* ratio for this waveform is shown bottom left, where a sigmoid function has been overlaid to preserve only the areas of high *signal/noise*. The *signal/noise* frequency space ratio, and an overlaid sigmoid function, for an induction wire, is shown bottom right.

An example of the effect of the noise mitigation steps is shown in Figure 6.7. The left side shows the raw data and the right side shows the data after the stuck code unsticker, coherent noise removal and Wiener filter algorithms have been applied. The effect of noise removal is clear, as the signals from the tracks become much more pronounced, particularly on the bottom induction plane. However, it can also be seen that the noise removal algorithms also remove signals from tracks, as the depositions shown on the collection plane (top plot)

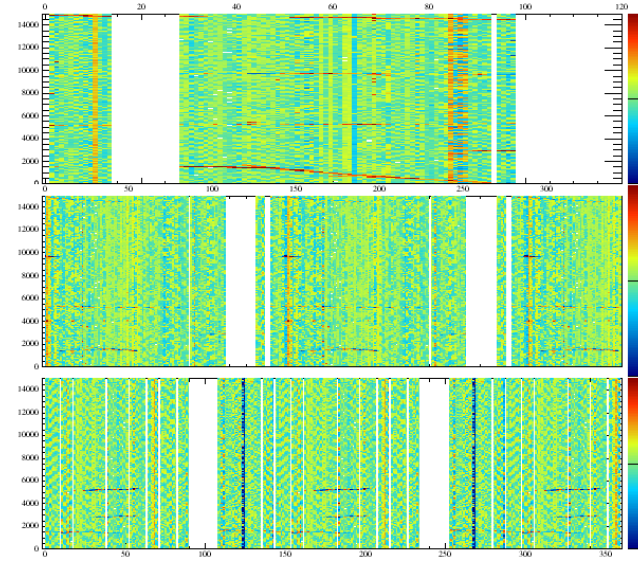
6.3 Observations on data quality and noise mitigation

1 around tick 10,000 becomes much less pronounced.

2



(a) Raw signal before noise removal



(b) Signal after noise removal

Fig. 6.7 Event displays showing the effect of the noise removal algorithms on data in the 35 ton. The event displays show the signals in the collection, U and V planes respectively. The plots show wire number, time in ticks and charge in ADC counts on the x, y and z axes respectively. The effect of the noise removal algorithms can clearly be seen, as large changes in charge due to the noise, are no longer present after they have been applied. The application of the noise removal algorithms does however also remove real signals, as depositions across many channels at the same time which were present before their application, can no longer be seen after they are applied.

Transitions to a higher noise state associated with strong signals at high frequencies, between 400 and 650 KHz, were observed after cool down. The transitions would occur approximately every 2 hours, and were occasionally observed to happen shortly after a saturation event across the whole detector [28]. Once the state was induced the only way to stop it was to power cycle the low voltage supplies. It was found that power cycling APA3 could both stop, and induce the higher noise state. Importantly, this was the only APA with electronics located at the base of the TPC. The data taken during the elevated noise state was unrecoverable as the electronics noise was too large, and so upon the observation of a transition the low voltage supplies were power cycled. It was observed that the transitions occurred much less frequently when APA3 was not powered, and so it was not used for significant portions of the data taking period. Despite efforts to study the transitions during warm testing they were unable to be induced, and have not been observed in other experiments such as MicroBooNE, despite other experiments using the same low voltage supplies. It is thought that the cause of the transitions is a feedback loop in the low voltage cable, which was much longer in the 35 ton than in MicroBooNE. This would explain why APA3 was more susceptible to the feedback loop, as the cable is routed past its electronics [29].

6.4 Performance of reconstruction algorithms

Following the noise removal outlined above, hit and track finding was still more difficult than in simulations, due to the still elevated noise level. In order for a reasonable number of hits to be reconstructed the hit finding threshold had to be substantially increased in data, as compared to Monte Carlo. This meant that many of the low energy hits would not be reconstructed.

A potential solution to not reconstructing the low energy hits, is to use the counter positions to select only hits which could have caused coincidences. When determining whether a reconstructed hit could have caused the counter coincidence, a two-dimensional window around the counter edges in the yz plane is constructed, and timing information is used to extend this to three dimensions. The x position of the hit can be calculated using the hit time, and electron drift velocity using Equation 5.1.

Determining whether collection plane hits are within the counter window is trivial as they have a constant z position, and either cover the full detector height (tall APAs), or roughly half of the detector height (short APAs). The wrapping of the induction planes, however, means that each wire segment has to be considered individually, and that multiple segments of a

6.4 Performance of reconstruction algorithms

66

given wire could lie within the counter shadow. The 3-dimensional volume that is enclosed by connecting the edges of the counters which were hit in the counter coincidence, is called the “counter shadow.” Only those wires which lie within the 2-dimensional projection of this volume onto the yz plane, are considered here. Choosing between these potential wire segments is done by iterating through the following steps. If at any point only one segment satisfies the condition then that segment is chosen:

- Does the wire segment intersect any collection plane wires which record hits?
 - This is because when there is a signal on an induction plane there should also be signals on the collection wires.
- Are there adjacent wires which have hits at a similar time?
 - This is because one would expect a track to deposit energy on multiple adjacent wire segments.
- Which hit lies closest to the line defined by unique collection plane hits in the xz plane?
 - This follows identical logic to the first criterion, but selects the hit which best matches the collection plane hits, and attempts to remove the effect of noisy collection plane wires by only using wires which have one hit within the counter shadow. This would also hopefully improve the quality of the fit, as there will not be numerous outlying hits.
 - This can be changed to consider the line defined by previously selected hits in the given TPC and plane where the hit choices are.

Following a re-optimisation of the clustering algorithms, it was observed that the standard reconstruction could achieve track reconstruction to a similar efficiency as the counter shadowing, and so the standard reconstruction has been used in the discussions to follow [30]. There has since been an effort to improve the counter shadowing hit disambiguation to remove the outlying collection plane hits using the MLESAC method [31], whereby points which are far away from a best fit are ignored. These studies are still on-going [32].

A symptom of the elevated noise state is that signals are often dropped on one of the induction planes, this means that the tracking algorithms often have to combine clusters in only two of the three planes. Reconstruction using two planes was shown to be effective by the ArgoNeuT collaboration [33], so the loss of signal in one of the three planes is not prohibitive to track reconstruction. Another consequence of the elevated noise level is that even when the

6.4 Performance of reconstruction algorithms

counters are used to seed hit finding, the hit finding threshold is too high to reconstruct the very lowest hits. This causes the plot of dQ/dx for muons, shown in Figure 6.8, to look flat, due to a cutoff at 100 ADC cm^{-1} , below which no hits are reconstructed. The inability to reconstruct the lowest energy hits means that calorimetry is all but impossible on the 35 ton dataset, even though the tracking algorithms perform relatively well. The inability to perform reliable calorimetry en masse means that the only particles which can be assuredly identified are the muons which triggered the counter coincidences, making the analysis proposed in Section 5.4 extremely difficult, if not impossible.

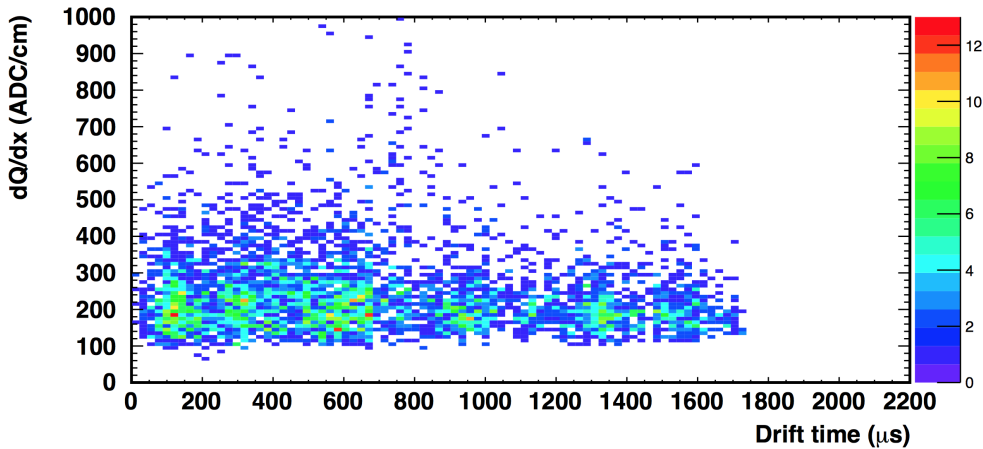


Fig. 6.8 The dQ/dx values for a sample of muon collection plane hits, note the cutoff at 100 ADC cm^{-1} due to the hit finding threshold. Figure taken from [34].

The muons in the triggered sample will all traverse the detector, but their orientations can be carefully selected by the user. For example, one could easily select a sample of muons which cross the APAs at increasing angles, or are parallel to the wire planes at increasing drift distances. This is done by matching through-going muons with counter coincidences. The process by which this is done is identical for both North-South and East-West coincidences, though more focus will be given to the later, as it is with muons of this orientation that the study shown in Section 6.5 was performed. The same matching technique would also have been applied to vertical muons had the telescope trigger been utilised. For a reference as to the locations of the counters around the cryostat, see Figure 3.3, and for a representation of only the East-West counters, see Figure 6.9.

It is possible to construct a line in the yz plane joining the centres of the two counters which were hit when a coincidence occurred, shown by the dashed line in Figure 6.9. This can then be compared with the trajectory of a track in the yz plane and a dot product of the

6.4 Performance of reconstruction algorithms

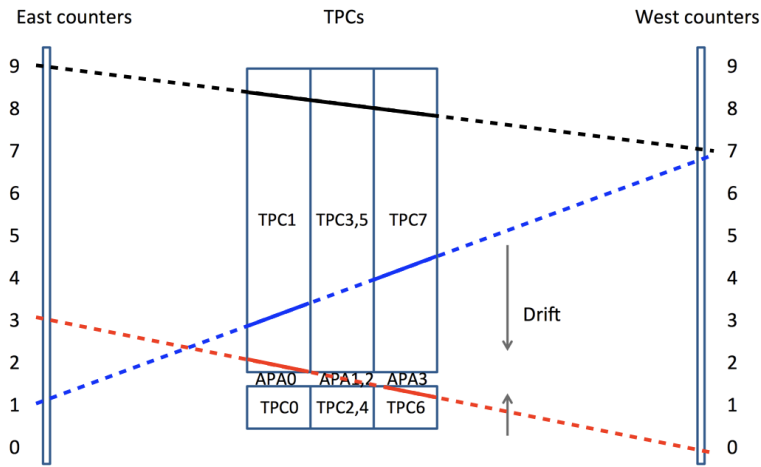


Fig. 6.9 The numbering scheme for the East - West counters in the 35 ton. The counters have been numbered from 0 to 10 depending on their position from the end of the short drift volume. This is different to the LArSoft numbering scheme shown in Figure 3.3 where they go from 6-15 and 28-37 for the East and West counters respectively. Three hypothetical muons which would have caused coincidence triggers are shown as dashed lines, and the hypothetical reconstructed tracks they produce are shown as solid lines. The red track is an APA crossing event, and would produce tracks in TPCs 1 and 6. The black muon is fully reconstructed as one continuous track, however the blue particle is not reconstructed in the middle TPCs and so is reconstructed as two separate tracks.

1 two vectors calculated. A reconstructed track is assigned to a given counter coincidence if the
 2 dot product of the track and the coincidence is more than 0.98, and the hit times are consistent
 3 with the x positions of the counters. The results of the dot product calculation are shown
 4 in Figure 6.10. Matching only tracks which are well aligned with a counter coincidence
 5 should produce a pure sample of tracks, as parallel muons are unlikely to be highly correlated
 6 in time, and any tracks reconstructed from the noise will have random directions. This is
 7 shown in data where if multiple tracks pass the dot product cut they are co-linear and are not
 8 randomly orientated, as shown in Figure 6.11.
 9

10 By matching tracks in this way it is possible to evaluate the reconstruction efficiencies
 11 for these muons, at increasing drift distances and track angles. If multiple tracks are aligned
 12 with the coincidence, and are within the expected time region, then their track lengths are
 13 summed when calculating reconstruction efficiencies. This is because, it is expected that
 14 the track was split by a region of the detector either being turned off, or being too noisy
 15 to reconstruct a track. If these tracks have a combined track length of more than 50 cm,

6.4 Performance of reconstruction algorithms

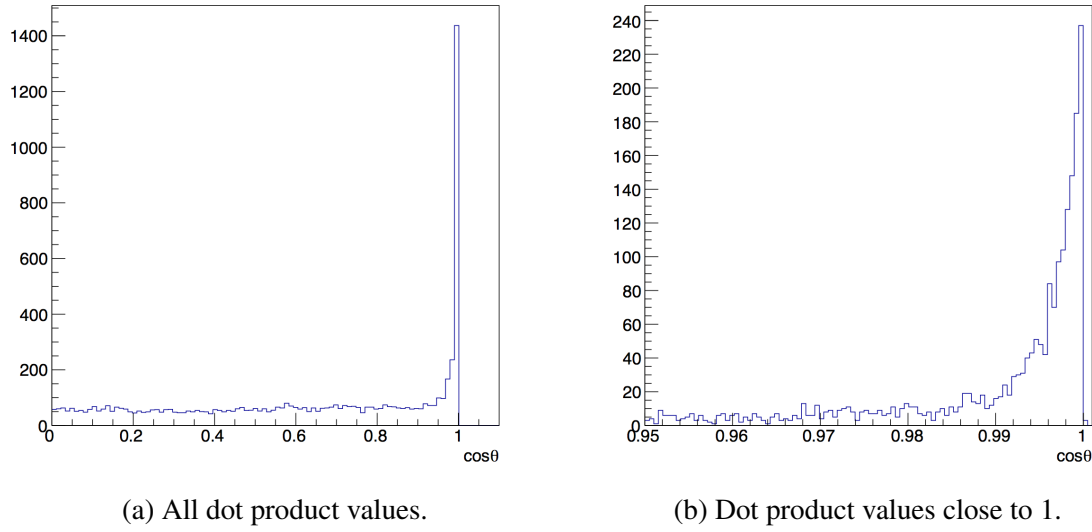


Fig. 6.10 The dot product of the track and vector joining the centres of the coincidence counters in the yz plane. A threshold value of 0.98 is required for a track to be considered to be due to the counter coincidence. It can be seen that many tracks are well aligned with counter coincidences, having dot products of more than 0.99.

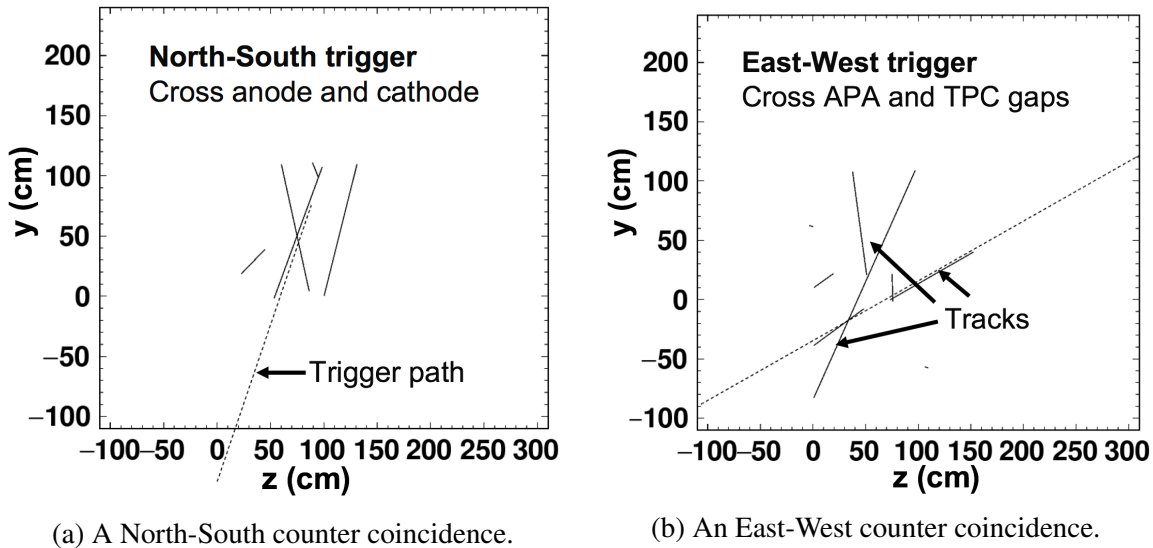


Fig. 6.11 The alignment of reconstructed tracks with the vectors joining the centres of the coincidence counters. The dashed lines show the vectors joining the centres of counters hit in the coincidence, whilst the solid lines show the reconstructed tracks. Left shows the alignment of tracks with a North-South coincidence, whilst right shows the alignment of tracks with an East-West coincidence. The z positions of the tracks are shown on the x axis, and the y positions of the tracks are shown on the y axis. Figures taken from [30].

6.4 Performance of reconstruction algorithms

70

1 then the coincidence is identified as having been successfully reconstructed. This threshold
2 is much lower than the true track length which should be reconstructed (more than 150
3 cm), but few particles are fully reconstructed in the data, and so a compromise is made to
4 achieve a large enough sample of tracks upon which analyses can be performed. A recon-
5 structed track that is 50 cm long is likely to have a large number of hits on collection plane
6 wires that are not noisy, and it is these hits which are required when calculating purity or
7 measuring the effect of diffusion, as discussed in Section 6.5. A track with length more
8 than 50 cm is also likely to have been stitched between TPCs, due to the geometry of the
9 35 ton and track trajectories. The demonstration of stitching tracks between TPCs was a
10 design goal of the 35 ton, and so identifying tracks where this was achieved satisfies that goal.

11

12 An important concept that must be introduced before these reconstruction efficiencies can
13 be described is that of a “counter difference.” The “counter difference” of a coincidence and
14 its associated tracks, is defined as the absolute difference between the counter numbers of the
15 East and West counters that were hit. As such, the “counter differences” of the coincidences
16 shown in Figure 6.10, are 2, 3 and 6 for the black, red and blue coincidences respectively.
17 Given the orientation of the counters, the rarest counter difference will be 9, as only particles
18 which hit counters (E_0 and W_9) and (E_9 and W_0) will have a counter difference of 9. In
19 contrast to this, the most common value for the counter difference is 1, as there are many
20 possible combinations of East and West counters being hit to give this counter difference.
21 In the discussions below “counter difference” is occasionally referred to as “delta counter”
22 or “ Δ counter.” The approximate angles which tracks, with given counter differences, have
23 relative to the APA frames, is shown in Table 6.1.

24

25 Figure 6.12 shows a range of reconstruction efficiency plots for combinations of different
26 counter differences, and different drift distances. As the counter coincidences with large
27 counter differences will have large variations in drift positions, the drift distance plotted here
28 is the average x position of the counter centres that were hit. For example, if the two counters
29 that produced the coincidence are at $x = 10$ cm and $x = 230$ cm respectively, then the drift
30 distance plotted would be 120s cm. This distance is called the “coincidence centre” in the
31 following discussion. Only coincidences which would produce tracks that are contained
32 within the long drift volume are considered here, hence there being no negative x positions.

33

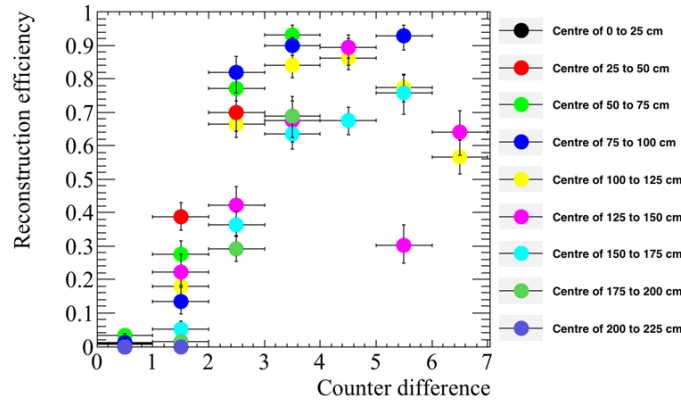
34 From Figure 6.12a, it is evident that the reconstruction efficiency for tracks with shallow
35 angles relative to the APAs is extremely poor, with the efficiency for tracks aligned with
36 counter differences of 0 or 1 never rising above 10%. This is due to the coherent noise

Table 6.1 The angles which tracks, with given counter differences have, relative to the APA frames. Though the East and West counters have a width in the y (vertical) direction, this is much less than their extent in the z direction. The depth of the counters, their extent in x , is negligible compared to the separation of the East-West counters. The counters have identical widths in both the y and z directions. The angles are calculated using the difference in the centres of the counters in the z direction divided by the separation of the East and West counters in z .

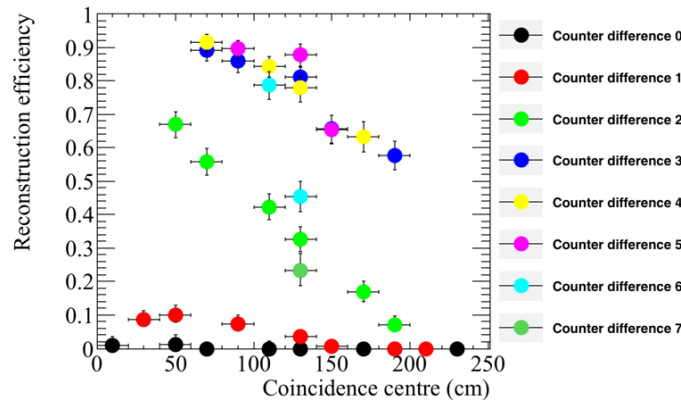
Absolute counter difference	Approximate angle ($^{\circ}$)
0	0 ± 2.1
1	4.2 ± 2.1
2	8.4 ± 2.0
3	12.5 ± 2.0
4	16.5 ± 2.0
5	20.3 ± 1.9
6	23.9 ± 1.8
7	27.3 ± 1.7
8	30.7 ± 1.6
9	33.5 ± 1.5

removal, where hits which are correlated in time will be removed as they will be perceived as being noise, as opposed to real signals. As the difference in counter number increases, the efficiency is seen to increase, though the rate of this increase is seen to depend on the “coincidence centre”. The effect of increasing “coincidence centre” can be seen more clearly in Figure 6.12b, where the efficiency for each counter difference as a function of “coincidence centre” is plotted. Here, it can be seen that the reconstruction efficiency decreases for coincidences that are centred further away from the APAs. This is due to the fact that when an energy deposition has further to drift, it will induce a smaller pulse on the wires, meaning that it is more likely to be below the hit threshold. Figure 6.12c combines Figures 6.12a and 6.12b, to show how the reconstruction efficiency for increasing “coincidence centre” changes, with increasing counter difference. It can be seen that tracks with counter differences of between 3 and 5, where the “coincidence centre” is between 60 cm and 140 cm away from the APAs, are the best reconstructed coincidences. Finally, Figure 6.12d shows how the frequency of coincidences of a given counter difference occurs, compared to how many events contain reconstructed tracks which are aligned with the coincidence. It can be seen that, as stated earlier, the most common counter difference is 1, with the least common being a counter difference of 9. However, given the low reconstruction efficiency seen for the lowest counter differences, few tracks are reconstructed. This means

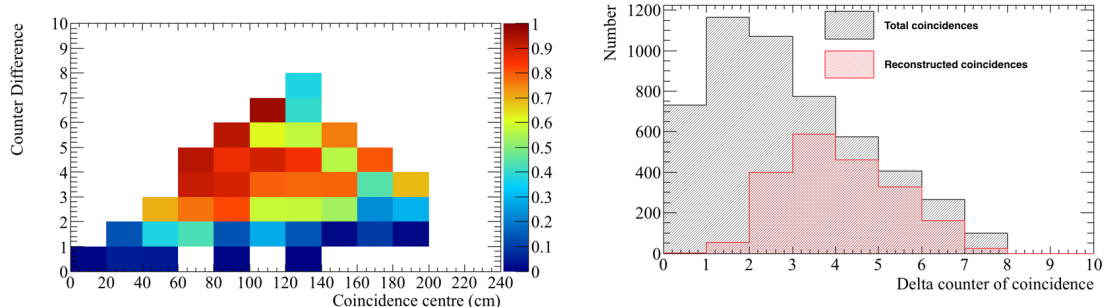
6.4 Performance of reconstruction algorithms



(a) The reconstruction efficiency as a function of counter difference for different coincidence centres.



(b) The reconstruction efficiency as a function of coincidence centres for different counter differences.



(c) How the reconstruction efficiency changes for increasing coincidence centres and counter differences.

(d) The number of events for each counter difference that were recorded in the data and the number of those which were successfully reconstructed.

Fig. 6.12 The reconstruction efficiencies for coincidences that trigger an East-West coincidence in the 35 ton data over a 2 day running period.

that when considering the reconstructed tracks, most are due to coincidences with counter differences of either 3, 4 or 5.

6.5 Measuring interaction times using electron diffusion

As electrons drift from the interaction point to the wire planes they become spread out in both time and space, this effect is known as diffusion, and is an important property of electron transport in LAr, which must be well understood. The mechanism by which diffusion occurs in LAr was first discussed by Atrazhev-Timoshkin [35], and has since been developed to consist of a complete set of measurements for electric fields between 100 and 2000 V cm⁻¹ [36]. The diffusion of electrons is rarely isotropic, and so the component that is transverse to the drift field, and the component that is parallel to the drift field, are normally measured separately. Diffusion parallel to the drift field is called longitudinal diffusion, and is generally smaller than the component of diffusion that is transverse to the drift field. Figure 6.13 shows how diffusion can smear the electrons collected on a set of wires when the electrons are initially highly correlated in time and space.

Longitudinal diffusion has the effect of spreading the drifting electrons out in time, causing signals to become wider in time, and smaller in height, as the total charge is conserved. The increasing hit width can be measured for increasing drift times (distances), provided the hits do not fall below a hit finding threshold. Transverse diffusion causes drifting electrons to spread out in space, changing the amount of charge deposited on a wire, and reducing the charge resolution of the detector. Transverse diffusion is measured by discerning how the width of the hit charge distribution changes for increasing drift distances [36].

Through-going particles make ideal tracks to study diffusion as they are minimally ionising, and so have roughly constant energy depositions along their tracks. The tracks that they produce can also cover a wide range of drift distances, if they are not parallel to the APAs. The drift distances of hits within a track can be determined by matching the track with a counter coincidence as discussed at the end of Section 6.4. The x positions of the hits can then be corrected using the result of Equation 5.2, in Equation 5.1.

Traditionally the only way to determine an interaction time for a track is to either match it to an external calibration source, such as whether it aligns with an external counter coincidence, or to match it to a flash of scintillation light, as in Section 5.1. These techniques are particularly crucial for neutrino detectors on the Earths surface, such as MicroBooNE, where

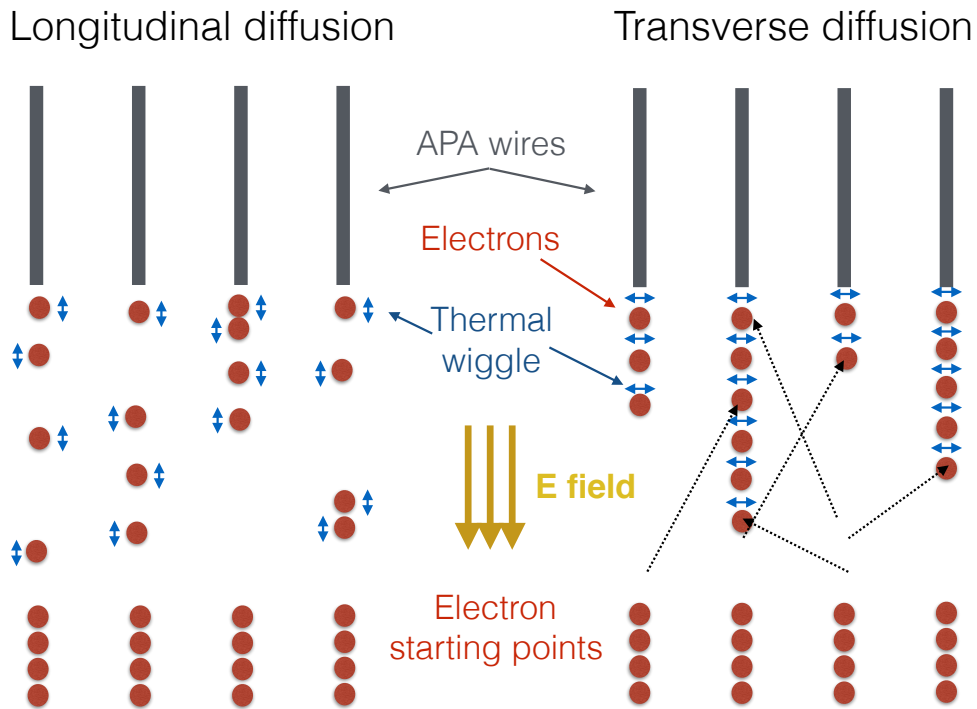


Fig. 6.13 A schematic showing the longitudinal diffusion (left), and the transverse diffusion (right), of electrons. In both cases, four electrons are initially shown below four wires, and are allowed to diffuse in either the drift direction, or perpendicular to the drift direction, in the longitudinal and transverse cases respectively. It can be seen that the effect of diffusion is to make the electrons spread out in time, in the case of longitudinal diffusion, and to spread out in space, in the case of transverse diffusion. Figure taken from [37].

1 each neutrino interaction usually has a background of at least one cosmic muon. The recon-
 2 structed tracks from this muon background have to be distinguished, from those due to the
 3 neutrino interactions, in order correctly assign a scintillation flash to the reconstructed tracks.
 4 An event where scintillation flashes and cosmic muons need to be correctly distinguished
 5 is shown in Figure 6.14. However, it may be possible that the change in hit width due to
 6 diffusion, as a particle travels through the detector, could be used to determine the interaction
 7 time; though this has not been attempted before. To study whether this is possible, the effects
 8 of diffusion would have to be measured for a sample of tracks with known interaction times
 9 and orientations.

10
 11 The 35 ton dataset is ideal for testing this hypothesis, as the counters are able to provide
 12 a sample of tracks with known angles and interaction times, which can be used to tune
 13 interaction time determination metrics. These metrics can then be applied to another sample
 14 of tracks, where the interaction time is known but not used, so that the accuracy of the

6.5 Measuring interaction times using electron diffusion

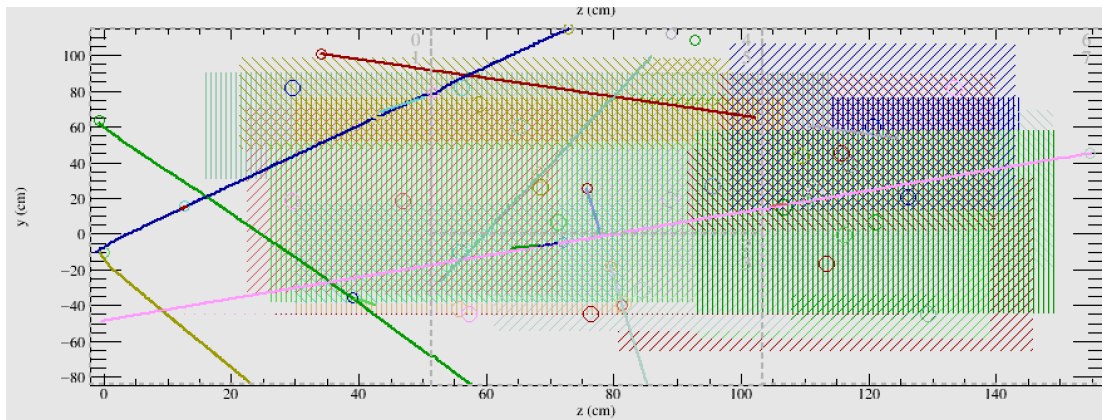


Fig. 6.14 A simulated event display showing multiple tracks and flashes to be assigned to each other in the 35 ton, in the yz plane. The coloured lines represent reconstructed tracks, whilst the coloured dashed boxes represent flashes.

calculated interaction times can be found. As longitudinal diffusion is the dominant effect that increases the hit width, transverse diffusion will not be directly considered further. However, as noted in Section 6.4, the noise level in the 35 ton data causes reconstruction issues, and so it is also useful to compare the method against a low noise detector. Monte Carlo can provide this sample, and this comparison is shown in Section 6.5.2. It is also useful to observe the effects that different detector conditions such as, the electric field, the electron lifetime, the noise level and the rate of diffusion, have on the method. This is shown in Section 6.5.3. First though, the method is performed on the 35 ton dataset.

6.5.1 Determining interaction times in 35 ton data

When calculating the determination metrics, only hits on wires which are not noisy want to be considered. This is because wires with a high level of correlated noise observe hits with a wider RMS. This is shown in Figure 6.15, where, when a baseline noise of 10 ADC counts is added to a simulated hit, with a peak value of 50 ADC counts, and an RMS of 10 ticks, the width increases by over 10%. Hits with delta rays also need to be removed, as the deposited energy will be larger and over a longer period of time than hits from the main track. This will make the RMS of the individual hit wider, and also increase the width of the charge distribution for the track. To remove these hits only hits which satisfy the following cuts are used:

- No hit on the same wire within 50 ticks of the hit in question. This removes delta rays.
- No more than 10 hits on the same wire in the whole 15,000 tick data sample. This removes clearly noisy wires.

6.5 Measuring interaction times using electron diffusion

¹ These cuts will clearly become much more restrictive as the noise level in the detector
² increases, but they are essential in order to produce a dataset which is not overpowered by
³ noise. Only collection plane hits are used, as the charge resolution is better, and the signals
⁴ are unipolar as opposed to bipolar, meaning that a Gaussian function can be easily fitted to
⁵ the signals. Additionally the *signal/noise* ratio on the collection planes was much higher
⁶ than on the induction planes for the 35 ton dataset, and so the hits could be much more
⁷ reliably reconstructed.

8

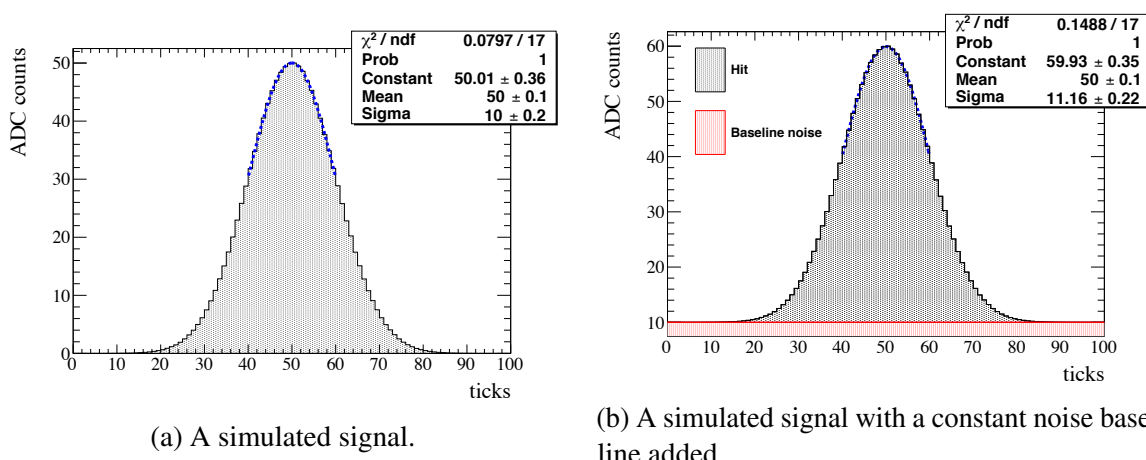


Fig. 6.15 ADC counts as a function of time for simulated signal with a width of 10 ticks, and an amplitude of 50 ADC counts, both before and after, a constant noise baseline of 10 ADC counts is added. The simulated ADC value is shown on the y axis, and the time, in ticks, is shown on the x axis. In reality the noise would fluctuate with time. When a Gaussian function is fitted to each signal, it is seen to be more than 10% larger for the signal where the noise baseline is added. This shows that noise can cause the measured width of a hit to increase. Figure taken from [37].

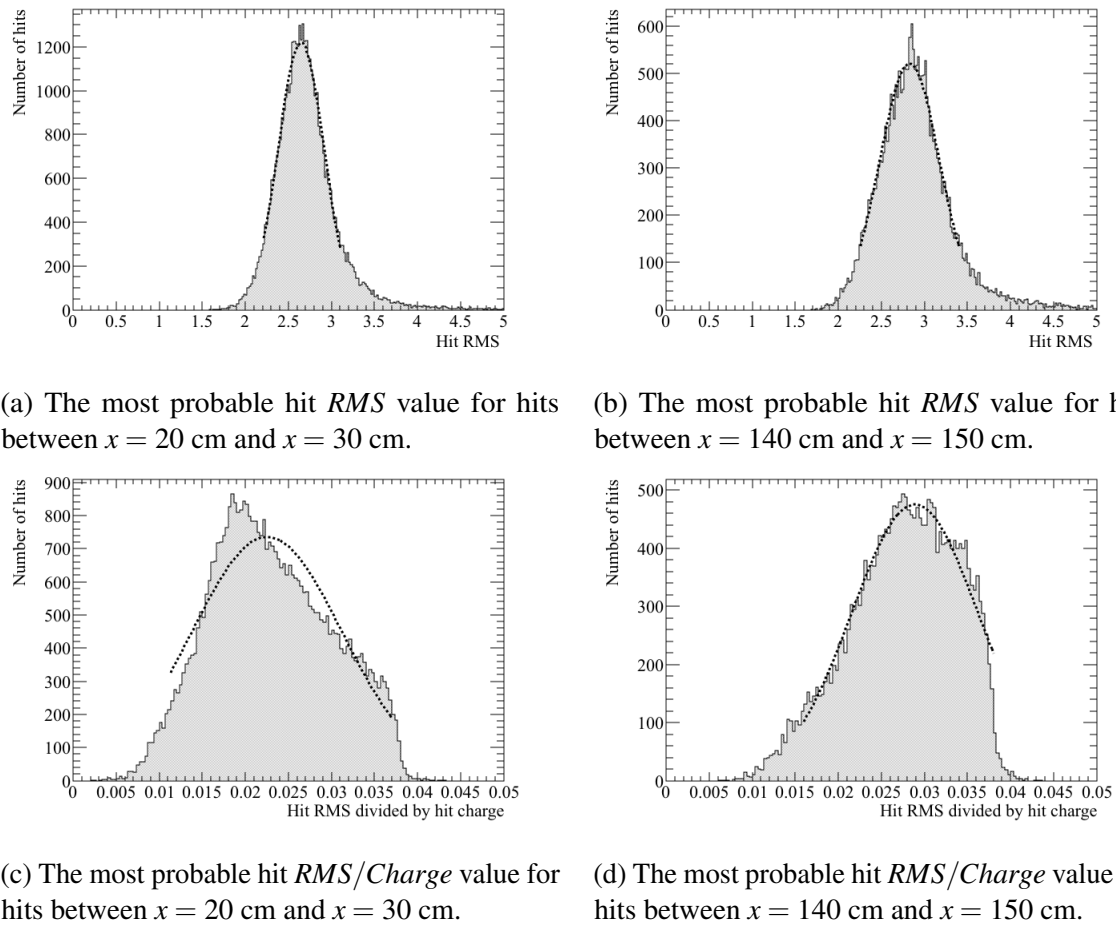
⁹ Diffusion is a track angle dependent property, and so track angle ranges have to be
¹⁰ considered independently. To minimise the number of figures presented, when graphs are
¹¹ made for all counter differences separately, only graphs made for tracks which have a counter
¹² difference of 4 are shown. However, the procedure for predicting interaction times is identical
¹³ for tracks of all counter differences. Tracks with a counter difference of 4 were chosen as they
¹⁴ were one of the angles for which tracks were well reconstructed in the data, see Figure 6.12.
¹⁵ Tracks are considered en masse, and so the hits for every track are separated into 10 cm
¹⁶ regions of increasing drift distance from the APAs. The following quantities are calculated
¹⁷ for each 10 cm drift region:

- ¹⁸ • The hit *RMS* - the most direct way to measure transverse diffusion.

6.5 Measuring interaction times using electron diffusion

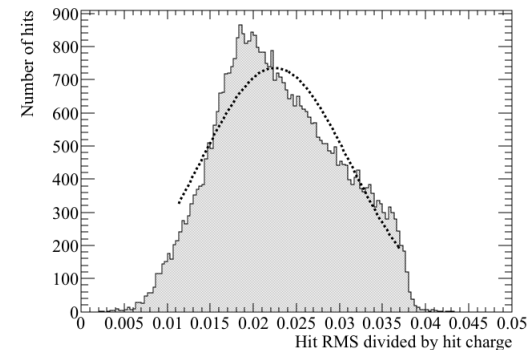
- The hit $RMS/Charge$ - an attempt to incorporate the effect of impurities in the LAr for relatively low purity data which will have a drift distance dependence.
 - The charge of a hit is calculated by integrating the ADCs of the reconstructed hit over time.

Fitting Gaussian functions around the peaks of the distributions will yield the most probable values for the drift regions, as is shown in Figure 6.16.



(a) The most probable hit RMS value for hits between $x = 20$ cm and $x = 30$ cm.

(b) The most probable hit RMS value for hits between $x = 140$ cm and $x = 150$ cm.



(c) The most probable hit $RMS/Charge$ value for hits between $x = 20$ cm and $x = 30$ cm.

(d) The most probable hit $RMS/Charge$ value for hits between $x = 140$ cm and $x = 150$ cm.

Fig. 6.16 The distributions of hit RMS (top), and hit $RMS/Charge$ (bottom), for points between 20 and 30 cm from the APAs (left), and points between 140 and 150 cm from the APAs (right), for tracks associated with coincidences that have a counter differences of 4. The most probable values hit RMS and hit $RMS/Charge$ are determined by fitting Gaussian functions around the peaks of the distributions. These fits are shown as dashed lines.

From Figure 6.16 it is clear the the width of the hit RMS distribution increases for hits which are further from the APAs. However, the width of the hit $RMS/Charge$ is seen to

6.5 Measuring interaction times using electron diffusion

¹ decrease, though this is due to a sharp cut-off at a hit $RMS/Charge$ equal to roughly 0.038
² ticks ADC⁻¹. The reason for this cut off was shown in Figure 6.8. It can also be seen that the
³ most probable values of both the hit RMS and hit $RMS/Charge$ increases with drift distance.

4

⁵ This drift distance effect can be observed by plotting the most probable values of hit
⁶ RMS and hit $RMS/Charge$, as drift distance increases, for fixed counter differences. This
⁷ drift distance dependence on hit RMS is shown in Figure 6.17, for tracks that are associated
⁸ with a coincidence which had a counter difference of 4. A drift distance dependence can
⁹ clearly be seen in the data, as the most probable hit RMS is seen to increase for hits which
¹⁰ originate further from the APAs.

11

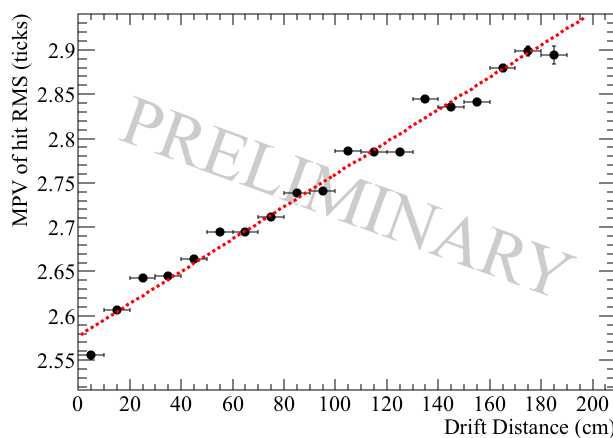


Fig. 6.17 The most probable values of hit RMS as a function of drift distance, for the hits within a track, associated with a coincidence that had a counter difference of 4.

¹² The angular dependence can then be shown by observing how the most probable fit
¹³ values at a drift distance of 0 cm changes for increasing angles, this is shown in Figure 6.18.
¹⁴ It is clear that there is an angular dependence on the hit width, as the most probable hit
¹⁵ widths next to the APAs is seen to rise for tracks associated with coincidences with large
¹⁶ counter differences. This angular dependence, along with the drift distance dependence show
¹⁷ that when considering a large sample, diffusion can be separated into distance and angular
¹⁸ dependencies. However, whether this can be observed for individual tracks, has not yet been
¹⁹ considered.

20

²¹ To consider single tracks, the best line fits for the counter differences for a large sample
²² of tracks, such as in Figure 6.17, are required. These best line fits can then be used to predict
²³ the position you would expect a hit to originate from, given values for the hit RMS and

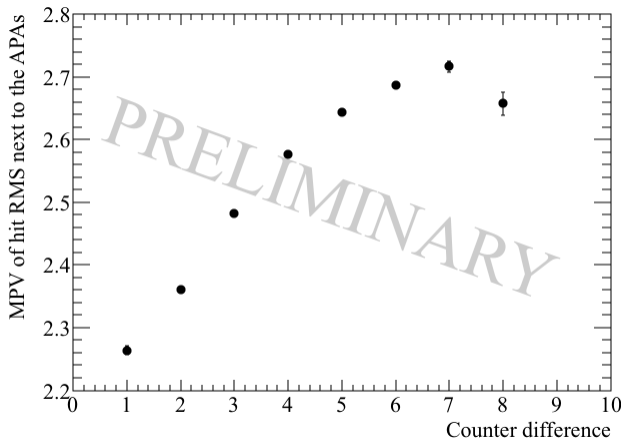


Fig. 6.18 The most probable values of hit *RMS* within 10 cm of the APAs, as a function of the counter difference of the coincidence, that the track, to which the hits belong, was associated with.

hit *RMS/Charge*, and the angle of the track to which it belongs. The predicted positions can then be compared to the known position from the counter coincidence to determine the accuracy of the prediction.

The distributions shown in Figure 6.16 are asymmetric due to some hits having large values of hit *RMS* or hit *Charge*. Asymmetry is also introduced due to the thresholding of the hits with the lowest hit charges, this comes about as a result of the elevated hit threshold, required to minimise the number of reconstructed noise hits, as shown in Figure 6.8. Whilst nothing can be done retrospectively concerning the omission of the lowest charge hits, the highest charge hits, which cause the tails at low hit *RMS/Charge*, can be removed. This can be done by not using hits which are in the tails of the hit *Charge* distribution. The tails of the distributions are removed by considering a plot of normalised hit charge, whereby the most probable hit charge has a value of 1. A conservative cut on normalised hit charges of 0.25 is made, so that it can be guaranteed that the tails are removed. This is shown in Figure 6.19, and means that any hits with charges less than ~ 65 ADC, and any hits with charges more than ~ 170 ADC are not used. This will have the effect of removing some of the low charge hits which were reconstructed, but the main effect will be the removal of the significant number of high charge hits, which introduce the tail at low hit *RMS/Charge*. This is shown in Figure 6.16. The difference in the predicted and reconstructed hit times should then be centred around the interaction time, and be distributed much more uniformly. This will mean that the interaction time can be determined much more accurately.

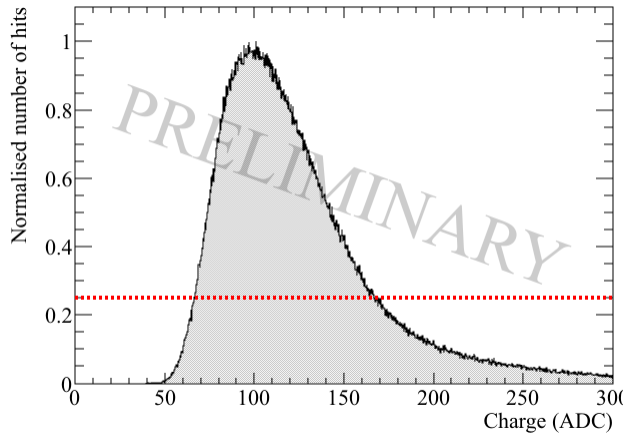


Fig. 6.19 The distribution of normalised hit charge, shown in units of ADC, in the 35 ton dataset. The number of hits with the most probable hit charge has been normalised to a value of 1. A cut on the normalised number of hits being greater than 0.25 is shown, the aim of this cut is to remove the tails of the hit charge distribution.

1 An intrinsic assumption in this method is that the track has a large number of collection
 2 plane hits, which do not contain delta rays, and are on wires which would not be identified as
 3 noisy. The tracks being considered here will have crossed all z values in the detector, meaning
 4 that a total of 336 collection hits could potentially be reconstructed. Given the reconstruction
 5 problems in the 35 ton detector, very few tracks will have hits on all of these collection
 6 wires. However, requiring at least 100 collection plane hits is not unreasonable, and would
 7 correspond to a reconstructed track length of at least 50 cm. The difference between the
 8 predicted and reconstructed hit time for each hit is shown in Figure 6.20, for both the hit
 9 *RMS* and hit *RMS/Charge* metrics.

10
 11 Figure 6.20 shows that both distributions are centred around a time difference of $0 \mu\text{s}$
 12 in the 35 ton dataset. This is encouraging as it shows that the method has potential. The
 13 width of the distribution for the *RMS/Charge* metric is smaller, and the peak larger, so it is
 14 expected that this will provide the more robust metric. This is because these features show
 15 that the predicted hit times are likely to be close to the reconstructed hit times. The peaks are
 16 centred around a time difference of 0, as the hit times had previously been corrected using
 17 the measured interaction time from the counter coincidence. This was done so as to avoid
 18 the uncertainty which would arise from allowing the coincidences to remain at random times
 19 between ticks 5000 and 6000, in the 15000 tick event. For an explanation as to why this
 20 occurs, see the discussion concerning Figure 6.2.

21

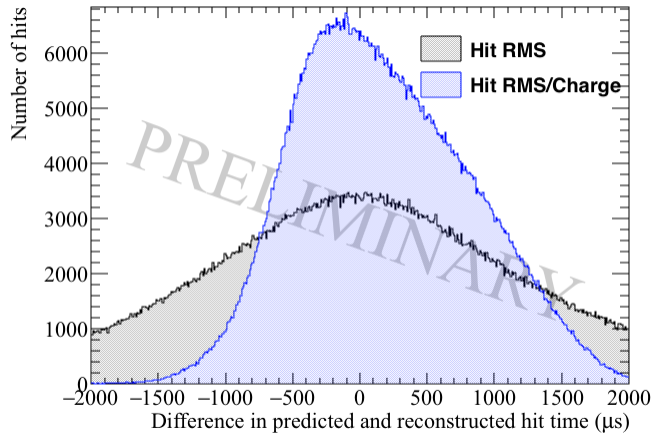
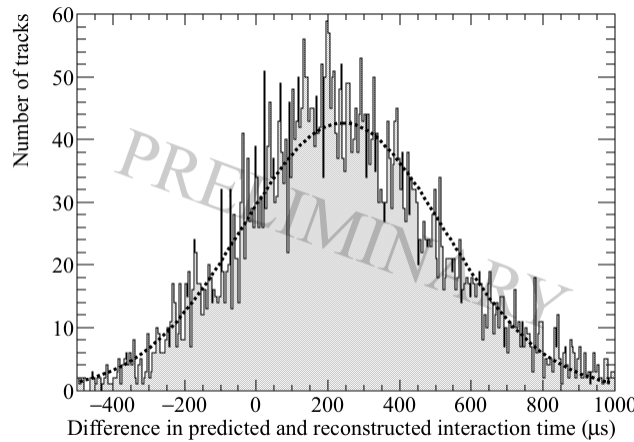


Fig. 6.20 The difference between the predicted and reconstructed hit times in the 35 ton dataset. The differences in time when the hit *RMS* metric is used are shown in black, whilst the differences in time when the hit *RMS/Charge* metric is used are shown in blue.

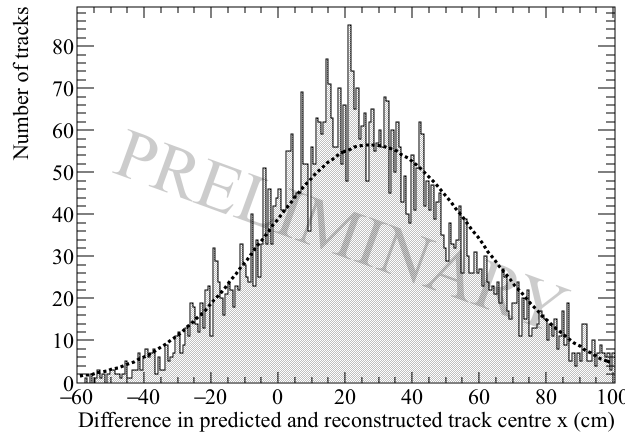
When evaluating interaction times the average difference in reconstructed and predicted hit times across every hit on the track must be considered. This is shown in Figures 6.21 and 6.22, where, as expected from Figure 6.20, the *RMS/Charge* metric provides a better estimation of the interaction time. The reason for this is that by utilising the charge information due to losses from impurities, this metric gains an extra handle on the drift distance, and hence the reconstructed time of the hits. The losses due to impurities are difficult to measure in high-purity LAr environments, as the decrease in collected charge with increasing drift distances is small [38]. The effect of increasing LAr purity is shown in Section 6.5.3. Using the change in hit charge in the 35 ton may have a drawback though, because, as shown in Figure 6.8, there is a threshold effect for hits with large drift times. However, as the same threshold effect is present in all 35 ton data samples, the limitation it introduces is mainly in the efficiency with which 'good' collection plane hits will be reconstructed, and so this information can be confidently used.

Figure 6.21 shows that using the effects of diffusion, and the hit *RMS*, the interaction time and central *x* position of a track, can be reliably predicted in the 35 ton dataset. The accuracy in determining the interaction time is found to be 240 μ s, where the distribution has a FWHM of 281 μ s. When this is converted into the difference in central *x* position of the track, the accuracy is found to be 27.7 cm, with a FWHM of 32.1 cm.

Figure 6.22 shows that using the effects of diffusion, and the hit *RMS/Charge*, the interaction time and central *x* position of a track, can be reliably predicted in the 35 ton dataset.



(a) The average difference in interaction times using the hit *RMS* metric.



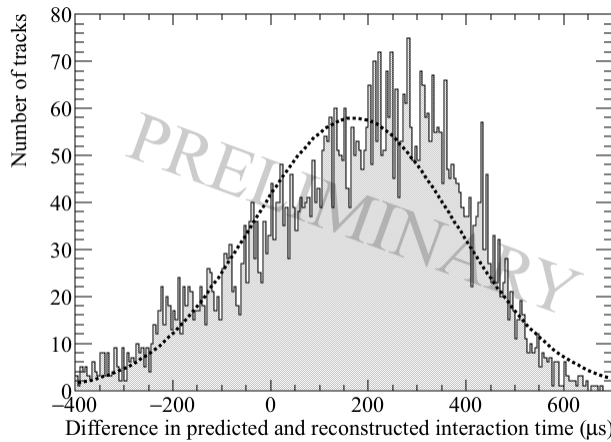
(b) The average difference in the central *x* position of a track using the hit *RMS* metric.

Fig. 6.21 The accuracy of the hit *RMS* method in the 35 ton dataset. Top shows the accuracy to which interaction times can be determined in μs . Bottom shows the accuracy to which the central *x* position of a track can be determined. Gaussian functions are fitted to the distributions so that any offset in the predicted times or positions can be discerned.

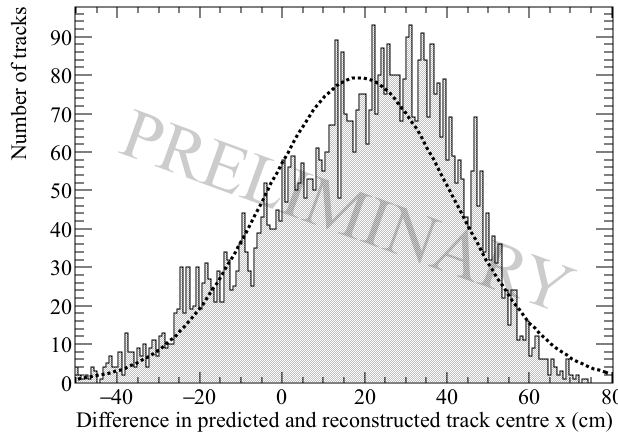
¹ The accuracy in determining the interaction time is found to be $171 \mu\text{s}$, where the distribution
² has a FWHM of $210 \mu\text{s}$. When this is converted into the difference in central *x* position of
³ the track, the accuracy is found to be 18.5 cm , with a FWHM of 23.0 cm .

⁴

⁵ The resolutions found are quite impressive, as given that the total drift time for electrons
⁶ through the whole 35 ton detector volume of 250 cm is roughly 5200 ticks, it means that
⁷ tracks can be cleanly distinguished throughout the detector volume. Though the resolution



(a) The average difference in interaction times using the hit *RMS/Charge* metric.



(b) The average difference in the central *x* position of a track using the hit *RMS/Charge* metric.

Fig. 6.22 The accuracy of the hit *RMS/Charge* method in the 35 ton dataset. Top shows the accuracy to which interaction times can be determined in μs . Bottom shows the accuracy to which the central *x* position of a track can be determined. Gaussian functions are fitted to the distributions so that any offset in the predicted times or positions can be discerned.

of the interaction time determination is impressive, it is concerning that there appears to be a systematic offset which has been introduced. This is seen by the distributions not being centred around a difference in predicted and reconstructed times of $0 \mu\text{s}$, as would be expected from the discussion concerning Figure 6.20. As discussed earlier, the issues with noise in the 35 ton dataset affect the accuracy with which tracking and calorimetry can be performed, and so it is reasonable to expect that the effectiveness of the interaction time determination was also affected. Therefore, it is prudent to repeat the study on a Monte Carlo

1
2
3
4
5
6
7

¹ sample, with the same detector conditions, but a much lower level of detector noise. This is
² presented in Section 6.5.2.

³

⁴ **6.5.2 Determining interaction times in a low-noise detector using Monte Carlo, and differences with data**

⁵

⁶ When determining interaction times in Monte Carlo simulations, exactly the same criteria
⁷ are applied to the hits. This is because δ -rays would still change the measured hit width, and
⁸ will be present in any sample. In a low noise detector it is expected that few wires would
⁹ be removed due to being noisy, but for consistency there is no danger in applying this cut.
¹⁰ Imposing a minimum number of collection plane hits is again important to ensure that the
¹¹ distribution of predicted hit times is centred on the interaction time. In addition to the same
¹² criteria being imposed on which wires are used, the same metrics are calculated. In all plots
¹³ shown below the Monte Carlo dataset has been normalised to the size of the 35 ton dataset.
¹⁴ This was done so that the area of the plots shown was the same, enabling easier comparison
¹⁵ between the two datasets.

¹⁶

¹⁷ Figure 6.23 shows both the hit *RMS* and hit *RMS/Charge* distributions, for hits from
¹⁸ tracks that are associated with a coincidence that has a counter difference of 4, and are
¹⁹ between 20 cm and 30 cm away from the APAs, or between 140 cm and 150 cm from the
²⁰ APAs. It can be seen that there is a large difference in the distributions for hits which are
²¹ relatively close to the APAs, at distances between 20 cm and 30 cm. The distributions are
²² also much more tightly distributed in the Monte Carlo sample, showing that the variation
²³ between hits is much smaller. However, the difference between the Monte Carlo and 35 ton
²⁴ data samples are much smaller at large drift distances, showing that at large distances the
²⁵ distributions become much more varied. An important feature of the 35 ton data sample,
²⁶ which is not present in the Monte Carlo sample, is the sudden cut off in values of high hit
²⁷ *RMS/Charge*. This was briefly discussed in the consideration of Figure 6.16, but it is much
²⁸ clearer in Figure 6.23d, where the rapid decrease in the number of hits with values of hit
²⁹ *RMS/Charge* which are more than 0.038 ticks ADC^{-1} seen in the 35 ton dataset, is not
³⁰ repeated in the Monte Carlo sample. This, along with Figure 6.8, shows clear evidence that
³¹ the hits with low values of hit *charge* are not reconstructed in the 35 ton data sample.

³²

³³ The most probable values of hit *RMS* at increasing drift distance are shown in Figure 6.24,
³⁴ where the Monte Carlo simulation is again shown with the values from the data. As was seen

6.5 Measuring interaction times using electron diffusion

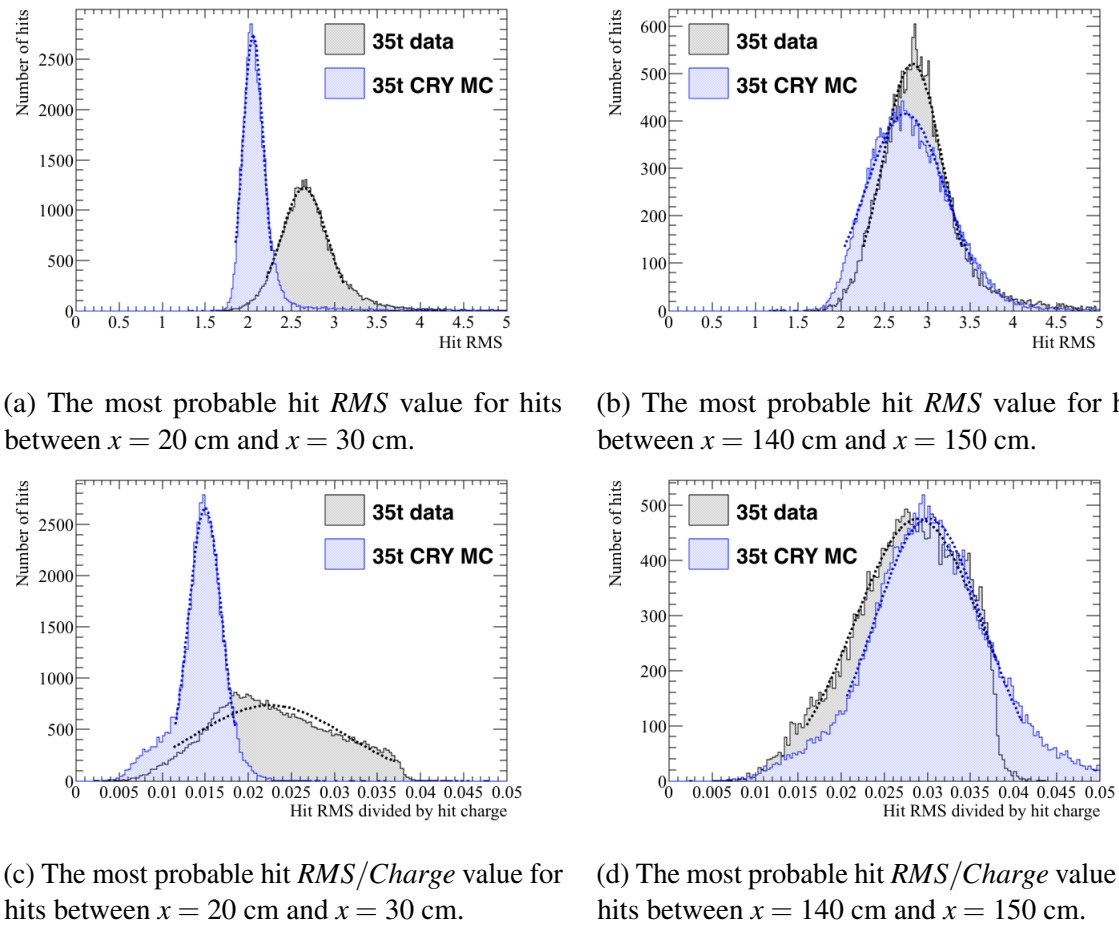


Fig. 6.23 The distribution of hit *RMS* (top), and hit *RMS/Charge* (bottom), for points between 20 and 30 cm from the APAs (left), and points between 140 and 150 cm from the APAs (right), for tracks associated with coincidences that have a counter differences of 4. The most probable values hit *RMS* and hit *RMS/Charge* are determined by fitting Gaussian functions around the peaks of the distributions. These fits are shown as dashed lines. The distributions for the 35 ton dataset are shown in black, whilst the distributions for the Monte Carlo simulation are shown in blue.

when considering the distributions at specific distances and counter differences, the most probable values of hit *RMS* in the Monte Carlo simulation is systematically lower than in the data. This is attributed to the elevated noise level seen in the data, because, as seen in Figure 6.15, when a noise base-line is added to a signal, the width of the signal increases. Another difference between the Monte Carlo and the data, is that the gradient of the most probable values of hit *RMS* in data is roughly half of that in the Monte Carlo. This could be due to an overestimation of the effect of longitudinal diffusion in the Monte Carlo sample, or, it could be due to the larger hit widths seen in the dataset at low drift distances, causing

1
2
3
4
5
6
7
8

6.5 Measuring interaction times using electron diffusion

the effects of diffusion to be less apparent. Evidence for the latter can be seen in the stark differences between the figures in Figure 6.23 at relatively short drift distances, compared to the similarities seen at large drift distances, where it appears that the Monte Carlo accurately simulates the distributions seen in the 35 ton dataset.

5

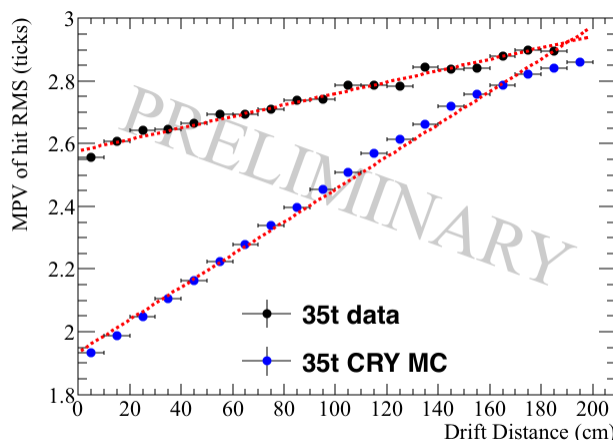


Fig. 6.24 The most probable values of hit *RMS* as a function of drift distance, for tracks associated with a coincidence that had a counter difference of 4. The distribution for the 35 ton dataset is shown in black, whilst the distribution for the Monte Carlo simulation is shown in blue.

The most probable value of hit *RMS* at a drift distance of 0 cm for a range of counter differences is shown in Figure 6.25. The change in MPV of hit *RMS* can be seen to increase for both the Monte Carlo and 35 ton data samples, which again shows that the effects of diffusion can be seen to be track angle dependant. However, the way in which the MPV of hit *RMS* increases is different in the two samples. The increased MPVs of hit *RMS* seen in the 35 ton dataset, is again prescribed to the increase in hit width caused by the elevated noise level.

13

Upon calculating the fit metrics in the low-noise Monte Carlo dataset it is then possible to use these to predict track interaction times. However, it is first necessary to calculate the normalised hit charge distributions as was done for the 35 ton dataset. This is shown in Figure 6.26. It can be seen that there are hits with lower values of hit *charge* in the Monte Carlo sample, supporting the idea that there is a thresholding effect in the 35 ton dataset. Importantly however, the aim of the cut to remove the tails of the hit *charge* distributions can be seen to be successful in both the 35 ton dataset and Monte Carlo sample, as hits with large value of hit *charge* are removed in both samples. The result of this will be that, the

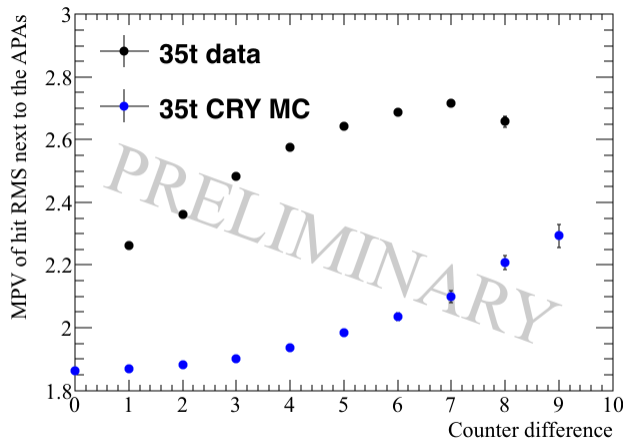


Fig. 6.25 The most probable values of hit *RMS* within 10 cm of the APAs, as a function of the counter difference of the coincidence, that the track was associated with. The distribution for the 35 ton dataset is shown in black, whilst the distribution for the Monte Carlo simulation is shown in blue.

difference in predicted and reconstructed hit times, for a given track, will be centred on the interaction time of the track, as was presented in the discussion of Figure 6.19. The Monte Carlo hit times have been corrected using the time of the counter coincidence, as was the case for the 35 ton dataset.

Figure 6.27 compares how reliably the interaction time, and central *x* position of a track, can be predicted using the effect that diffusion has on the hit *RMS*, in the 35 ton dataset and a low-noise Monte Carlo sample. The accuracy in determining the interaction time in Monte Carlo (data) is found to be, 108 (240) μ s, where the distribution has a FWHM of 98 (281) μ s. When this is converted into the difference in central *x* position of the track, the accuracy is found to be, 11.8 (27.7) cm with a FWHM of 10.9 (32.1) cm.

Figure 6.28 compares how reliably the interaction time, and central *x* position, of a track can be predicted using the effect that diffusion has on the hit *RMS/Charge*, in the 35 ton dataset and a low-noise Monte Carlo sample. The accuracy in determining the interaction time in Monte Carlo (data) is found to be, -3 (171) μ s, where the distribution has a FWHM of 114 (210) μ s. When this is converted into the difference in central *x* position of the track, the accuracy is found to be, -0.4 (18.5) cm with a FWHM of 12.6 (23.0) cm.

The hit *RMS/Charge* metric appears to be able to more accurately predict interaction times, as was seen in when considering the only 35 ton dataset. This is again due to the

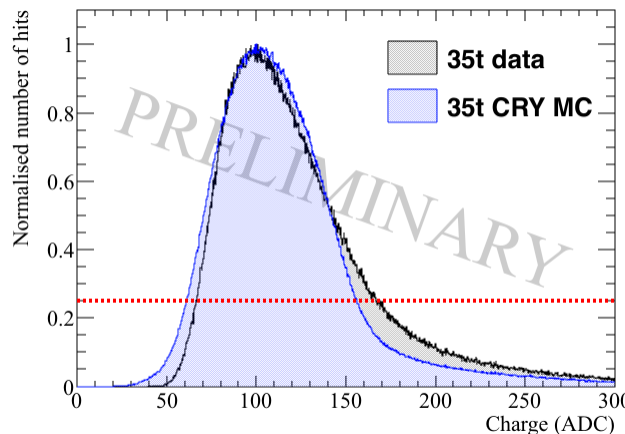
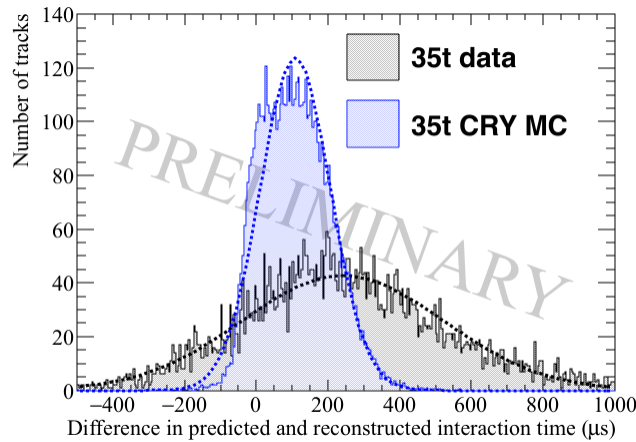


Fig. 6.26 The distribution of normalised hit charge, shown in units of ADC, in the 35 ton dataset and Monte Carlo sample. The number of hits with the most probable hit charge has been normalised to a value of 1. A cut on the normalised number of hits being greater than 0.25 is shown, the aim of this cut is to remove the tails of the hit charge distribution. The distribution for the 35 ton dataset is shown in black, whilst the distribution for the Monte Carlo simulation is shown in blue.

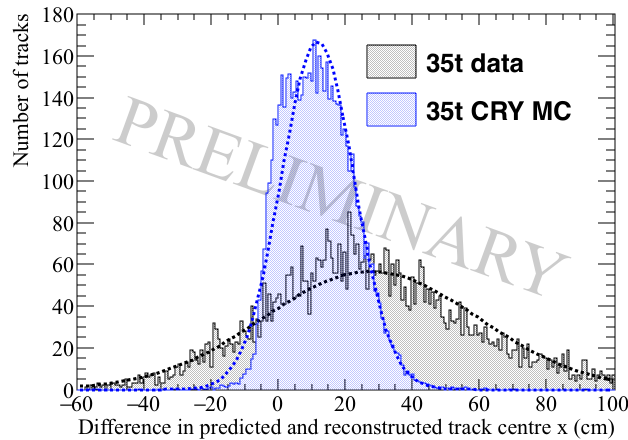
¹ ability to incorporate information about loses due to impurities, which increase with drift
² distance. Also, as expected from the previous figures and the lower noise state in the Monte
³ Carlo, it is seen that the interaction times predicted in the Monte Carlo sample more closely
⁴ match the true interaction times, than was the case with the predictions made in the dataset.
⁵ An important feature to observe is that, as well as more accurately predicting the interaction
⁶ times, the widths of the distributions in Monte Carlo are less than half of that in the data,
⁷ particularly when using the hit *RMS*, as shown in Figure 6.27. This means that the resolution
⁸ with which tracks can be distinguished in the Monte Carlo sample is much better than in the
⁹ 35 ton dataset, again this is attributed to the lower noise level in the Monte Carlo.

¹⁰
¹¹ The calculation of interaction times is clearly much better in the low-noise Monte Carlo
¹² dataset, than in the 35 ton dataset. However, the distributions when using the hit *RMS* are
¹³ still not centred around 0, implying that there is a systematic error in the method, which
¹⁴ has not been removed when considering a low-noise environment. The cut applied on
¹⁵ the normalised hit *charge* distribution was applied in order to remove the tails of the hit
¹⁶ *RMS/Charge* distribution, as seen in Figure 6.26. Given that Figure 6.28 shows that when
¹⁷ using this metric, the predicted interaction times are centred on the reconstructed interaction
¹⁸ times, this appears to have been successful. However, the analogous cut is not performed

6.5 Measuring interaction times using electron diffusion



(a) The average difference in interaction times using the hit *RMS* metric.



(b) The average difference in the central *x* position of a track using the hit *RMS* metric.

Fig. 6.27 The accuracy of the hit *RMS* method in the 35 ton dataset and a Monte Carlo simulation. Top shows the accuracy to which interaction times can be determined in μs . Bottom shows the accuracy to which the central *x* position of a track can be determined. Gaussian functions are fitted to the distributions so that any offset in the predicted times or positions can be discerned. The distributions for the 35 ton dataset are shown in black, whilst the distributions for the Monte Carlo simulation are shown in blue

on the hit *RMS* distribution, and so this could explain the decreased accuracy using this metric.

It is also possible that some δ -rays have not been removed. This is because the only way to remove hits containing unseparated δ -rays, is to look for the slight dip in the raw signal, which is associated with the δ -ray beginning to separate from the main track. This would be

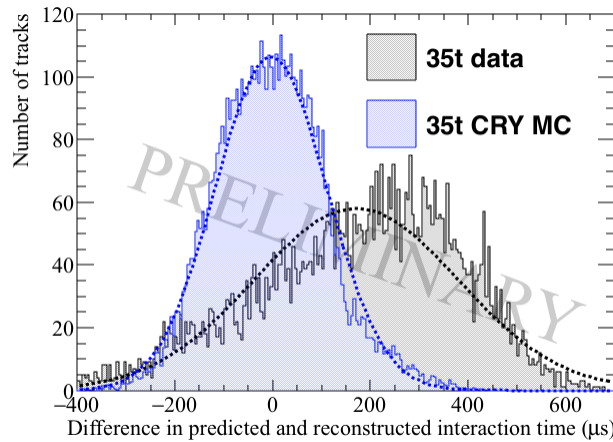
1

2

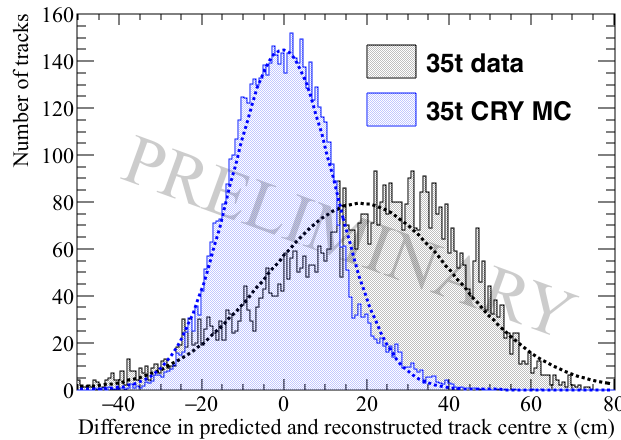
3

4

5



(a) The average difference in interaction times using the hit *RMS/Charge* metric.



(b) The average difference in the central *x* position of a track using the hit *RMS/Charge* metric.

Fig. 6.28 The accuracy of the hit *RMS/Charge* method in the 35 ton dataset and a Monte Carlo simulation. Top shows the accuracy to which interaction times can be determined in μs . Bottom shows the accuracy to which the central *x* position of a track can be determined. Gaussian functions are fitted to the distributions so that any offset in the predicted times or positions can be discerned. The distributions for the 35 ton dataset are shown in black, whilst the distributions for the Monte Carlo simulation are shown in blue

¹ almost impossible in the 35 ton dataset given the oscillatory nature of the noise. Were a cut
² on hit *RMS* to be applied, then these indistinguishable δ -rays would likely be removed. This
³ is because hits with delta rays would lie in the high value tails of the hit *RMS* distribution,
⁴ which the cut would remove.

The 35 ton dataset as a whole overestimates the interaction times though, and it is thought that this is due to elevated noise level. Justification for this assertion is discussed in Section 6.5.3 where the detector conditions of a simulated detector are varied. One of the detector conditions which is varied is the noise level in the detector.

6.5.3 Discerning the impact of changing detector properties using Monte Carlo samples

Much has been made of the difficulty that the noise level in the 35 ton dataset introduces, when performing reconstruction and analysis of the data. It is necessary to verify this claim, and so a sample of Monte Carlo events with increasing noise levels is produced, and analysed below. The noise level in the Monte Carlo samples is increased from the low-noise state used in the previous section, to a level more similar to that which is seen in the 35 ton dataset. If the claim that the noise level made reconstruction more difficult is correct, then the the accuracy with which the interaction time can be determined should be seen to anti-correlate with the noise level of the simulated detector. In addition to varying noise levels, the electron lifetime, the electric field, and the constant of longitudinal diffusion are varied. All samples have used the same initial muons, this is done so that the only difference between the different samples are the detector conditions. Only one detector condition is varied at a time, so that the effect of each detector condition can be studied in isolation. As only one detector property is changed between samples, there is one sample that is consistent to all sample sets. This is when the RMS of the noise is 2.5 ADCs, the electron lifetime is 3 ms, the electric field is 500 V cm^{-1} , and the coefficient of longitudinal diffusion is $6.2 \times 10^9 \text{ cm}^2 \text{ ns}^{-1}$. When presenting the studies with changing detector conditions, only the accuracy with the which the interaction time, and central x position of a track, can be predicted is shown here. A more robust collection of figures can be seen in Appendix A.

Figures 6.29 and 6.30 show the accuracy to which the interaction time, and central x position of a track, can be determined using the effect that diffusion has on the hit *RMS* and hit *RMS/Charge*, as the noise level in the detector changes. Figures 6.29 and 6.30 both show that the accuracy of the fits decrease with increasing noise levels, but they show this decrease in accuracy is manifested in different ways. As discussed in Section 6.3, the 35 ton data had significant amounts of coherent noise which was not expected, and so this had not previously been simulated. As this level of coherent noise is not expected in future detectors, coherent noise has not been simulated in these increased noise level samples.

6.5 Measuring interaction times using electron diffusion

92

1 Instead, the electronics noise, or 'thermal noise,' has been varied. The lowest noise level
2 was the design noise level for the 35 ton, and is what is used in the 'baseline' sample in the
3 plots to follow. This level of thermal noise is very minimal, and so only noise levels which
4 are more than this have been simulated. This is because the *signal/noise* ratio which one
5 gets with such a low ADC RMS is large, and so a decrease in this noise level is unlikely
6 to make a significant difference in the accuracy of the method. However, as can be seen
7 in the 35 ton data, and the following plots, increasing the noise level has serious consequences.

8

9 No noise mitigation algorithms have been applied to the increased noise samples shown
10 here. Instead, the threshold that the hit finder uses has been increased to the level that was
11 necessary for a reasonable number of hits to be reconstructed. A reasonable number of hits
12 simply means, not reconstructing such a large number of noise hits that they outweigh the
13 number of true signals from tracks. The hit threshold which was required was determined by
14 looking at the deconvoluted signal, and choosing a threshold which was above the majority
15 of the noise signals. The hit threshold used for each level are summarised below:

- 16 • Noise level of 2.5 ADC RMS - hit threshold of 6 ADC
17 • Noise level of 5 ADC RMS - hit threshold of 10 ADC
18 • Noise level of 7.5 ADC RMS - hit threshold of 15 ADC
19 • Noise level of 10 ADC RMS - hit threshold of 20 ADC

20 This means that the main effect of increasing the noise level is to remove the low charge hits,
21 as they will fall below the hit threshold, as it is increased to compensate for the increased
22 noise level.

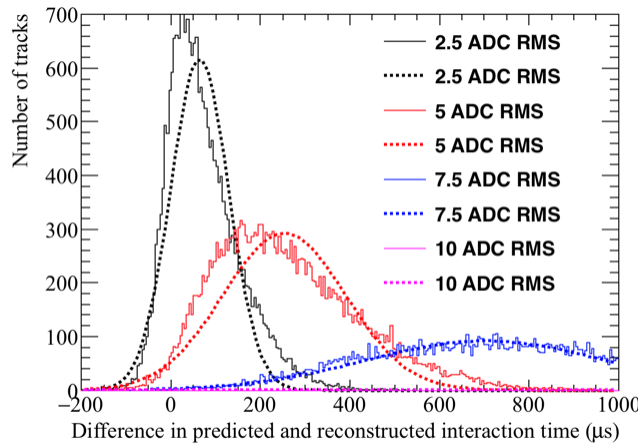
23

24 Firstly, considering Figure 6.29, it can be seen that the accuracy to which interaction
25 times can be determined rapidly decreases as the noise level increases. This is partly due to
26 the fits used to make the prediction metrics not converging for counter differences of 1, 2, 3
27 and 4, where the MPV of hit *RMS* is not seen to increase for increasing drift distances. For
28 evidence of this, see the Figures in Appendix A. Though this is the extreme case, it can be
29 seen that the validity of the hit *RMS* for increasing drift distances becomes less predictable
30 as the noise is increased. The result of this is a less accurate prediction metric, which leads
31 to the large offsets and widths of the distributions that are shown in Figure 6.29.

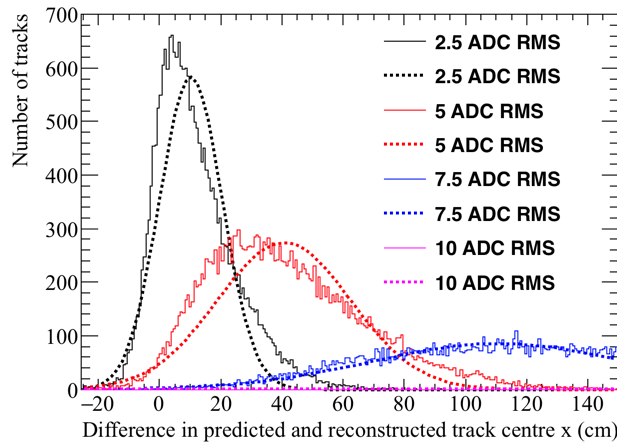
32

33 The most striking feature of Figure 6.30 is the decrease in statistics seen for the increasing
34 noise levels. This shows the effect that increasing the noise level, and hence hit threshold has.

6.5 Measuring interaction times using electron diffusion



(a) The average difference in interaction times using the hit *RMS* metric.



(b) The average difference in the central *x* position of a track using the hit *RMS* metric.

Fig. 6.29 The accuracy of the hit *RMS* method, for different electronic noise levels. Top shows the accuracy to which interaction times can be determined in μs . Bottom shows the accuracy to which the central *x* position of a track can be determined. Gaussian functions are fitted to the distributions so that any offset in the predicted times or positions can be discerned.

This is because fewer tracks in total are reconstructed, and those that are reconstructed are less likely to meet the criteria about the number of collection hits required to make predictions.

Figures 6.31 and 6.32, show the accuracy to which the interaction time, and central *x* position of a track, can be determined using the effect that diffusion has on the hit *RMS* and hit *RMS/Charge*, for changing electron lifetimes. Figure 6.31 shows that with an electron

1

2

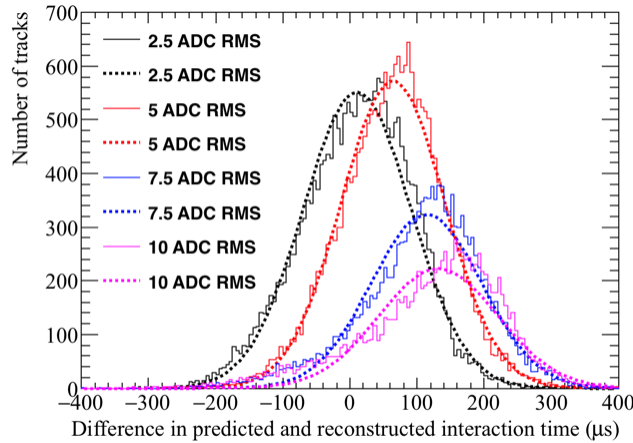
3

4

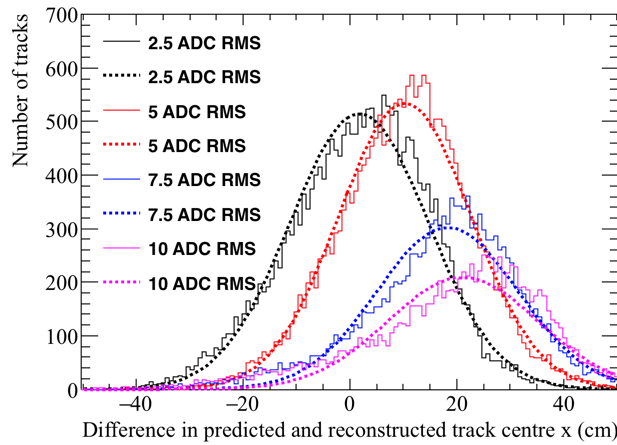
5

6

6.5 Measuring interaction times using electron diffusion



(a) The average difference in interaction times using the hit *RMS/Charge* metric.



(b) The average difference in the central x position of a track using the hit *RMS/Charge* metric.

Fig. 6.30 The accuracy of the hit *RMS/Charge* method, for different electronic noise levels. Top shows the accuracy to which interaction times can be determined in μs . Bottom shows the accuracy to which the central x position of a track can be determined. Gaussian functions are fitted to the distributions so that any offset in the predicted times or positions can be discerned.

¹ lifetime of 1 ms, the hit *RMS* metric is very inaccurate, this is likely due to hits which are a
² large distance away from the APAs being very difficult to reconstruct, due to the extremely
³ poor lifetime. For this reason, the accuracy to which the hit *RMS* metric predicts the interac-
⁴ tion time improves as the electron lifetime increases, though this increase is small between
⁵ the 3 ms, 5 ms and 8 ms samples. Figure 6.32 shows the opposite effect, the accuracy to
⁶ which the interaction time can be determined decreases with increasing electron lifetime for

the hit *RMS/Charge* metric. This is shown by the widths of the distribution increasing as the electron lifetime increases. This happens because the decrease in hit charge is much greater when the electron lifetime is lower, and this dependence is the corner stone of this metric. The large decrease in hit charge for low electron lifetimes is why this metric performs so well for low electron lifetimes, and so the decrease in its accuracy is an unavoidable consequence of increasing electron lifetime.

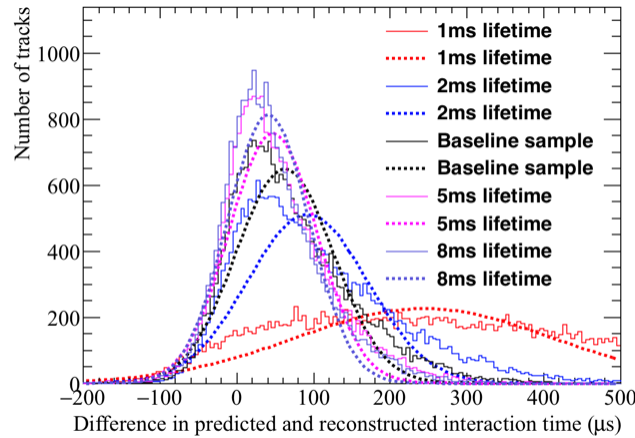
Figures 6.33 and 6.34, show the accuracy to which the interaction time, and central x position of a track, can be determined using the effect that diffusion has on the hit *RMS* and hit *RMS/Charge*, for changing electric field values. Figure 6.33 shows that the accuracy to which the interaction time can be predicted, decreases with increasing electric field. This is shown by the introduction of an offset in the predicted interaction time for lower values of electric field strength. However, when these interaction times are converted to the central x position of a track, the accuracy is relatively unaffected by electric field strength, due to the slower drift velocities at low electric field strengths. The opposite is shown in Figure 6.34, as the accuracy to which interaction time can be predicted does not see the introduction of an offset, and is better for the samples with lower electric field strengths. As the interaction times are accurately predicted, there is no offset seen in the predicted central x position. This shows that the hit *RMS/Charge* method is unaffected by electric field strength.

Figures 6.35 and 6.36, show the accuracy to which the interaction time, and central x position of a track, can be determined using the effect that diffusion has on the hit *RMS* and hit *RMS/Charge*, for changing values of the longitudinal diffusion constant. As would be expected, both figures show that the accuracy to which the interaction time and central x position can be predicted are highly dependant on the longitudinal diffusion constant. This is seen by the distributions becoming much narrower, and more closely centred around the true interaction time, or central x position, as the constant of longitudinal diffusion increases. It is interesting to note that the extremely poor resolution seen in Figure 6.35 when there is no longitudinal diffusion, is not present in Figure 6.36. It is thought that this is due to the effect of charge attenuation, which will still occur because of the finite electron lifetime.

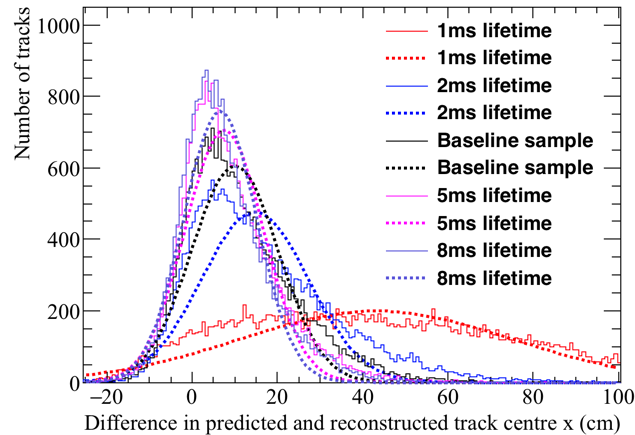
6.5.4 The limitations of and future improvements to the method of interaction time determination using diffusion

The comparison of the 35 ton data and Monte Carlo samples, as well as the Monte Carlo samples with differing detector conditions, show that there is potential in the ability to

6.5 Measuring interaction times using electron diffusion



(a) The average difference in interaction times using the hit *RMS* metric.



(b) The average difference in the central *x* position of a track using the hit *RMS* metric.

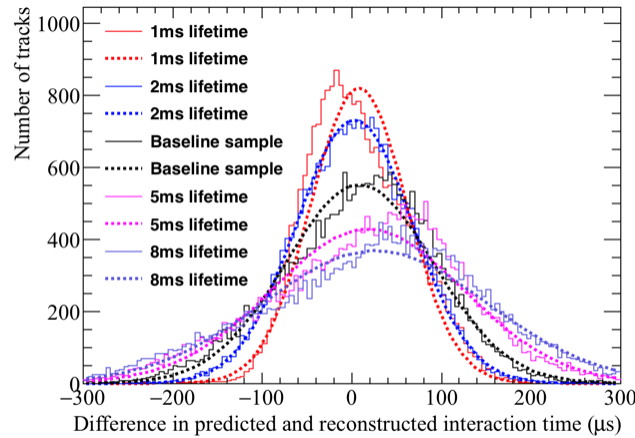
Fig. 6.31 The accuracy of the hit *RMS* method, for changing values of the electron lifetime. Top shows the accuracy to which interaction times can be determined in μs . Bottom shows the accuracy to which the central *x* position of a track can be determined. Gaussian functions are fitted to the distributions so that any offset in the predicted times or positions can be discerned.

¹ determine interaction times using the effects of diffusion. However, there are still some
² issues which need to be overcome. These will be discussed briefly below.

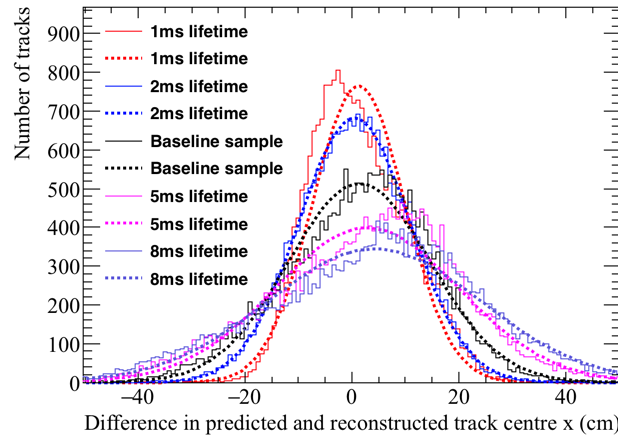
³

⁴ Many of the figures shown still have slight offsets even though the tails of the hit charge
⁵ distributions have been removed. However, these offsets are generally confined to detector
⁶ conditions which would not be considered optimal, such as very low electron lifetimes (1 ms)

6.5 Measuring interaction times using electron diffusion



(a) The average difference in interaction times using the hit *RMS/Charge* metric.

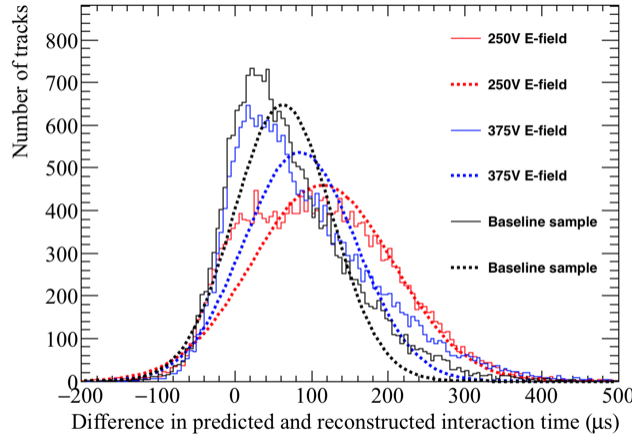


(b) The average difference in the central x position of a track using the hit *RMS/Charge* metric.

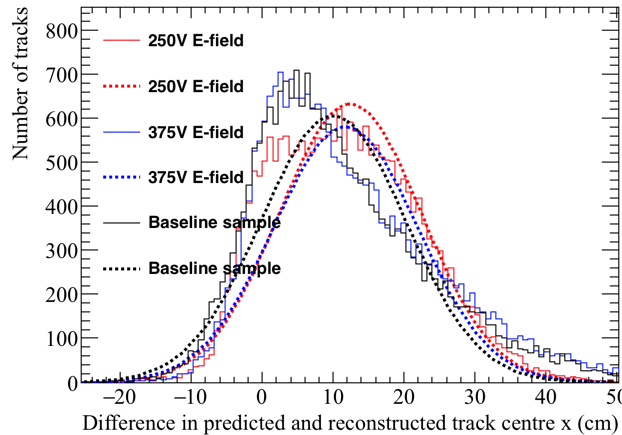
Fig. 6.32 The accuracy of the hit *RMS/Charge* method, for changing values of the electron lifetime. Top shows the accuracy to which interaction times can be determined in μ s. Bottom shows the accuracy to which the central x position of a track can be determined. Gaussian functions are fitted to the distributions so that any offset in the predicted times or positions can be discerned.

or high detector noise. The latter is seen to be the case when considering the 35 ton dataset, where the high noise scale can be seen to affect the accuracy to which the interaction time, and central x position, can be determined. A potential solution to reduce these offsets, and also to reduce the width of the distributions, is to perform the interaction time determination twice. The result of the first run, which is what was shown earlier, would then be used to select only hits which lie within the expected regions of hit *RMS* and hit *RMS/Charge*. This

6.5 Measuring interaction times using electron diffusion



(a) The average difference in interaction times using the hit *RMS* metric.

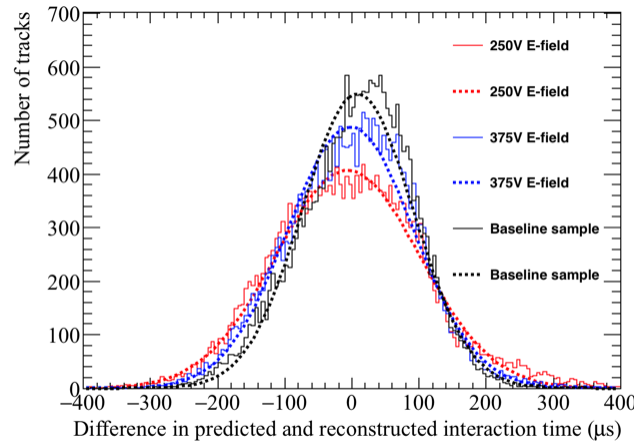


(b) The average difference in the central *x* position of a track using the hit *RMS* metric.

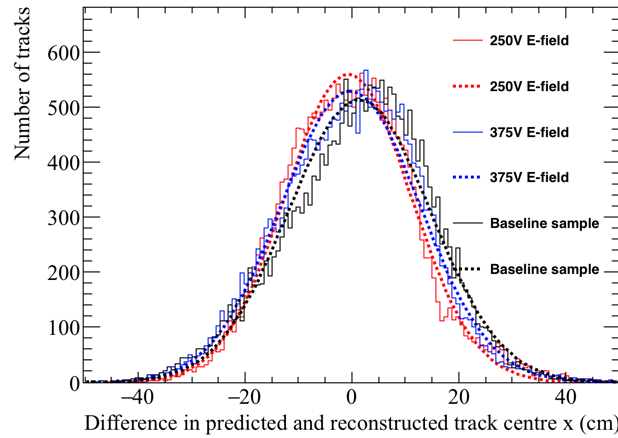
Fig. 6.33 The accuracy of the hit *RMS* method, for changing values of the electric field. Top shows the accuracy to which interaction times can be determined in μs . Bottom shows the accuracy to which the central *x* position of a track can be determined. Gaussian functions are fitted to the distributions so that any offset in the predicted times or positions can be discerned.

¹ would be possible as the initial interaction time determination could be used to work out the
² rough *x* positions of hits, and then only hits which lie within $N \sigma$ of the MPV would be used
³ to determine the interaction time from the second pass. When performing the second pass of
⁴ interaction time determination, N would be a user defined parameter, but would likely be
⁵ less than 2, so as to exclude the beginnings of the tails of the hit *RMS*, and hit *RMS/Charge*,

6.5 Measuring interaction times using electron diffusion



(a) The average difference in interaction times using the hit *RMS/Charge* metric.



(b) The average difference in the central x position of a track using the hit *RMS/Charge* metric.

Fig. 6.34 The accuracy of the hit *RMS/Charge* method, for changing values of the electric field. Top shows the accuracy to which interaction times can be determined in μs . Bottom shows the accuracy to which the central x position of a track can be determined. Gaussian functions are fitted to the distributions so that any offset in the predicted times or positions can be discerned.

distributions.

An important improvement to the method would be to expand it to include the induction plane wires, as this will greatly increase both the number of wires which can be used, and the range of track angles whose interaction times can be predicted. The angular range of the method would increase, as when using only collection plane wires it is impossible to

1

2

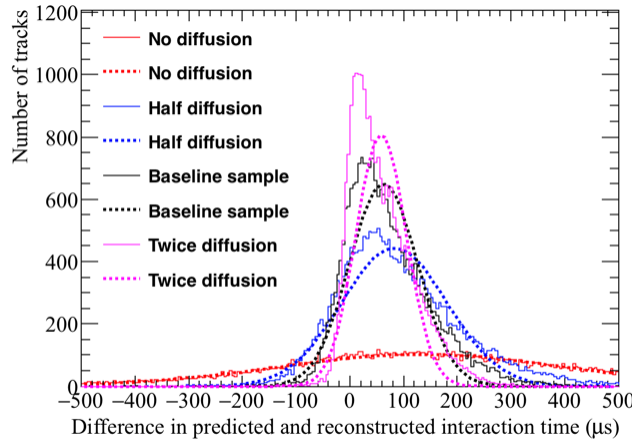
3

4

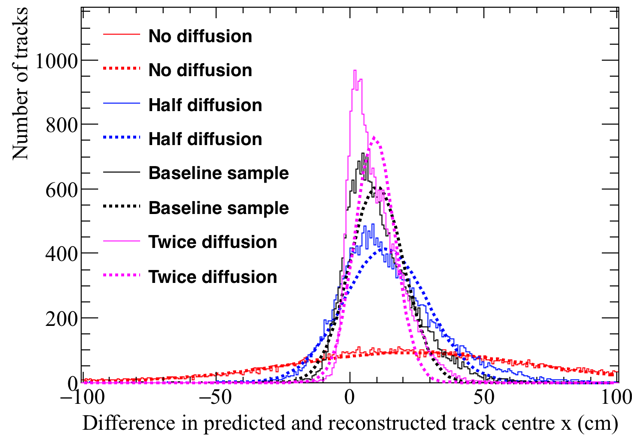
5

6

6.5 Measuring interaction times using electron diffusion



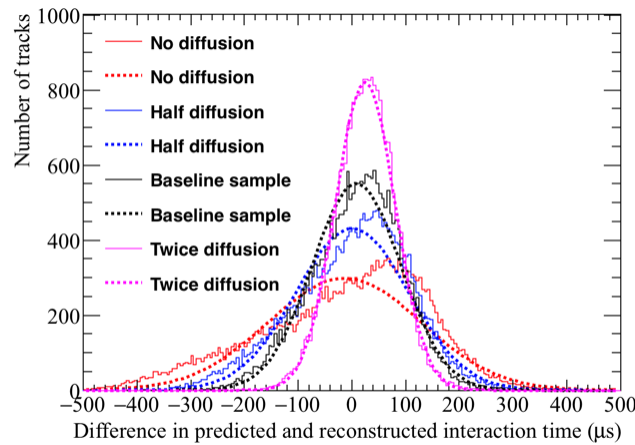
(a) The average difference in interaction times using the hit *RMS* metric.



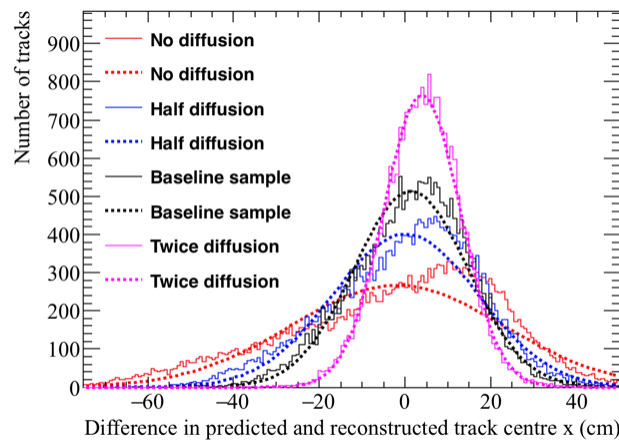
(b) The average difference in the central *x* position of a track using the hit *RMS* metric.

Fig. 6.35 The accuracy of the hit *RMS* method, for changing values of the constant of longitudinal diffusion. Top shows the accuracy to which interaction times can be determined in μs . Bottom shows the accuracy to which the central *x* position of a track can be determined. Gaussian functions are fitted to the distributions so that any offset in the predicted times or positions can be discerned.

¹ reconstruct enough hits for nearly vertical muons, as very few wires would be hit. This was
² discussed in Section 5.3. This was not attempted here, as the electronics noise in the 35 ton
³ data was too large to able to reliably reconstruct all hits on the induction planes, without
⁴ reconstructing many noise hits. This meant that the hit threshold on the induction planes was
⁵ very high.



(a) The average difference in interaction times using the hit *RMS/Charge* metric.



(b) The average difference in the central x position of a track using the hit *RMS/Charge* metric.

Fig. 6.36 The accuracy of the hit *RMS/Charge* method, for changing values of the constant of longitudinal diffusion. Top shows the accuracy to which interaction times can be determined in μs . Bottom shows the accuracy to which the central x position of a track can be determined. Gaussian functions are fitted to the distributions so that any offset in the predicted times or positions can be discerned.

¹ Chapter 7

² Simulations of the DUNE Far Detector

³ Previous work presented has been done concerning the 35 ton prototype, however it is also
⁴ important to simulate the DUNE Far Detector (FD). Simulations in the FD have concen-
⁵ trated on cosmogenic background to neutrino oscillations, in Section 7.1, and the muon
⁶ background to nucleon decay, in Section 7.3. The simulations shown in Section 7.1 are
⁷ discussed in!!!! citepMartinsThesis!!!!, and were performed for the Long Baseline Neutrino
⁸ Experiment (LBNE), which along with the Long Baseline Neutrino Oscillation (LBNO)
⁹ experiment, formed the basis for DUNE, and so are included here for completeness. The
¹⁰ other work presented was performed for the DUNE collaboration, in conjunction with work
¹¹ done by Vitaly Kudryavtsev and Matthew Robinson, both of the University of Sheffield. This
¹² work was performed with the aim of producing muon-induced background limits to nucleon
¹³ decay in the DUNE FD.

¹⁴

¹⁵ 7.1 Simulations of the LBNE surface detector

¹⁶ 7.2 The use of MUSUN in LArSoft

¹⁷ The primary muons in the following discussions are all generated using MUSIC [8] [10] [11]
¹⁸ and MUSUN [8] [9], and so a brief overview of them is required. MUSIC first propagates
¹⁹ muons through a medium, defined by the user, for given initial energies, positions, and
²⁰ direction cosines. A range of energies between 10^2 and 10^7 GeV are considered, and their
²¹ energy distributions are stored at depths of between 100 and 15,000 m w.e. Energy losses
²² due to four processes are considered; ionisation, bremsstrahlung, electron-positron pair
²³ production and muon-nucleus inelastic scattering. The output of MUSIC is then used by

MUSUN to generate a muon energy spectrum and angular distribution, for a given detector location. MUSUN is able to use information about the local surface profile to make these distributions more accurate.

The location of the DUNE far detector, near the Ross shaft at SURF, has global coordinates of, $44^{\circ}20'45.21''$ North, $103^{\circ}45'16.13''$ West. The rock composition is assumed to be, $\langle Z \rangle = 12.09$ and $\langle A \rangle = 24.17$. The density is assumed to be 2.70 g cm^{-3} [39]. The flux calculated by MUSIC/MUSUN of $5.18 \times 10^{-9} \text{ cm}^{-2} \text{ s}^{-1} \text{ sr}^{-1}$, is well matched to the flux measured by the active veto system of the Davis' experiment, which was $(5.38 \pm 0.07) \times 10^{-9} \text{ cm}^{-2} \text{ s}^{-1} \text{ sr}^{-1}$ [40]. Given the small differences in these values, and another measurement by the Majorana demonstrator, the systematic uncertainty in calculating the muon flux is estimated to be 20% [41].

The surface profile around the proposed detector location is shown in Figure 7.1a, where the proposed location is in the centre of the map. Each quadrant on the map has been divided into 4 angles of 22° , to help guide the eye when comparing it to Figure 7.1b, where the distribution of azimuth angles is plotted. The vertical lines in Figure 7.1b show the division of the quadrants when the angle is calculated from East to the North. When moving from East to North it is possible to discern how the peaks and troughs on the surface profile, correspond to troughs and peaks, in the distribution of azimuthal angle.

Given these parameters, the muon flux at the DUNE far detector location, when assuming a spherical detector geometry, and without simulating a detector cavern, is given by Table 7.1.

Table 7.1 Muon flux parameters as calculated with MUSIC/MUSUN.

Total flux ($\text{cm}^{-2} \text{ s}^{-1}$)	Mean E_{μ} (GeV)	Mean slant depth (m w.e)	Mean θ ($^{\circ}$)
5.66×10^{-9}	283	4532	26

The muons simulated for DUNE are sampled on the surface of a box surrounding the detector hall, that also encompasses 7 m of rock above the cavern, and 5 m of rock on all other sides. This is to ensure that the simulated muons pass through a sufficient amount of rock to induce cascades, both above and around the detector hall. The secondaries produced in these cascades which enter the detector, in the absence of the initial muon, are of particular interest, as they could be mistaken for nucleon decay events. The study of these nucleon decay mimicking events is discussed in Section 7.3. The size of the box which the muons

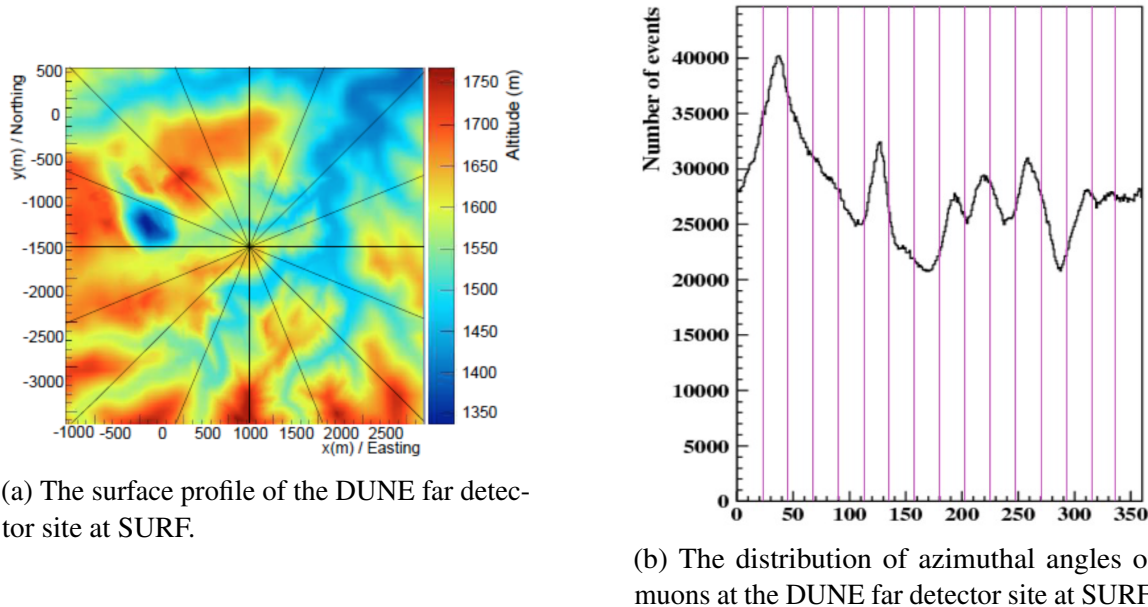
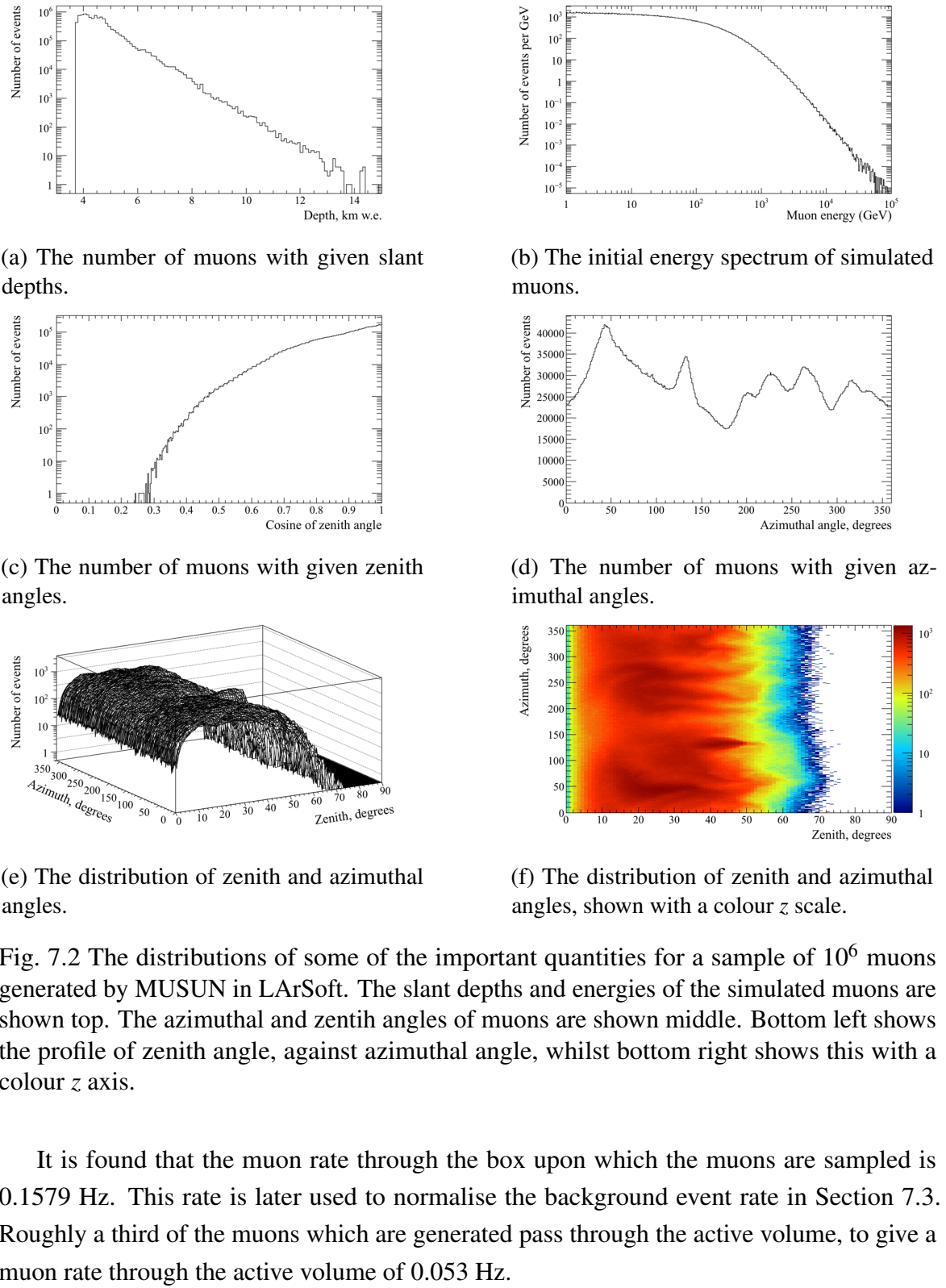


Fig. 7.1 The correlation between the surface profile and distribution of azimuthal angles at the DUNE far detector site. The quadrants have been divided into four angles of equal size. The azimuthal angle, calculated as the angle from East (pointing to the right in Fig. 7.1a), and increasing counterclockwise, is seen to follow the contours of the surface profile.

1 are sampled from is $74.43 \times 29.54 \times 30.18 \text{ m}^3$, compared to the simulated cryostat which
 2 has dimensions, $61.62 \times 14.94 \times 13.58 \text{ m}^3$. The dimensions are given as length \times width \times
 3 height. The muons are sampled randomly according to their energy spectrum, for a given
 4 zenith and azimuthal angle, using the angular distribution obtained with MUSIC.

5
 6 Before this could be done however, MUSUN had to be incorporated into the DUNE
 7 software framework, as it had previously been maintained in FORTRAN as an external
 8 package. This involved building on the work done by the LZ collaboration in porting the
 9 code to C++ !!!!citepKareem. The process by which this was done, was to first reproduce the
 10 distributions produced by the LZ collaboration using the DUNE software framework. Once
 11 the distributions could be reproduced for the Davis shaft at SURF, the muon distributions
 12 produced by the original FORTRAN code for the DUNE detector location were reproduced.
 13 The distributions produced by the DUNE software framework are shown in Figure 7.2. These
 14 are seen to be consistent with the distributions made for the LBNE collaboration [42]. The
 15 initial positions of 10,000 muons generated in LArSoft around the simulated DUNE 10 kt
 16 module are shown in Figure 7.3. The initial positions of the muons are shown as blue points,
 17 whilst the cryostat is a single black box, and each TPC is a single red box.

7.2 The use of MUSUN in LArSoft



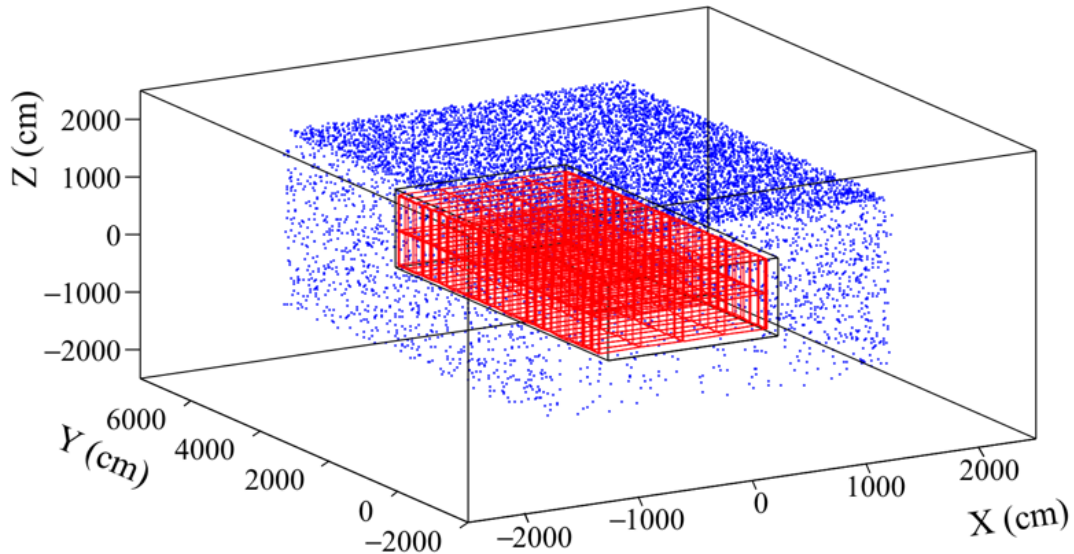


Fig. 7.3 The initial positions of muons generated by MUSUN around a DUNE 10 kt module. The initial positions of the muons are shown as blue points, whilst the cryostat is a single black box and each TPC is a single red box.

¹ 7.3 Nucleon decay channels in DUNE

² When searching for rare processes, where an experiment is unlikely to see more than a few
³ real signatures, an exhaustive study of the potential backgrounds is required. This is so
⁴ that if a signal is observed, it could provide overwhelming evidence for the process. The
⁵ search for nucleon decay in DUNE is one such process, and so an exhaustive study of the
⁶ background to nucleon decay is required. As discussed in Section 3.3.3, cosmogenic muons
⁷ cause backgrounds to nucleon decay signatures, as the secondary particles produced by their
⁸ interactions are able to mimic the nucleon decay signatures. For this reason it is necessary
⁹ to simulate this background, and to develop a series of cuts which can be applied to the
¹⁰ energy depositions they produce, to establish that they are not due to nucleon decays. When
¹¹ doing this, it is important to use a simulation that is as accurate as possible to the DUNE
¹² far detector. It is for this reason that MUSUN was incorporated into LArSoft, as the muons
¹³ which it generates are well matched to the observed muon flux, as described in Section 7.2.
¹⁴

¹⁵ To ensure that the background has been properly simulated it is advantageous to simulate
¹⁶ many more background events than will be collected by the experiment. As the DUNE
¹⁷ detector will run for roughly 20 years, it was decided that an initial sample representing 200

years of detector live time would be simulated. Given that the muon rate through the cavern is 0.1579 Hz, 200 years of detector live time corresponds to roughly 10^9 muons. This only represents one of the DUNE 10 kt modules, and so an even larger dataset will be required to represent the full live time of the 4 10 kt modules. For this reason, muons were generated beyond this initial sample size, with a total of $2/times10^9$ muons having been simulated currently.

Producing samples of this size requires significant computer power, both in terms of running time, and storage space. As such, many of the simulated events are discarded before being saved to disk, through the application of a filter after GEANT4. It is essential that the events which are discarded could not have been mistaken for nucleon decay events, and so only very generous cuts are applied. Only events satisfying one of the following cuts are discarded;

- Contain a muon track of more than 1 m.
- There are no energy depositions in the entire detector volume.

It is envisioned that a muon track of more than a metre would not be misreconstructed. It is also assumed that any signatures observed within one drift window of such a track would not be studied in a nucleon decay search, as there would be doubt as to the authenticity of the signal. Given that the total rate of muons through the active volume is 0.053 Hz, and that the drift time is a few ms, ignoring all times where any track from a cosmogenic muon is present results in less than 0.1% dead time. The dead time associated with ignoring events with muon tracks of more than 1 m is clearly less than this. This amount of dead time is assumed to be acceptable.

After applying this series of cuts, the sample of $2/times10^9$ muons is reduced to $XXXX \times 10^{XXXX}$ muons, which is a much more reasonable sample size to store on tape, and to perform analyses on. It is upon this reduced sample of muons that the cosmogenic background analyses are performed. As discussed in Section 3.3.2, the proton decay channel of $p \rightarrow K^+ + \nu e$ is referred to as the 'Golden Channel' in LAr, this analysis is discussed in [41]. The related decay of channel of $n \rightarrow K^+ + e^-$ is discussed here.

7.3.1 Cosmogenic background to the $n \rightarrow K^+ + e^-$ decay channel

As shown in Table 3.1, the predicted sensitivity that DUNE will have to this channel is much larger than that of Super-K. As a result, it is an interesting decay mode to study as DUNE

1 could easily have the best limit for this decay channel. As discussed in Section 3.3.3, the
2 cosmogenic background to nucleon decay is predominantly caused by neutral particles, such
3 as K^0 , entering the detector volume, and interacting far away from the detector edges. This
4 is particularly true for the 'Golden Channel,' as shown in Figure 3.1, but it also holds for
5 other channels. This means that it is events such as this which are the main cause for concern
6 when trying to eliminate all cosmogenic backgrounds.

7

8 As is the case with the 'Golden Channel,' the final state of the decay contains a single
9 charged kaon, and so events which do not contain a kaon track can be immediately discounted.
10 There is also an electron in the final state of the decay, and so this means that events which
11 do not also contain an electron can be discounted. In a nucleon decay event, the kaon and
12 electron produced in the final state will have a common vertex, and so the requirement that
13 the two particles have a common vertex can also be applied. Other constraints that are applied
14 to eliminate background events are; a cut on external muon length, a cut on depositions near
15 the detector edges, and criteria about the distribution of deposited energy. The criteria about
16 the distribution of deposited energy is found by considering a sample of simulated decay
17 events, and is discussed in Section 7.3.3. These cuts, which are applied sequentially, are
18 outlined below:

- 19 • The event contains energy depositions due to kaons and due to electrons.
- 20 • The event contains at least one kaon track, and at least one electron track/shower.
- 21 • The event contains a single kaon track, and a single electron track/shower.
- 22 • No muon travels more than 20 cm in the detector volume.
- 23 • The event has no energy depositions within 2 cm of the detector edges.
 - 24 – This is changed to a maximum of 100 MeV of energy deposited within 2 cm of
25 the detector edge in Section 7.3.2.
- 26 • The kaon and electron share a common vertex.
 - 27 – The kaon and electron tracks are separated by no more than 5 cm.
 - 28 – If the kaon and electron tracks are separated by more than 5 cm, then the point of
29 closest approach between the two extrapolated tracks is less than 2 cm.
- 30 • The energy depositions in the event are within the ranges expected from a nucleon
31 decay event. This is explained in Section 7.3.3, but the energies considered are
32 summarised below:

- The energy directly deposited by the kaon. 1
- The energy deposited by the kaon decay products. 2
- The energy directly deposited by the electron. 3
- The energy deposited near the shared kaon and electron vertex 4
- The energy deposited in the detector which does not fit any of the above criteria. 5

Inspiration for these cuts were taken from [43], though some of the cuts were relaxed. The cut on muons was relaxed from a cut on any muon being present, to a maximum track length of 20 cm, as this was found to be sufficient. The cuts on the number of pions in the event were relaxed so as to not expect that all particles are perfectly reconstructed. However, as the analysis is performed using Monte Carlo truth information, without position or energy smearing, the kaons and electrons are assumed to be perfectly reconstructed. This means that it is assumed that all deposited charge will be reconstructed, and that the detector characterisation is perfect. This is something which will need to be refined in future analyses, and will be taken into account when the analysis progresses to use reconstructed quantities, as discussed in Section 7.3.4.

When performing the analysis it is important to be able to trace the particle ancestry. This is so that energy depositions in the detector can be properly assigned, and cuts applied, to the relevant particles. For example, a μ^+ is often produced when a K^+ decays at rest, and this muon may travel more than 20 cm. However, the cut on muon length should not be applied to this muon as it was produced by the decay of the kaon. Similarly, as the kaon interacts in the detector secondary particles will be produced, which will be reconstructed as tracks coming off the main kaon track. The initial kinetic energy of the kaon can then be determined by summing the energy depositions due to these secondary particles, and the energy depositions due to the kaon itself. Correctly calculating the initial kaon kinetic energy is critical when determining if an event is a nucleon decay event. The reason for this is that nucleon decay events have very specific energy spectra, and so being able to correctly assign the ancestry of energy depositions is vitally important. The same is true for the electron energy, which is calculated by tracing the ancestry of the particles in the shower back to the electron which initiated the shower.

As no reconstruction has been performed, the tracks referred to here are different from those in previous sections. The definition of a track used here, is that the particle in question has energy depositions, on simulated wires, which are directly associated with it. These simulated wires are not the same as the the wires which have been considered in previous

¹ Monte Carlo studies, as the signals have not been digitized. This distinction is important, as
² it allows the energy depositions directly from GEANT4 to be used, whilst also allowing for
³ LArSoft methods concerning whether depositions are within TPC boundaries to be utilised.

⁴

⁵ The simulated electrons may begin showering immediately, or they may produce a short
⁶ 'track like' segment before beginning to shower. To ensure that every electron shower can
⁷ be identified, electrons are not required to produce a short 'track like' segment. This means
⁸ that all electrons are assumed to begin showering immediately, and it is also assumed that all
⁹ of the energy in the shower can be identified as coming from a single initial electron. This
¹⁰ definition of shower energy is used as it is the one that is used when the showering algorithms
¹¹ are developed in LArSoft. It is hoped that when DUNE begins taking data the showering
¹² algorithms will be able to achieve this level of energy reconstruction.

¹³

¹⁴ When calculating the distance between the start of the kaon track, and the start of the
¹⁵ electron track/shower, the energy depositions whose locations are closest to the Monte Carlo
¹⁶ truth start points of the particles, are used. For particles which are produced within the active
¹⁷ volume, these locations generally correspond to the Monte Carlo truth start positions, though
¹⁸ this is not always the case. For example, if a particle is created in the gap between two TPCs,
¹⁹ then there will be no charge collected until it enters the active volume. This will result in
²⁰ the measured start position to be shifted from the true generation point. This shift can prove
²¹ troublesome when considering decay events, as if the decay occurred in the centre of an APA,
²² then it is likely that the kaon and electron would deposit energy on opposite sides of the
²³ APA. This would cause the depositions to be separated by over 5 cm, as this is the width of
²⁴ the APAs. However, if the tracks are propagated backwards, towards their true start point,
²⁵ it should still be possible to determine that they had a common vertex. An example of a
²⁶ simulated decay event where this happens is shown in Figure 7.4.

²⁷

²⁸ In the determination of whether a kaon track and an electron shower share a common
²⁹ vertex, the first requirement which is applied is whether the distance between the starts of the
³⁰ kaon track, and the electron shower, are separated by less than 5 cm. A maximum separation
³¹ of 5 cm is used, as, if the two particles are produced in the centre of a TPC, a gap of 5 cm
³² would require no energy depositions to be collected over approximately 10 collection wires.
³³ This is assumed to be unlikely during data taking, and cannot happen in the simulations
³⁴ considered here, as Monte Carlo truth information is used. As shown by Figure 7.4 however,
³⁵ it is possible for the kaon and electron to be separated by more than 5 cm in signal events.
³⁶ To prevent events such as this being missed, a second criteria is applied to events with large

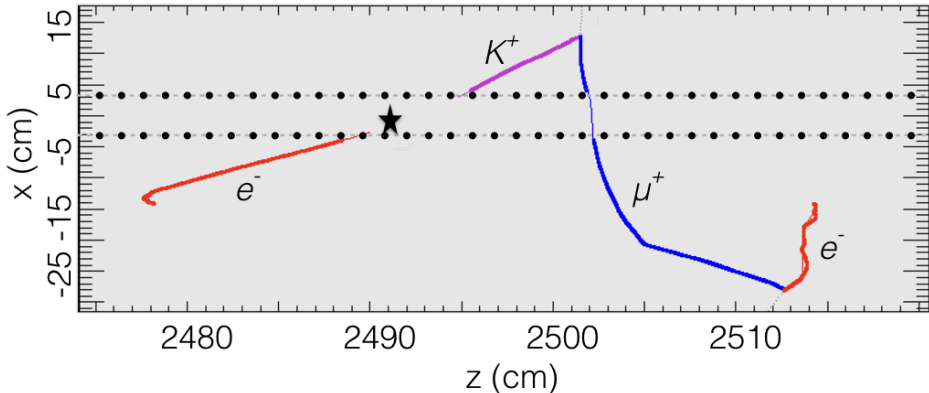


Fig. 7.4 A simulated $n \rightarrow K^+ + e^-$ decay which occurred in a gap between TPCs. The path which the kaon produced in the decay took is shown as a purple line. The path which the muon produced by the decay of the kaon is shown as a blue line. The paths which the electrons in the event took are shown as red lines, the electron on the left is the electron produced in the neutron decay, whilst the one on the right is produced by the decay of the muon. The thin coloured lines, show track segments which were in uninstrumented parts of the detector, such as gaps between TPCs and APAs. The dotted black lines shows the gap between the TPCs, and the black star shows the location at which the decay occurred. The distance between the first kaon energy deposition and the first electron energy deposition is found to be 10.7 cm. However, when the kaon and electrons tracks are extrapolated towards the true start position, the point of closest approach (PoCA) between the two tracks is found to be 0.67 cm, showing that they do in fact have a common vertex, despite the separation of the start points.

separations. Both the kaon and electron tracks, are extrapolated from their start and end points, and the minimum separation of these extrapolated tracks is calculated. This is known as calculating the “Point of Closest Approach” (PoCA) between the two tracks, and if this PoCA is less than 2 cm, then the tracks are considered to have a common vertex which was missed.

When performing the fiducial cut, it is only applied to the outer edges of the cryostat, as if it were done with respect to the edge of every TPC in the far detector the loss of volume would be prohibitive. This means that the event shown in Figure 7.5 would not fail the fiducial cut, as the decay occurred over 6 m away from the edge of the detector, but happened to be in a gap between two TPCs. The need for a fiducial cut is two fold, firstly the vast majority of cosmically induced events in the detector will have a charged particle, which was produced externally, entering the detector. Performing a fiducial cut will remove all of these events, and will then mean that the only cosmic background events which can induce a signal would involve either a significant amount of charge being missed, or a neutral

¹ particle entering the detector, and interacting far from the detector wall. Secondly, in order
² to calculate the kinetic energies of the particles produced in the nucleon decay, and also to
³ perform particle identification, they must be fully contained within the detector. As such,
⁴ if one of the particles produced in the nucleon decay escapes the detector then it's kinetic
⁵ energy cannot be determined accurately, and if it is the kaon, or its decay products, then the
⁶ particle cannot be identified using the method discussed in Section 5.4. A fiducial cut of
⁷ 2 cm is used, as the loss of volume is negligible in a detector which is scale of the DUNE
⁸ FD, whilst also ensuring that a significant amount of charge would have to be missed for
⁹ a particle which enters/escapes the detector to be incorrectly identified as being contained
¹⁰ within the detector.

11

¹² Once both the ancestry of energy depositions in the simulation, and the initial kinetic
¹³ energies, have been correctly accounted for and calculated, it is possible to observe the distri-
¹⁴ bution of background events, as the cuts outlined above are applied. The energy distribution
¹⁵ of background events surviving the application of sequential cuts is shown in Figure 7.5. The
¹⁶ normalised energy distribution of background events surviving the application of sequential
¹⁷ cuts is shown in Figure 7.6. The distribution of normalised energies is found by dividing the
¹⁸ number of events by the bin energy.

19

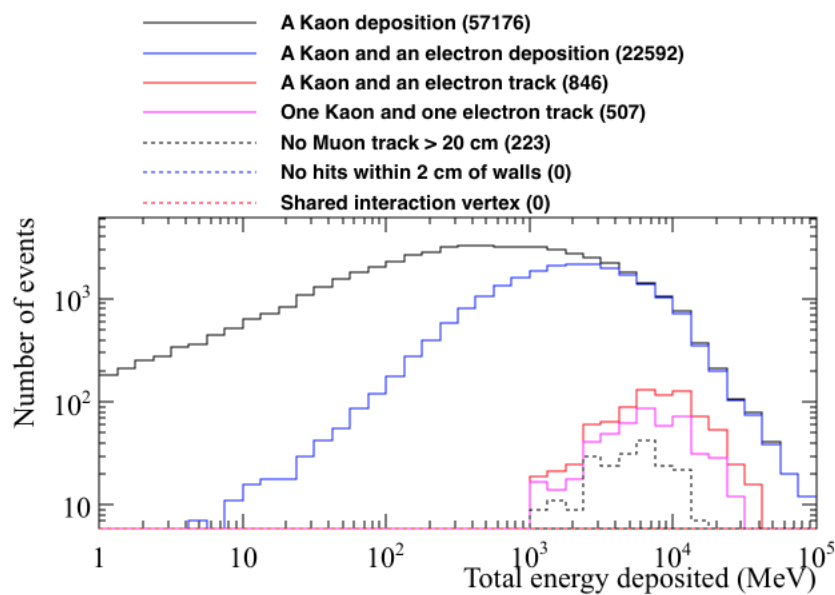


Fig. 7.5 The energy distribution of background events surviving the application of sequential cuts in the $n \rightarrow K^+ + e^-$ channel. The total energy deposited in the detector is plotted on the x axis.

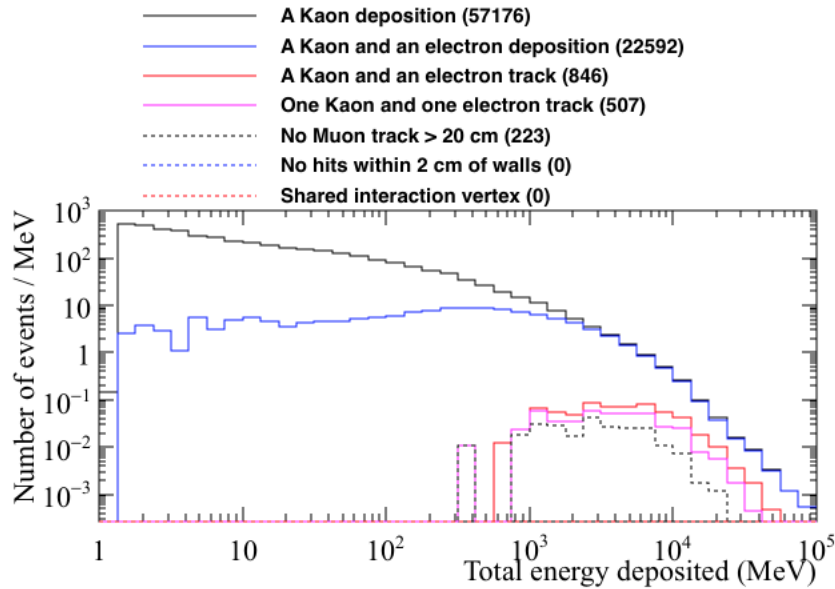


Fig. 7.6 The normalised energy distribution of background events surviving the application of sequential cuts in the $n \rightarrow K^+ + e^-$ channel. The total energy deposited in the detector is plotted on the x axis. The normalised energy distribution has been found by dividing the number of events within a bin by the bin energy.

From Figures 7.5 and 7.6, it can be seen that there are no background events which could mimic a decay signature as there are no events which survive the application of all cuts. This corresponds to a limit on the cosmogenic background to the $n \rightarrow K^+ + e^-$ decay channel of $XX \times 10^X X$.

It is interesting however, to observe the effect that relaxing the cuts after the presence of at least one kaon track and at least one electrons shower in the event has been confirmed. This allows for the effectiveness of each of the cuts to be observed. Initially, the four cuts which are applied after kaon tracks, and electron showers, have been identified, are applied in isolation. The number of events surviving each of the cuts is shown in Table 7.2.

The effectiveness of the fiducial cut is clearly apparent from Table 7.2, as it removes all 845 events where there is both a kaon track and an electron shower. It is for this reason that the loss in fiducial volume that it causes is accepted. The requirement made on the proximity of the kaon track and electron shower is also seen to be very effective at removing background events. It is found that of the 507 events that have a single kaon track, and a single electron shower, in only 41 of them would the kaon and electron be considered to have a common vertex. When the additional constraint of there not being a muon with a track

Table 7.2 The number of events surviving isolated cuts which could mimic a $n \rightarrow K^+ + e^-$ decay. Cuts are applied after it is found that the event contains at least one kaon track, and at least one electron shower present. This is found to be true for 845 events, representing the top line of the table. The fiducial cut of 2 cm is seen to remove all of the events considered.

Cut that is applied	Num. events survivng isolated cut
At least one kaon track, and electron shower	845
Only one kaon track, and only one electron shower	507
No muon track that is longer than 20 cm in length	339
No energy depositions within 2 cm of detector edge	0
The kaon and electron share a common vertex	85

¹ length of more than 20 cm present in the event is applied, only 11 events would survive the
² cuts. This shows that the only way to remove all potential background events is to apply the
³ fiducial cut, or to make the some of the other criteria stricter, such as reducing the seperation
⁴ of the kaon track and the electron shower which constitutes a common vertex.

⁵

⁶ 7.3.2 Signal events in the $n \rightarrow K^+ + e^-$ decay channel

⁷ It is important to confirm that the cuts developed do not adversely affect the identification
⁸ of true nucleon decay events. For this reason a sample of 10,000 neutron decay events
⁹ in the DUNE far detector were generated using GENIE. Neutron decays are generated at
¹⁰ random positions within the detector volume, and so it is possible that the decay occurs in
¹¹ between TPC volumes, as shown in Figure 7.4, or near the edge of the detector, as is shown
¹² in Figure 7.7.

¹³

¹⁴ The analysis performed on the cosmogenic background was primarily designed to reject
¹⁵ background events, whilst also attempting to not use cuts which would also affect signal
¹⁶ efficiency. Therefore, it is hoped that the loss of signal events will be minimal. When running
¹⁷ the analysis on the simulated signal events the same definitions for tracks, showers, and
¹⁸ the ancestry of particles are used, as well as the same cuts that were outlined in Section 7.3.1.

¹⁹

²⁰ The energy distribution of the signal events survivng the application of the sequential cuts
²¹ is shown in Figure 7.8, this is the equivalent of Figure 7.5 for the cosmogenic background
²² sample. The normalised energy distribution of signal events surviving the application of
²³ sequential cuts is shown in Figure 7.9, this is the equivalent of Figure 7.6 for the cosmogenic
²⁴ background sample. As before, the distribution of normalised energies is found by dividing

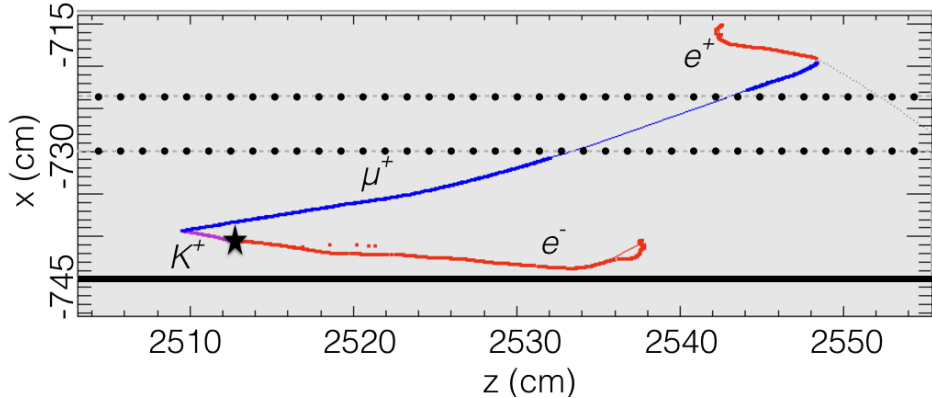


Fig. 7.7 A simulated $n \rightarrow K^+ + e^-$ decay which occurred near the edge of the detector volume. The path which the kaon produced in the decay took is shown as a purple line. The path which the muon produced by the decay of the kaon is shown as a blue line. The paths which the electrons in the event took are shown as red lines, the electron on the left is the electron produced in the neutron decay, whilst the one on the right is produced by the decay of the muon. The thin coloured lines, show track segments which were in uninstrumented parts of the detector, such as gaps between TPCs and APAs. The dotted black lines shows the gap between the TPCs, and the solid black line shows the edge of the detector. The black star shows the location at which the decay occurred. It can be seen that though the event is contained within the detector it is very close to the edge of the detector due to the location at which the decay occurred.

the number of events by the bin energy.

When comparing Figures 7.8 and 7.9 with Figures 7.5 and 7.6, the most obvious difference is that when considering the nucleon decay events, the total energy deposited in the detector never exceeds 1 GeV, whilst in the cosmogenic background sample, the energy deposited in the detector frequently exceeds 1 GeV. This is something which one would expect, as the simulated neutrons decay at rest and so have a total energy of less than 1 GeV, meaning that there cannot be more than 1 GeV deposited in the detector. This is in stark contrast to the cosmogenic background, where the primary muons being generated have a mean energy of 283 GeV, as shown in Table 7.1. This means that many events will deposit significant amounts of energy in the detector, even if the primary muon narrowly misses the detector volume.

The initial cuts, requiring that both a kaon track and an electron shower are observed in the decay, show that there are occasions when either the kaon, or the electron, do not deposit energy in the detector. This affects very few events, though an example of one such event is shown in Figure 7.10, where it can be seen that the kaon decayed before entering the

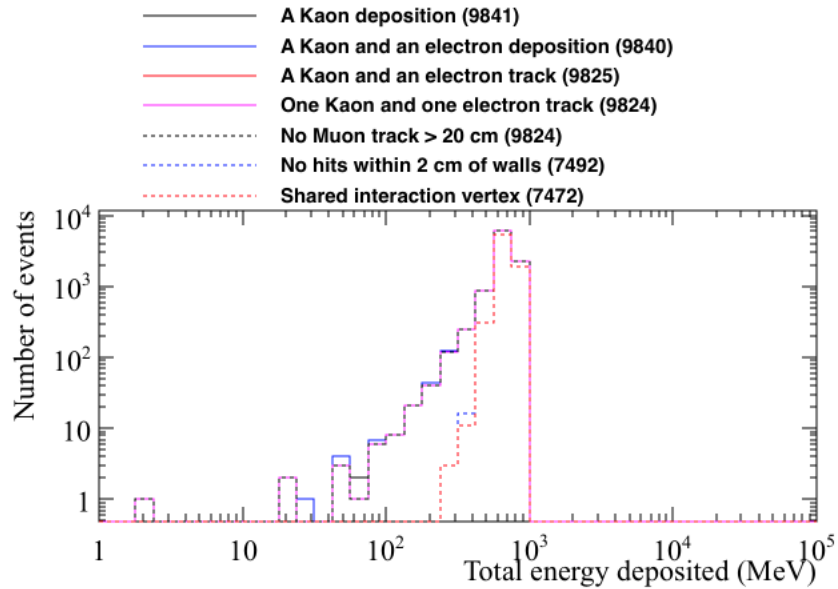


Fig. 7.8 The energy distribution of signal events surviving the application of sequential cuts in the $n \rightarrow K^+ + e^-$ channel. The total energy deposited in the detector is plotted on the x axis.

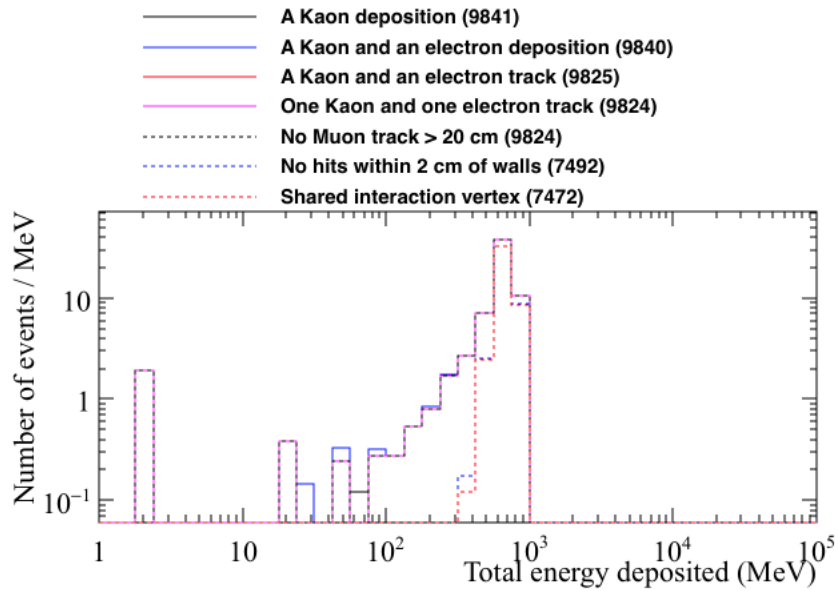


Fig. 7.9 The normalised energy distribution of signal events surviving the application of sequential cuts in the $n \rightarrow K^+ + e^-$ channel. The total energy deposited in the detector is plotted on the x axis. The normalised energy distribution has been found by dividing the number of events within a bin by the bin energy.

active volume, and so no track was found for it. It would be very difficult to identify this event as a signal event, as the presence of the kaon could only be inferred from the muon originating from the gap between the APAs, and the energy deposited by the kaon will not be reconstructed. Further compounding the identification of this event as a signal event, is the fact that the electron produced in the nucleon decay scatters back into the gap between the APAs, and so a significant amount of its energy would not be reconstructed.

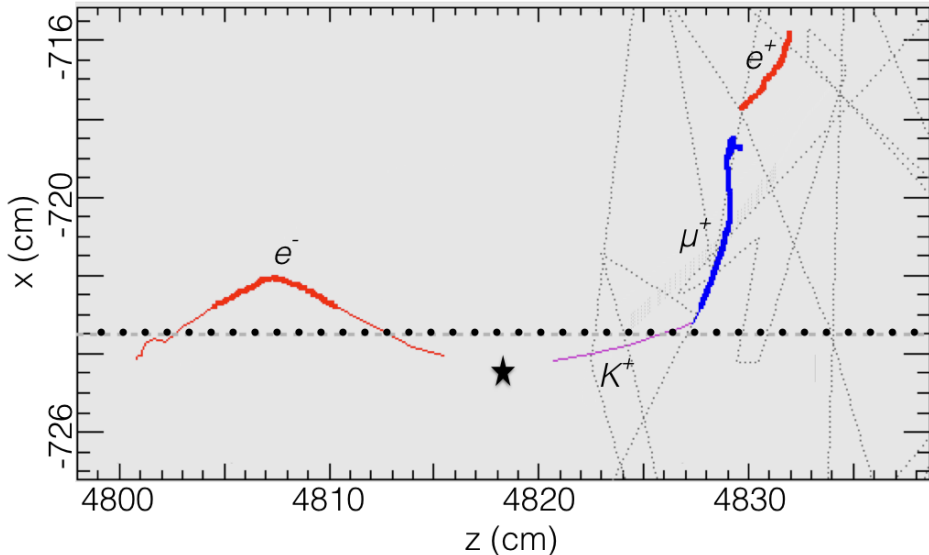


Fig. 7.10 A simulated $n \rightarrow K^+ + e^-$ decay where the kaon did not deposit any energy in the active volume. The path which the kaon produced in the decay took is shown as a purple line. The path which the muon produced by the decay of the kaon is shown as a blue line. The paths which the electrons in the event took are shown as red lines, the electron on the left is the electron produced in the neutron decay, whilst the one on the right is produced by the decay of the muon. The thin coloured lines, show track segments which were in uninstrumented parts of the detector, such as gaps between TPCs and APAs. The dotted black lines shows the gap between the TPCs, and the solid black line shows the edge of the detector. The black star shows the location at which the decay occurred. It can be seen that the kaon decayed before it entered the active volume of the detector, and so no track was found for it. A significant portion of the distance which the electron from the decay travelled was also outside the active volume of the detector.

The number of events which are removed by the fiducial cut is concerning, as almost 20% of events are removed due to it. This suggests that the cut is too strict. The reason for this, is that protons and neutrons are emitted from the nucleus in many of the simulated decays, and whilst the protons produced will create relatively short tracks, which are connected to the decay vertex, the neutrons will travel large distances, and cause energy depositions

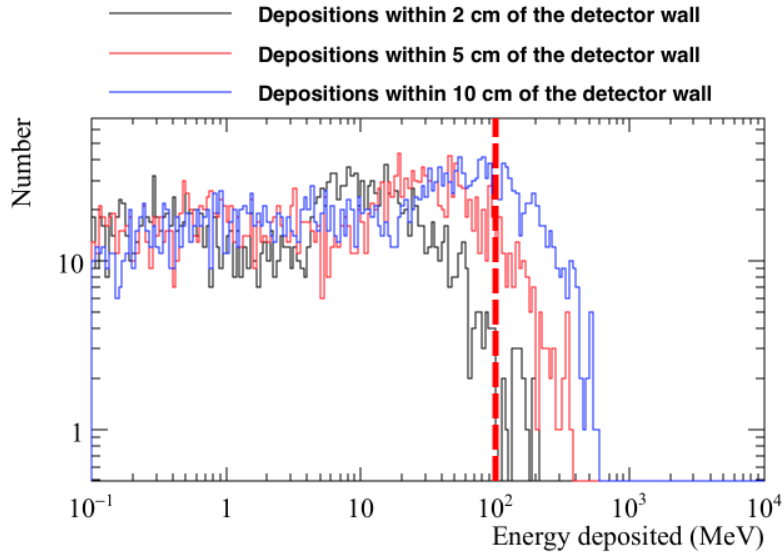
1 which are far away from the decay vertex. The faint dashed lines in Figure 7.10 show the
2 spallation neutrons produced in the decay. It is predominantly the energy depositions from
3 these spallation neutrons which are causing events to fail the “no energy depositions within 2
4 cm of the detector edge” cut. As a result it is likely that this cut needs to be relaxed, to instead
5 be a cut on the amount of energy deposited within 2 cm of the detector edge. Figure 7.11
6 shows the amount of energy deposited within 2 cm, 5 cm, and 10 cm of the detector edges,
7 for the simulated nucleon decay events, and the cosmogenic background events.

8

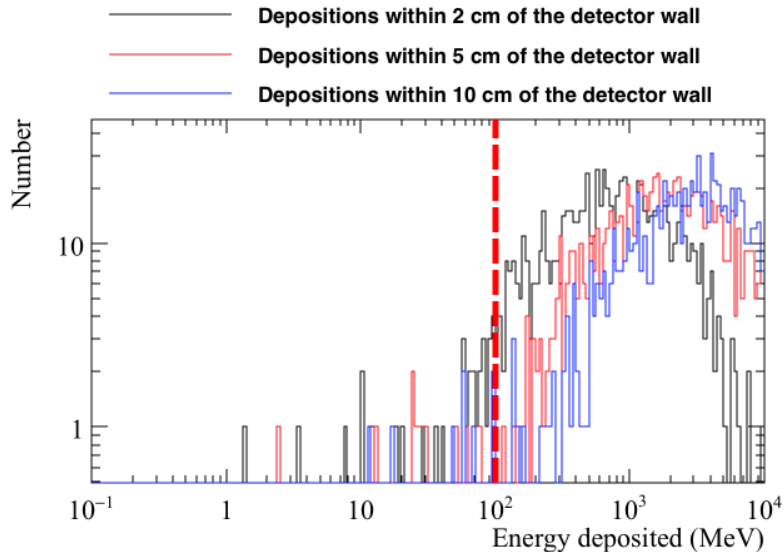
9 As can be seen from Figure 7.11, the amount of energy deposited near the detector edges
10 is very different in the nucleon decay and cosmogenic background events. As such, they can
11 be cleanly separated, and so a very conservative cut, requiring no more than 100 MeV of
12 energy to be deposited within 2 cm of the detector edge, can be used. There are very few entries
13 in the figure for the simulated neutron decay events, because, as shown in Figures ?? and ??,
14 there are 7492 events for which there are no depositions within 2 cm of the detector edge.
15 Requiring that there be no more than 100 MeV of energy deposited within 2 cm of the detector
16 edges, removes only 19 of the 9824 signal events, whilst only 18 out of the 223 cosmic
17 background events meet this requirement. Whilst this does mean that the fiducial cut is no
18 longer as effective at removing the cosmic background sample, it does not cause the huge
19 loss of signal events which was seen when the hard cut, of no energy depositions within 2 cm
20 of the detector edge, was used. It is also important to remember that the requirement that the
21 kaon and electron share a common vertex, as well as cuts on the energy deposition profiles,
22 will still be applied to these 18 background events. It will be seen in Section 7.3.3, that no
23 events survive the application of these cuts.

24

25 The definition used to decide if the start of the kaon track, and the start of the electron
26 shower, share a common vertex seems to be a reasonable requirement, as almost all of the
27 signal events satisfy this definition. The distance between the start of the kaon track, and
28 the start of the electron shower is shown in Figure 7.12. It can be seen that the separation
29 between the two particles is very small (<0.1 cm) in most events. However, there are some
30 events where the separations are very large (>10 cm). As discussed earlier, the decays in
31 these events occur in the gaps between TPCs, such as that shown in Figure 7.4. When the
32 requirement that the kaon and electron track have a PoCA of less than 2 cm is then applied to
33 these events, most of them are then shown to have a common interaction vertex. This is found
34 to be the case for the event shown in Figure 7.4. However, in some events the kaon track, and
35 the electron shower, are still found to not have a common interaction vertex. Handscanning
36 of these events shows that particles undergo scattering before entering the active volume, and



(a) The nucleon decay events.



(b) The cosmogenic background events.

Fig. 7.11 The number of events, as a function of the energy deposited within 2 cm, 5 cm, and 10 cm of the detector edges. Top shows the energies which were deposited for the simulated neutron decay events. Bottom shows the energies which were deposited in the simulated cosmogenic background events. The histograms are filled after the cut requiring that there is no muon with a track length of greater than 20 cm in the detector is applied. As such, the histograms are filled with 9824 and 223 events for the top and bottom histograms respectively. The dashed red line shows a preliminary cut on the energy deposited of 100 MeV.

7.3 Nucleon decay channels in DUNE

120

- ¹ so by the time the energy depositions are collected, their trajectories are no longer closely
² aligned, causing them to have large values for the PoCA which is calculated.

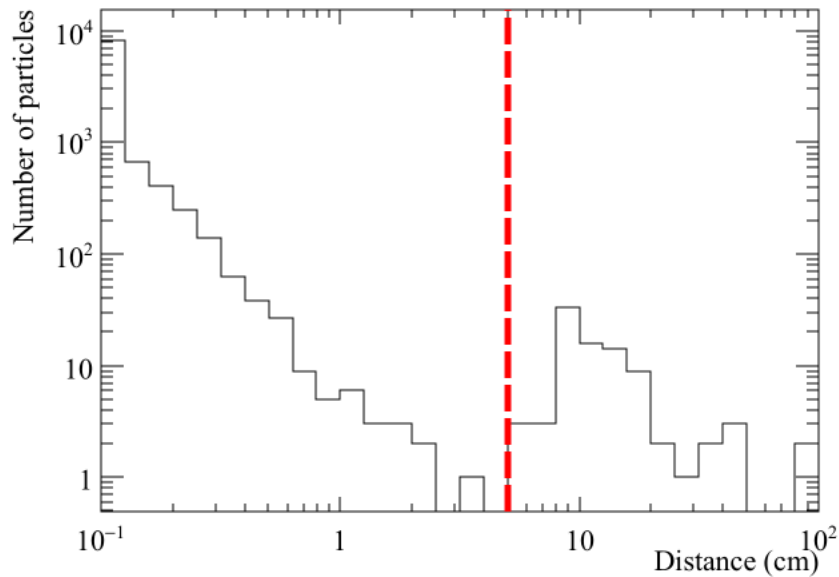
³

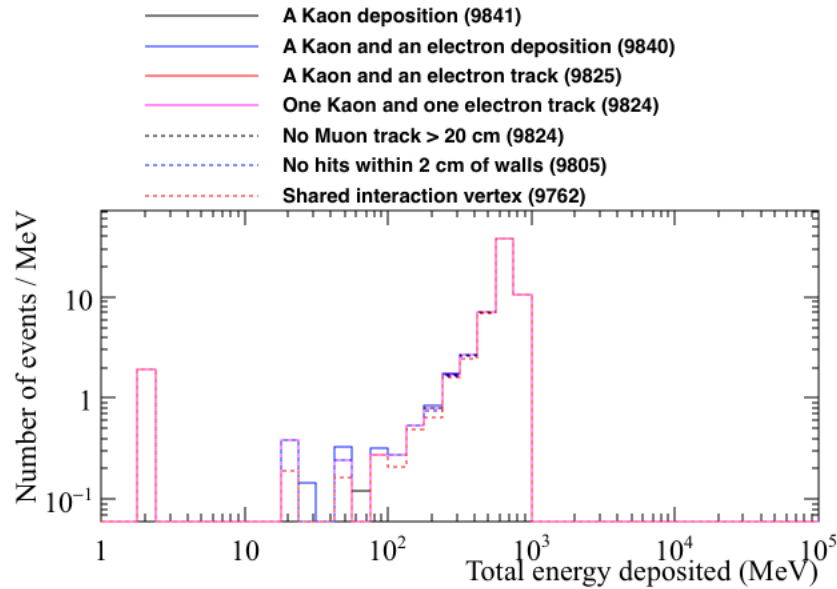
Fig. 7.12 The separation of the kaon and the electron produced in the $n \rightarrow K^+ + e^-$ decay channel. The dashed red line, drawn at a separation of 5 cm, shows the maximum possible separation a kaon and an electron could have, and still be considered to have a common vertex.

- ⁴ The normalised energy distributions of simulated decay events, and simulated cosmogenic background events, after the fiducial cut is changed to be a limit of 100 MeV of
⁵ energy deposited within 2 cm of the detector edge, is shown in Figure 7.13. As before, the
⁶ distribution of normalised energies is found by dividing the number of events by the bin
⁷ energy.
⁸

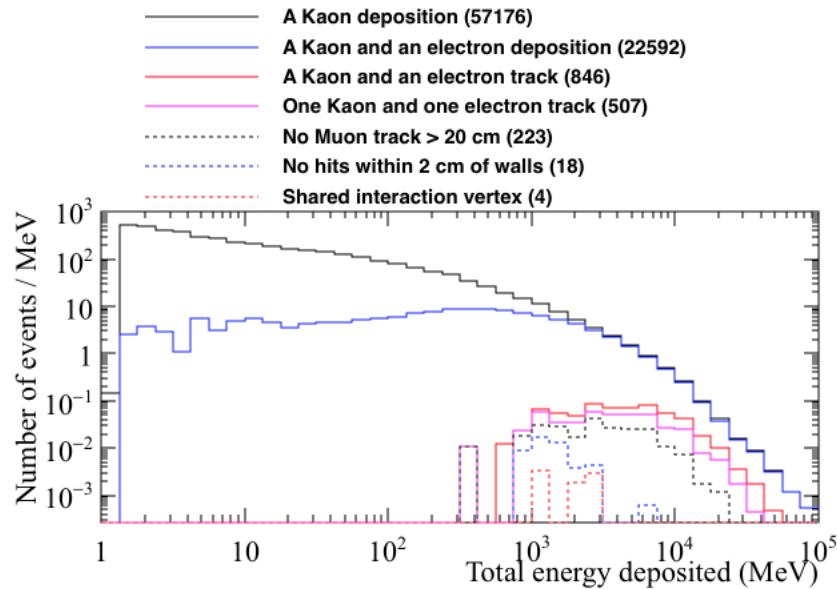
⁹

- ¹⁰ The number of signal events which are removed by the cuts can be seen to be much more
¹¹ reasonable after the fiducial cut is modified, as less than 2.5% of signal events are removed
¹² as cuts are applied. It is seen that in many of the simulated decay events which fail the cuts,
¹³ at least one of the kaon, or the electron, are not contained in the detector. This means that,
¹⁴ either no depositions are found for the particle, or it deposits significant amounts of energy
¹⁵ as it leaves the detector.

¹⁶



(a) The normalised energy distribution of signal events.



(b) The normalised energy distribution of cosmic background events.

Fig. 7.13 The normalised energy distribution of signal events, and cosmic background events, surviving the application of sequential cuts, after the fiducial cut is modified. The total energy deposited in the detector is plotted on the x axis. The normalised energy distribution has been found by dividing the number of events within a bin by the bin energy.

It can be seen that though 4 of the cosmic background events pass the application of all cuts, the total energy deposited in the detector is not less than 1 GeV in any of these

¹ events. This means that the total energy deposited in the detector is more than the rest mass
² of a neutron, and so the event is not consistent with being from the decay of a neutron at
³ rest. However, it is still prudent to determine the expected energy deposition distribution for
⁴ the signal events, to ensure that a clean separation can be observed between the signal and
⁵ background events.

⁶

⁷ 7.3.3 Energy constraints on the cosmogenic background to the $n \rightarrow$ ⁸ $K^+ + e^-$ decay channel

⁹ As outlined in Section 7.3.1, it is possible to exclude background events from signal events,
¹⁰ using the distribution of how energy is deposited in the detector. The energy criteria which
¹¹ were previously outlined were;

- ¹² • The energy directly deposited by the kaon.
- ¹³ • The energy deposited by the kaon decay products.
- ¹⁴ • The energy directly deposited by the electron.
- ¹⁵ • The energy deposited near the shared kaon and electron vertex
- ¹⁶ • The energy deposited in the detector which does not fit any of the above criteria.

¹⁷ Following the earlier discussions in Section 7.3, it should be clear that the energy directly
¹⁸ deposited by the kaon corresponds to the sum of all energy depositions which are due to the
¹⁹ kaon or its interaction products. Equivalently, the energy directly deposited by the electron
²⁰ corresponds to the sum of all energy depositions which are due to the electron as it showers,
²¹ and any particles created as a result of the shower. The energy deposited by the kaon decay
²² products, would include all depositions by the muon and subsequent electron, in the case that
²³ the kaon decayed via $k^+ \rightarrow \mu^+ + \nu_\mu$, and then the muon decayed via $\mu^+ \rightarrow e^+ + \nu_e + \nu_\mu$.
²⁴ The energy deposited near the shared kaon and electron vertex, would primarily consist of
²⁵ energy depositions due to spallation products. The depositions due to spallations products
²⁶ would largely be due to protons, though may also include some depositions due to the
²⁷ neutrons too, if they deposit energy near the vertex. Any depositions within 5 cm of the kaon
²⁸ and electron vertex are considered as 'near.' The final criteria, of any depositions which do
²⁹ not fit the above description, would largely consist of energy depositions due to the spallation
³⁰ neutrons in the decay sample. However, in the cosmic background sample, this would include
³¹ all depositions by muons, pions, and any other particles which enter the detector.

³²

In presenting the separation of simulated cosmic background events and simulated neutron decay events, the important distributions to consider are as follows:

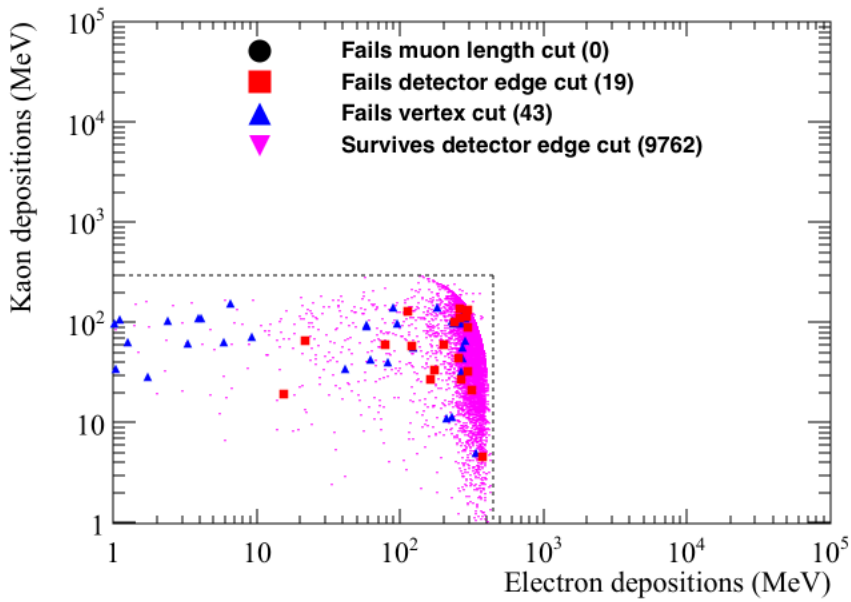
- The energy directly deposited by the kaon, against the energy directly deposited by the electron. This is shown in Figure 7.14.
- The energy directly deposited by the kaon, plus the energy directly deposited by the electron, against the energy deposited near the shared kaon and electron vertex. This is in Figure.
- The energy deposited by the kaon, including decay products, against the energy deposited in the detector which does not fit any of the other criteria. This is shown in Figure.
- The energy deposited by the kaon, including decay products, plus the energy directly deposited by the electron, plus the energy deposited near the shared kaon and electron vertex, against the energy deposited in the detector which does not fit any of the other criteria. This is shown in Figure.

Each will be discussed in turn below.

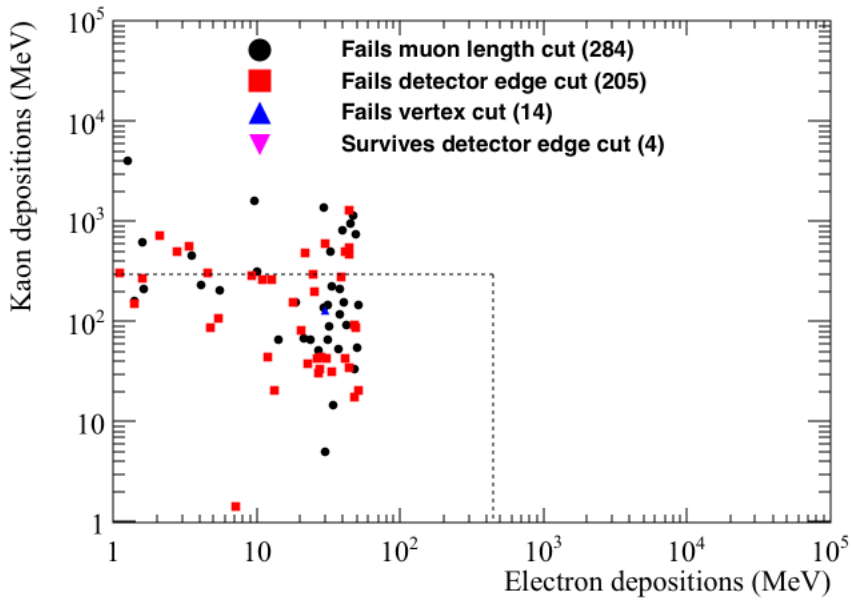
From Figure 7.14 it can be seen that the electron energy distribution in the cosmic background sample is very different from the one seen in the simulated neutron decay sample. This is shown by energies deposited by electrons in the decay sample being tightly concentrated between 200 and 400 MeV, whilst in the cosmic background sample, the energy deposited by the electron is always less than 50 MeV. Many of the electrons in the cosmic background sample deposit less than 1 MeV of energy in the detector, and so are not shown here. This is why the events where the kaon and electron share a common vertex are not shown in the cosmic background sample. Realistically, these electrons are unlikely to be reconstructed due to their extremely low energies. From Figure 7.14a, it can be seen some of the electrons produced in the nucleon decay events also deposit very little energy in the detector, though these events generally fail either the fiducial, or vertex, cuts. An explanation as to why these events fail the cuts was presented in Section 7.3.2.

Figure 7.15 shows.

Figure 7.16 shows.



(a) The energy distribution of signal events.

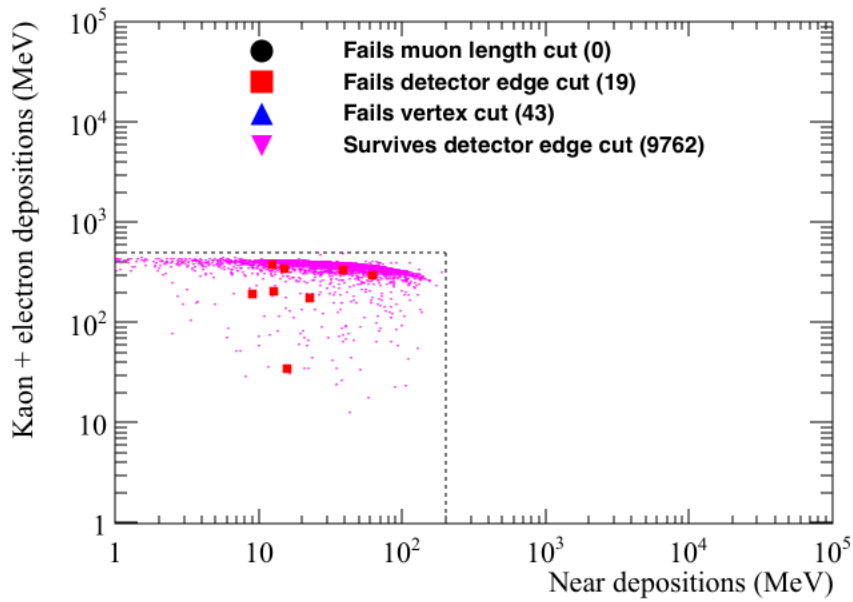


(b) The energy distribution of cosmic background events.

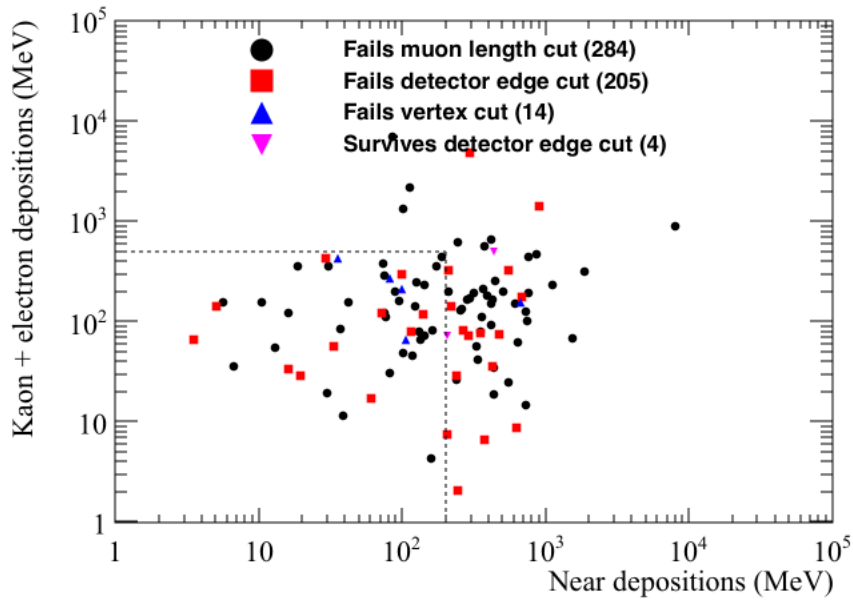
Fig. 7.14 The energy directly deposited by kaons, as a function of the energy directly deposited by electrons, in the simulated nucleon decay, and cosmic background samples. The events failing the application of the muon length (black circle), fiducial (red box) and vertex (blue triangle) cuts, as well as the events passing all cuts (pink triangle) are shown.

¹ Figure 7.17 shows.

²

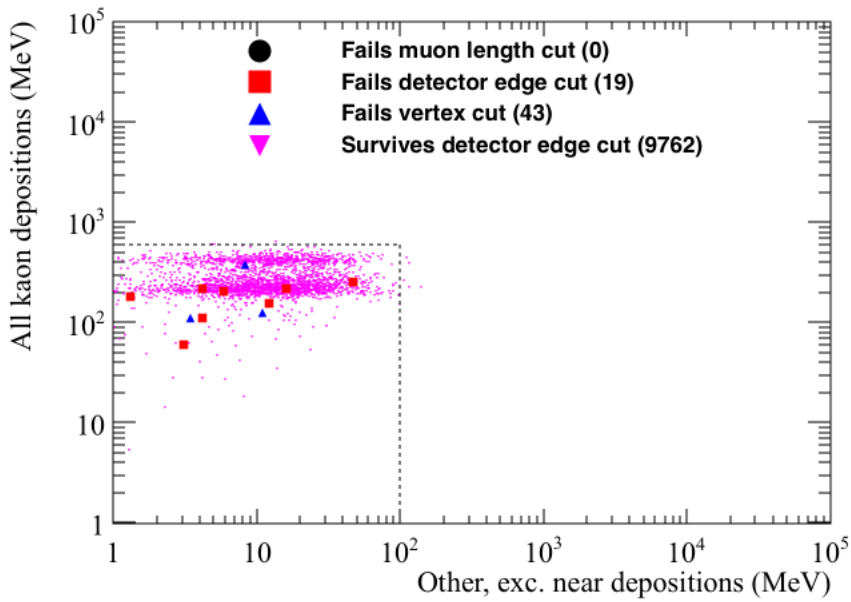


(a) The energy distribution of signal events.

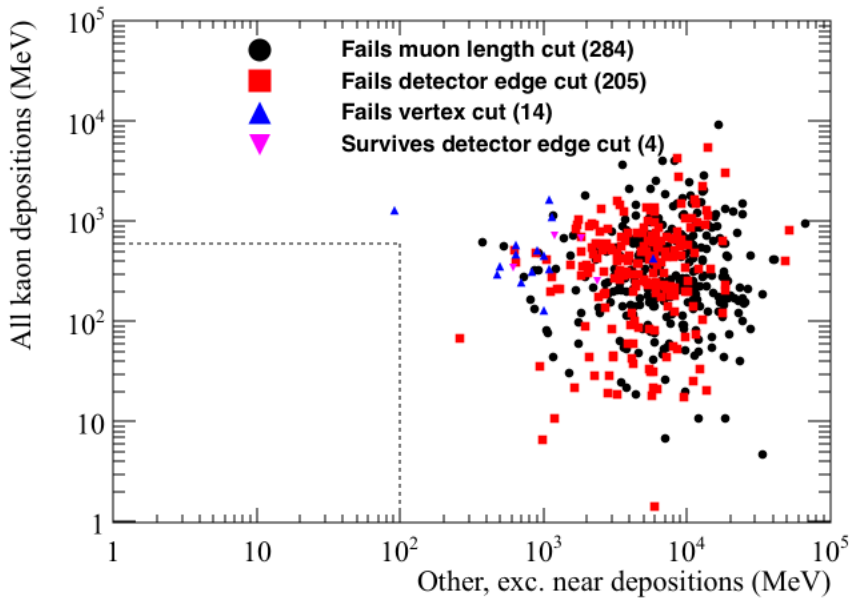


(b) The energy distribution of cosmic background events.

Fig. 7.15 The energy directly deposited by kaons, plus the energy directly deposited by electrons, as a function of the energy deposited near the kaon and electron vertex, in the simulated nucleon decay, and cosmic background samples. The events failing the application of the muon length (black circle), fiducial (red box) and vertex (blue triangle) cuts, as well as the events passing all cuts (pink triangle) are shown.

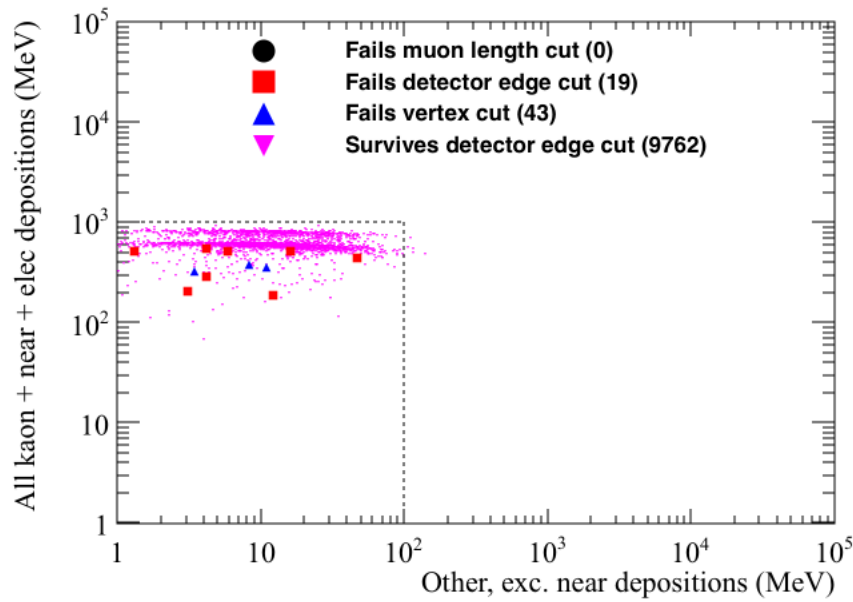


(a) The energy distribution of signal events.

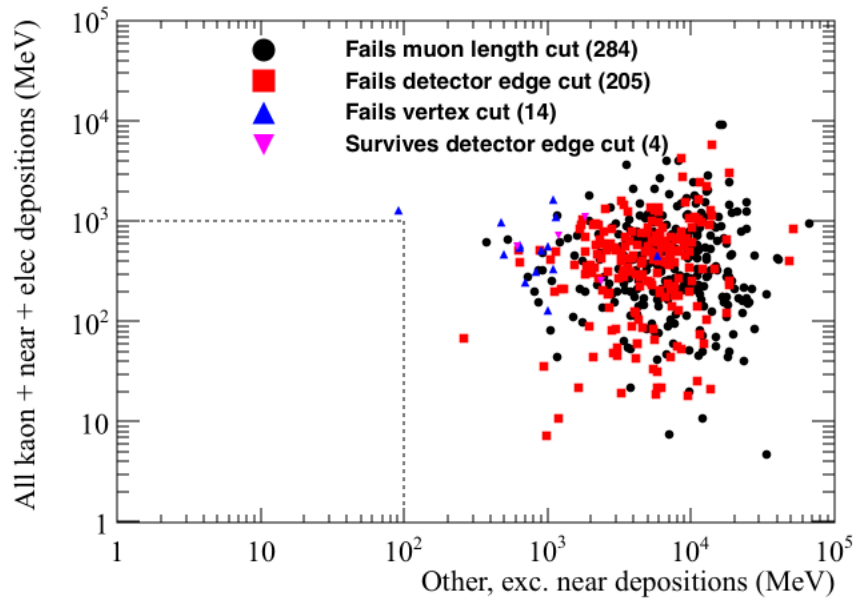


(b) The energy distribution of cosmic background events.

Fig. 7.16 The energy directly deposited by kaons, plus the energy deposited by the kaon decay products, as a function of the energy depositions which do not fit any of the other criteria, in the simulated nucleon decay, and cosmic background samples. The events failing the application of the muon length (black circle), fiducial (red box) and vertex (blue triangle) cuts, as well as the events passing all cuts (pink triangle) are shown.



(a) The energy distribution of signal events.



(b) The energy distribution of cosmic background events.

Fig. 7.17 The energy directly deposited by kaons, plus the energy deposited by the kaon decay products, plus the energy directly deposited by electrons, plus the energy deposited near the kaon and electron vertex, as a function of the energy depositions which do not fit any of the other criteria, in the simulated nucleon decay, and cosmic background samples. The events failing the application of the muon length (black circle), fiducial (red box) and vertex (blue triangle) cuts, as well as the events passing all cuts (pink triangle) are shown.

7.3.4 Future improvements to nucleon decay studies

Thus far the nucleon decay studies have been performed on the Monte Carlo truth information, and so have not used reconstructed objects such as tracks. The extension of the analyses to include work on tracks is an important next step as then the full analysis which would be applied on real data can be tested. Preliminary studies have begun on hit reconstruction, and involve running a filter on the muons used in the earlier analyses. This is because the number of events which are saved to disk would be prohibitive to running the full reconstruction process. As such, only events which meet the following criteria will be reconstructed [44];

- A minimum of 10 MeV deposited in the detector volume.
- A maximum of 3,000 MeV deposited in the detector volume.
- A maximum of 5 MeV deposited within 10 cm of the detector edge.

These criteria are designed to be broad enough that the full range of nucleon decay modes can be studied, including di-nucleon decay modes, hence the maximum deposited energy greatly exceeding the rest mass of a single nucleon.

15

References

- [1] E. D. Church, “LArSoft: A Software Package for Liquid Argon Time Projection Drift Chambers,” 2013. 1
2
3
- [2] The LArSoft collabortion. (2017) Software for LArTPCs. [Online]. Available: <http://larsoft.org> 4
5
- [3] R. Brun and F. Rademakers, “ROOT: An object oriented data analysis framework,” *Nucl. Instrum. Meth.*, vol. A389, pp. 81–86, 1997. 6
7
- [4] S. Agostinelli *et al.*, “Geant4—a simulation toolkit,” *Nuclear Instruments and Methods in Physics Research Section A: Accelerators, Spectrometers, Detectors and Associated Equipment*, vol. 506, no. 3, pp. 250 – 303, 2003. [Online]. Available: <http://www.sciencedirect.com/science/article/pii/S0168900203013688> 8
9
10
11
- [5] C. Andreopoulos *et al.*, “The GENIE neutrino Monte Carlo generator,” *Nuclear Instruments and Methods in Physics Research Section A: Accelerators, Spectrometers, Detectors and Associated Equipment*, vol. 614, no. 1, pp. 87 – 104, 2010. [Online]. Available: <http://www.sciencedirect.com/science/article/pii/S0168900209023043> 12
13
14
15
- [6] D. Casper, “The Nuance neutrino physics simulation, and the future,” *Nucl. Phys. Proc. Suppl.*, vol. 112, pp. 161–170, 2002, [,161(2002)]. 16
17
- [7] C. Hagman *et al.* (2012) Cosmic-ray Shower Library CRY. [Online]. Available: http://nuclear.llnl.gov/simulation/doc_cry_v1.7/cry.pdf 18
19
- [8] V. Kudryavtsev, “Muon simulation codes MUSIC and MUSUN for underground physics,” *Computer Physics Communications*, vol. 180, no. 3, pp. 339 – 346, 2009. [Online]. Available: <http://www.sciencedirect.com/science/article/pii/S0010465508003640> 20
21
22
23
- [9] V. A. Kudryavtsev, N. J. C. Spooner, and J. E. McMillan, “Simulations of muon induced neutron flux at large depths underground,” *Nucl. Instrum. Meth.*, vol. A505, pp. 688–698, 2003. 24
25
26
- [10] P. Antonioli, C. Ghetti, E. V. Korolkova, V. A. Kudryavtsev, and G. Sartorelli, “A Three-dimensional code for muon propagation through the rock: Music,” *Astropart. Phys.*, vol. 7, pp. 357–368, 1997. 27
28
29
- [11] V. A. Kudryavtsev, E. V. Korolkova, and N. J. C. Spooner, “Narrow muon bundles from muon pair production in rock,” *Phys. Lett.*, vol. B471, pp. 251–256, 1999. 30
31

- ¹ [12] J. Asaadi *et al.* (2016, Sept) The Current Status of Simulation and Reconstruction for the DUNE Far Detector. [Online]. Available: <http://docs.dunescience.org:8080/cgi-bin>ShowDocument?docid=1689>
- ⁴ [13] C. Harris and M. Stephens, “A combined corner and edge detector.” Citeseer, 1988.
- ⁵ [14] P. V. C. Hough, “Machine Analysis Of Bubble Chamber Pictures,” in *Proceedings, 2nd International Conference on High-Energy Accelerators and Instrumentation, HEACC 1959: CERN, Geneva, Switzerland, September 14-19, 1959*, vol. C590914, 1959, pp. 554–558. [Online]. Available: http://inspirehep.net/record/919922/files/HEACC59_598-602.pdf
- ¹⁰ [15] M. Antonello *et al.*, “Precise 3D track reconstruction algorithm for the ICARUS T600 liquid argon time projection chamber detector,” *Adv. High Energy Phys.*, vol. 2013, p. 260820, 2013.
- ¹³ [16] J. S. Marshall and M. A. Thomson, “The Pandora Software Development Kit for Pattern Recognition,” *Eur. Phys. J.*, vol. C75, no. 9, p. 439, 2015.
- ¹⁵ [17] M. Wallbank. (2016, June) EMShower Reconstruction. [Online]. Available: <http://docs.dunescience.org:8080/cgi-bin>ShowDocument?docid=1369>
- ¹⁷ [18] J. Birks, “The efficiency of organic scintillatois,” *ORGANIC*, p. 12, 1960.
- ¹⁸ [19] R. Acciarri *et al.*, “A study of electron recombination using highly ionizing particles in the ArgoNeuT Liquid Argon TPC,” *JINST*, vol. 8, p. P08005, 2013.
- ²⁰ [20] J. Thomas and D. A. Imel, “Recombination of electron-ion pairs in liquid argon and liquid xenon,” *Phys. Rev. A*, vol. 36, pp. 614–616, Jul 1987. [Online]. Available: <http://link.aps.org/doi/10.1103/PhysRevA.36.614>
- ²³ [21] H. Bethe, “Zur theorie des durchgang schneller korpuskularstrahlen durch materie,” *Annalen der Physik*, vol. 397, no. 3, pp. 325–400, 1930. [Online]. Available: <http://dx.doi.org/10.1002/andp.19303970303>
- ²⁶ [22] F. Bloch, “Zur bremsung rasch bewegter teilchen beim durchgang durch materie,” *Annalen der Physik*, vol. 408, no. 3, pp. 285–320, 1933. [Online]. Available: <http://dx.doi.org/10.1002/andp.19334080303>
- ²⁹ [23] C. Patrignani *et al.*, “Review of Particle Physics,” *Chin. Phys.*, vol. C40, no. 10, p. 100001, 2016.
- ³¹ [24] J. Insler. (2016, March) Module to unstick ADC codes. [Online]. Available: <https://indico.fnal.gov/getFile.py/access?contribId=2&resId=0&materialId=slides&confId=11627>
- ³⁴ [25] MicroBooNE Collaboration. (2016, July) Noise Characterization and Filtering in the MicroBooNE TPC. [Online]. Available: <http://www-microboone.fnal.gov/publications/publicnotes/MICROBOONE-NOTE-1016-PUB.pdf>
- ³⁷ [26] J. Cooley and J. Turkey, “An algorithm for the machine calculation of complex fourier series,” *Math. Comp.*, vol. 19, pp. 297–301, 1965.

- [27] N. Wiener, *Extrapolation, Interpolation, and Smoothing of Stationary Time Series*. [Cambridge]: Technology Press of the Massachusetts Institute of Technology., 1942. 1
2
- [28] M. Johnson *et al.* (2016, August) 35T Observations and Measurements. [Online]. Available: <http://docs.dunescience.org:8080/cgi-bin>ShowDocument?docid=1704> 3
4
- [29] L. Bagby *et al.* (2016, Oct) 35T Noise Studies Summary - APA wire readout noise. [Online]. Available: <http://docs.dunescience.org:8080/cgi-bin>ShowDocument> 5
6
- [30] T. Yang. (2016, June) Update on reconstruction of 35t data. [Online]. Available: <https://indico.fnal.gov/getFile.py/access?contribId=1&resId=0&materialId=slides&confId=12349> 7
8
9
- [31] P. Torr and A. Zisserman, “Mlesac: A new robust estimator with application to estimating image geometry,” *Computer Vision and Image Understanding*, vol. 78, no. 1, pp. 138–156, 2000. 10
11
12
- [32] M. Thiesse. (2016, Aug) Hit reconstruction and purity. [Online]. Available: <https://indico.fnal.gov/getFile.py/access?contribId=1&resId=0&materialId=slides&confId=12859> 13
14
15
- [33] C. Anderson *et al.*, “The ArgoNeuT Detector in the NuMI Low-Energy beam line at Fermilab,” *JINST*, vol. 7, p. P10019, 2012. 16
17
- [34] T. Yang. (2016, June) Update on 35 ton analysis. [Online]. Available: <https://indico.fnal.gov/getFile.py/access?contribId=1&resId=0&materialId=slides&confId=12396> 18
19
- [35] V. M. Atrazhev and I. V. Timoshkin, “Trasport of electrons in atomic liquids in high electric fields,” *IEEE Trans. Dielectrics and Electrical Insulation*, vol. 5, pp. 450–457, 1998. 20
21
22
- [36] Y. Li *et al.*, “Measurement of Longitudinal Electron Diffusion in Liquid Argon,” *Nucl. Instrum. Meth.*, vol. A816, pp. 160–170, 2016. 23
24
- [37] D. Brailsford. (2016, Sept) Looking at electron diffusion in 35t data and MC. [Online]. Available: <https://indico.fnal.gov/getFile.py/access?contribId=43&sessionId=19&resId=0&materialId=slides&confId=10613> 25
26
27
- [38] C. Bromberg *et al.*, “Design and operation of longbo: a 2 m long drift liquid argon tpc,” *Journal of Instrumentation*, vol. 10, no. 07, p. P07015, 2015. 28
29
- [39] D. M. Mei, C. Zhang, K. Thomas, and F. Gray, “Early Results on Radioactive Background Characterization for Sanford Laboratory and DUSEL Experiments,” *Astropart. Phys.*, vol. 34, pp. 33–39, 2010. 30
31
32
- [40] M. L. Cherry, M. Deakyne, K. Lande, C. K. Lee, R. I. Steinberg, B. Cleveland, and E. J. Fenyves, “Multiple muons in the homestake underground detector,” *Phys. Rev. D*, vol. 27, pp. 1444–1447, Apr 1983. [Online]. Available: <http://link.aps.org/doi/10.1103/PhysRevD.27.1444> 33
34
35
36
- [41] E. Church. (2016, Sept) September 2016 Progress Report from the Atmospheric Neutrinos, Nucleon Decay, and Cosmogenics Working Groups. [Online]. Available: <http://docs.dunescience.org:8080/cgi-bin>ShowDocument?docid=1644> 37
38
39

References

132

- ¹ [42] V. A. Kudryavtsev *et al.* (2014) Muon simulations for LBNE using MUSIC and
² MUSUN. [Online]. Available: <http://lbne2-docdb.fnal.gov/cgi-bin>ShowDocument?docid=9673>
- ⁴ [43] A. Bueno, Z. Dai, Y. Ge, M. Laffranchi, A. J. Melgarejo, A. Meregaglia, S. Navas, and
⁵ A. Rubbia, “Nucleon decay searches with large liquid argon TPC detectors at shallow
⁶ depths: Atmospheric neutrinos and cosmogenic backgrounds,” *JHEP*, vol. 04, p. 041,
⁷ 2007.
- ⁸ [44] M. Robinson. (2017, Jan) Cosmogenic background to nucleon decay. [Online].
⁹ Available: <https://indico.fnal.gov/getFile.py/access?contribId=104&sessionId=14&resId=0&materialId=slides&confId=10641>
¹⁰

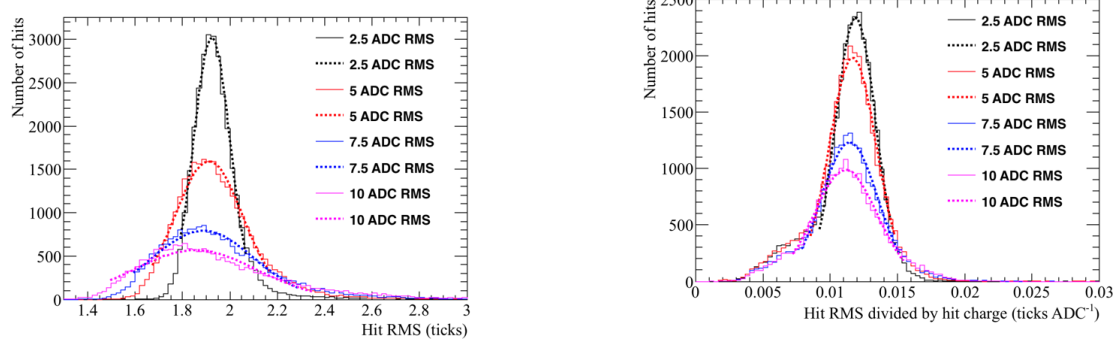
Appendix A

Supporting figures to Monte Carlo studies concerning determining interaction times using the effects of diffusion

Figure A.1, shows how the most probable values of the hit RMS and hit $RMS/Charge$ change as the electronics noise increases, for hits between 20 and 30 cm from the APAs. Figure A.2, shows how the most probable values of hit RMS changes as drift distance increases for track associated with counter differences of 4, for different values of the electronics noise. Figure A.3, shows how the most probable value of hit RMS next to the APAs changes for increasing counter difference. Figure A.16, shows the normalised hit charge distributions for increasing noise levels, and the cut which is applied to remove the tails of the distribution.

Figure A.5, shows how the most probable values of the hit RMS and hit $RMS/Charge$ change as the electron lifetime increases, for hits between 20 and 30 cm from the APAs. Figure A.6, shows how the most probable values of hit RMS changes as drift distance increases for track associated with counter differences of 4, for different values of the electron lifetime. Figure A.7, shows how the most probable value of hit RMS next to the APAs changes for increasing counter difference.

Figure A.9, shows how the most probable values of the hit RMS and hit $RMS/Charge$ change as the electric field increases, for hits between 20 and 30 cm from the APAs. Figure A.10, shows how the most probable values of hit RMS changes as drift distance increases



(a) The most probable hit *RMS* values for hits between $x = 20$ cm and $x = 30$ cm.

(b) The most probably hit *RMS/Charge* values for hits between $x = 20$ cm and $x = 30$ cm.

Fig. A.1 The most probable values of the hit *RMS* and hit *RMS/Charge* distributions for hits between $x = 20$ cm and $x = 30$ cm, for tracks with a counter difference of 4, as the electronics noise changes.

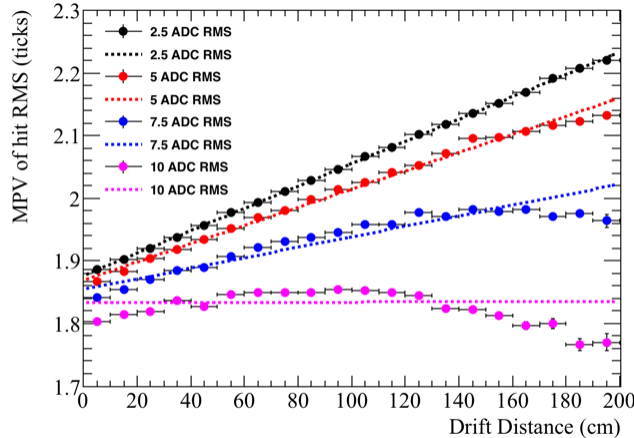


Fig. A.2 The most probable values of hit *RMS* as a function of drift distance, for tracks associated with a coincidence that had a counter difference of 4, as the electronics noise changes.

¹ for track associated with counter differences of 4, for different values of the electric field.
² Figure A.11, shows how the most probable value of hit *RMS* next to the APAs changes for
³ increasing counter difference.

⁴
⁵ Figure A.13, shows how the most probable values of the hit *RMS* and hit *RMS/Charge*
⁶ change as the constant of longitudinal diffusion increases, for hits between 20 and 30 cm
⁷ from the APAs. Figure A.14, shows how the most probable values of hit *RMS* changes as
⁸ drift distance increases for track associated with counter differences of 4, for different values

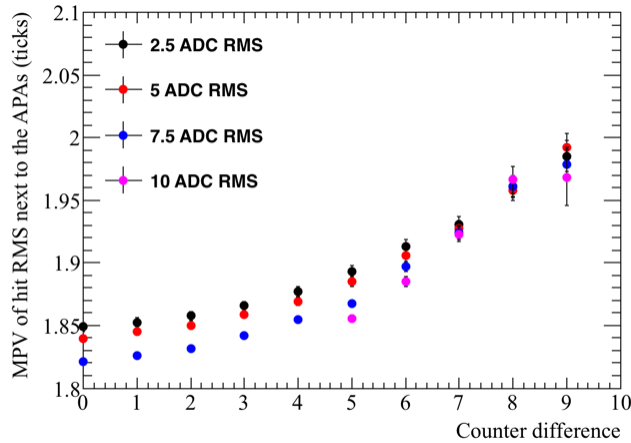


Fig. A.3 The most probable values of hit *RMS* within 10 cm of the APAs, as a function of the counter difference of the coincidence, that the track was associated with, as the electronics noise changes.

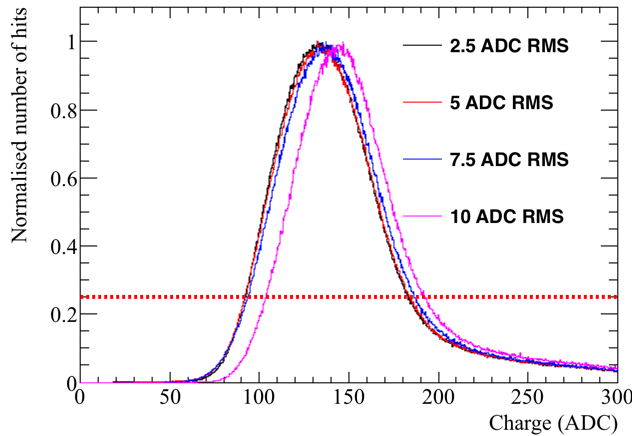
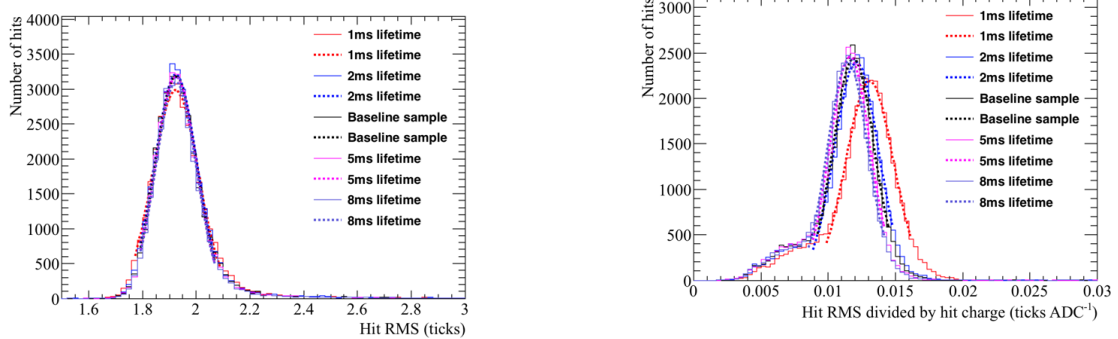


Fig. A.4 The normalised hit charge distribution as the electronics noise changes. The hit charge is shown in units of ADC, and is normalised so that the most common hit charge has a value of 1. A cut on the normalised number of hits being greater than 0.25 is shown, the aim of this cut is to remove the tails of the hit charge distribution.

of the constant of longitudinal diffusion. Figure A.15, shows how the most probable value of hit *RMS* next to the APAs changes for increasing counter difference.

1
2
3



(a) The most probable hit *RMS* values for hits between $x = 20$ cm and $x = 30$ cm.

(b) The most probably hit *RMS/Charge* values for hits between $x = 20$ cm and $x = 30$ cm.

Fig. A.5 The most probable values of the hit *RMS* and hit *RMS/Charge* distributions for hits between $x = 20$ cm and $x = 30$ cm, for tracks with a counter difference of 4, as the electron lifetime changes.

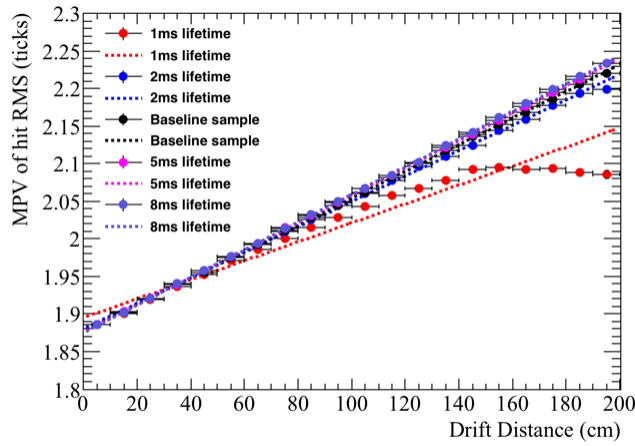


Fig. A.6 The most probable values of hit *RMS* as a function of drift distance, for tracks associated with a coincidence that had a counter difference of 4, as the electron lifetime changes.

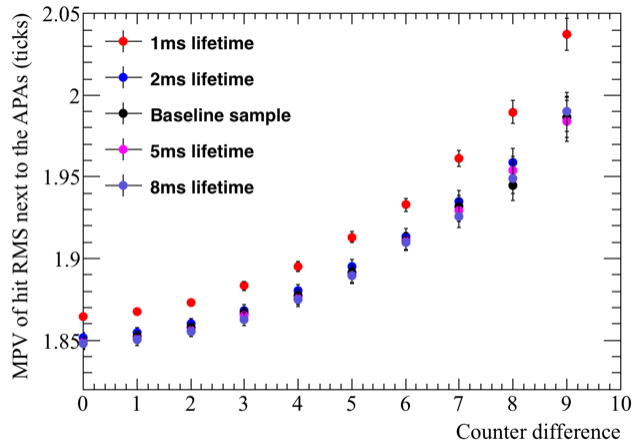


Fig. A.7 The most probable values of hit *RMS* within 10 cm of the APAs, as a function of the counter difference of the coincidence, that the track was associated with, as the electron lifetime changes.

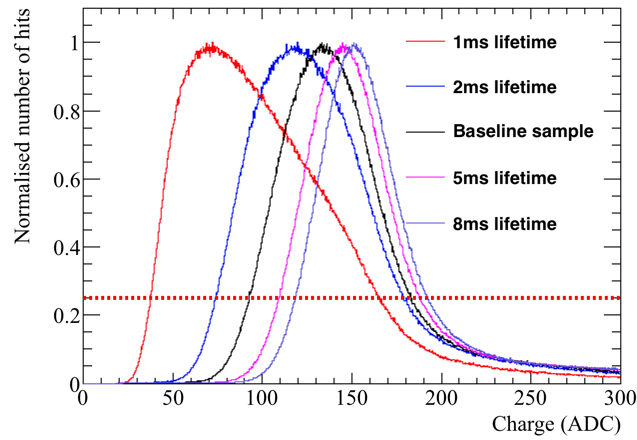
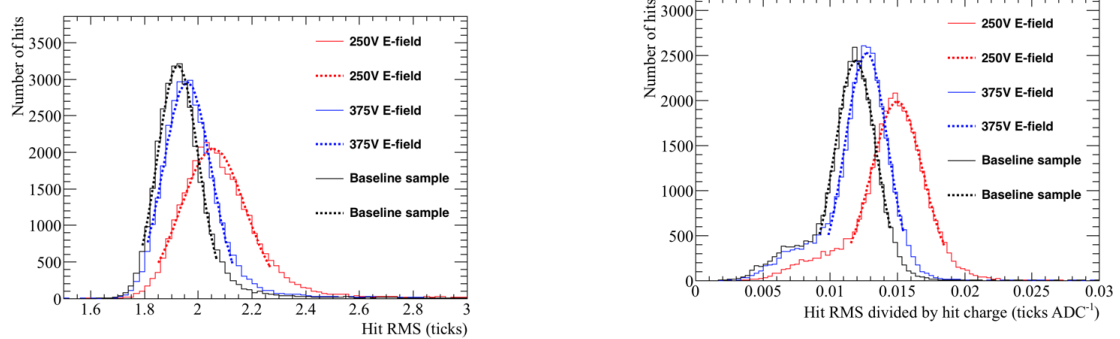


Fig. A.8 The normalised hit charge distribution as the electron lifetime changes. The hit charge is shown in units of ADC, and is normalised so that the most common hit charge has a value of 1. A cut on the normalised number of hits being greater than 0.25 is shown, the aim of this cut is to remove the tails of the hit charge distribution.



(a) The most probable hit *RMS* values for hits between $x = 20$ cm and $x = 30$ cm.

(b) The most probably hit *RMS/Charge* values for hits between $x = 20$ cm and $x = 30$ cm.

Fig. A.9 The most probable values of the hit *RMS* and hit *RMS/Charge* distributions for hits between $x = 20$ cm and $x = 30$ cm, for tracks with a counter difference of 4, as the electric field changes.

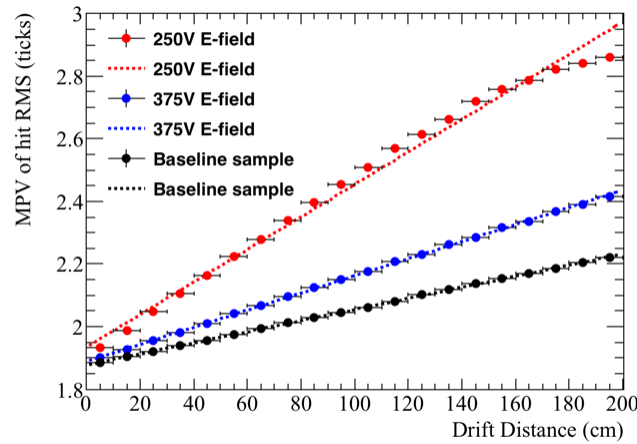


Fig. A.10 The most probable values of hit *RMS* as a function of drift distance, for tracks associated with a coincidence that had a counter difference of 4, as the electric field changes.

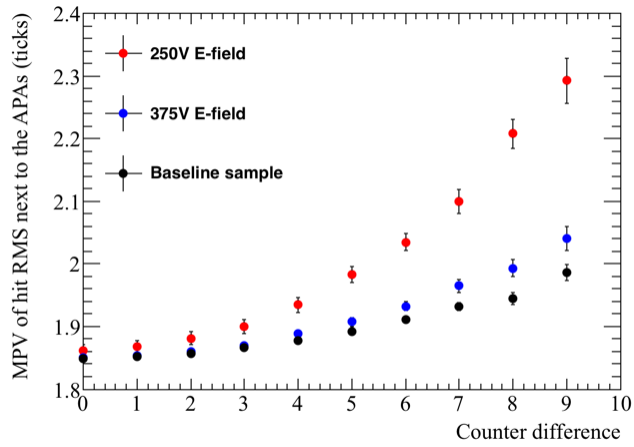


Fig. A.11 The most probable values of hit *RMS* within 10 cm of the APAs, as a function of the counter difference of the coincidence, that the track was associated with, as the electric field changes.

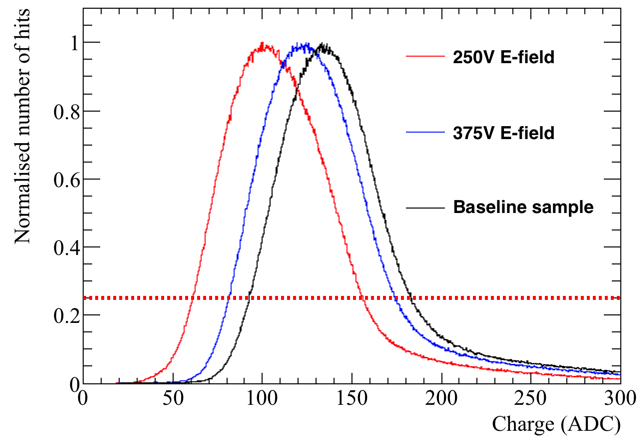
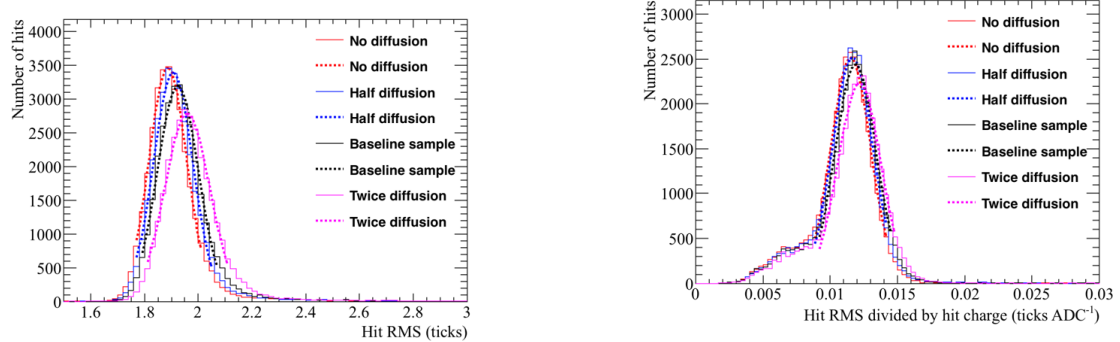


Fig. A.12 The normalised hit charge distribution as the electric field changes. The hit charge is shown in units of ADC, and is normalised so that the most common hit charge has a value of 1. A cut on the normalised number of hits being greater than 0.25 is shown, the aim of this cut is to remove the tails of the hit charge distribution.



(a) The most probable hit *RMS* values for hits between $x = 20$ cm and $x = 30$ cm.

(b) The most probable hit *RMS/Charge* values for hits between $x = 20$ cm and $x = 30$ cm.

Fig. A.13 The most probable values of the hit *RMS* and hit *RMS/Charge* distributions for hits between $x = 20$ cm and $x = 30$ cm, for tracks with a counter difference of 4, as the constant of longitudinal diffusion changes.

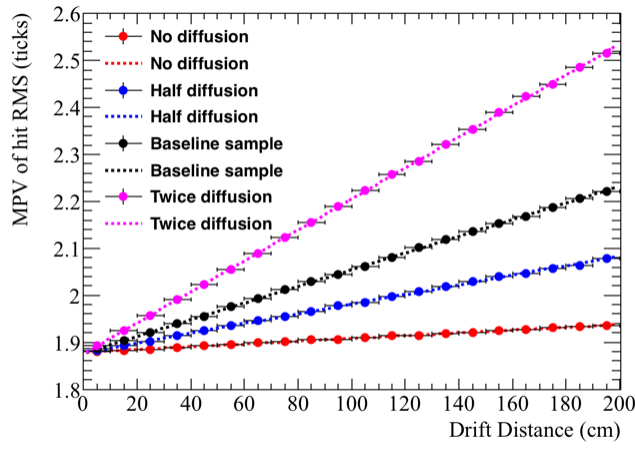


Fig. A.14 The most probable values of hit *RMS* as a function of drift distance, for tracks associated with a coincidence that had a counter difference of 4, as the constant of longitudinal diffusion changes.

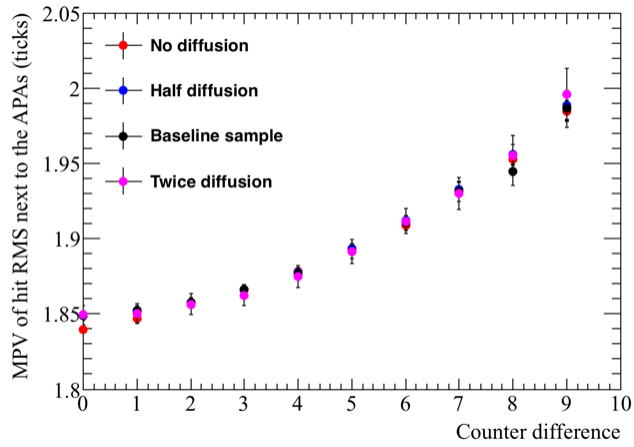


Fig. A.15 The most probable values of hit *RMS* within 10 cm of the APAs, as a function of the counter difference of the coincidence, that the track was associated with, as the constant of longitudinal diffusion changes.

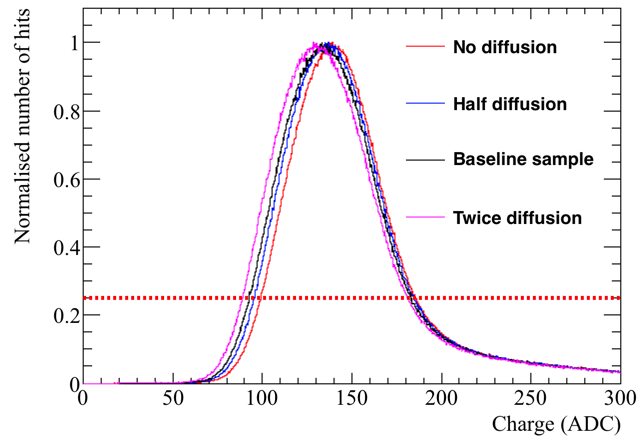


Fig. A.16 The normalised hit charge distribution as the constant of longitudinal diffusion changes. The hit charge is shown in units of ADC, and is normalised so that the most common hit charge has a value of 1. A cut on the normalised number of hits being greater than 0.25 is shown, the aim of this cut is to remove the tails of the hit charge distribution.

¹ **Appendix B**

² **Something else mildly interesting**